



Steels for rails

W. Solano-Alvarez^{a,*}, H.K.D.H. Bhadeshia^{a,b}

^a Materials Science and Metallurgy, University of Cambridge, UK

^b School of Engineering and Materials Science, Queen Mary University of London, UK

ARTICLE INFO

Keywords:

Steel
rails
Wear
White-etching layer
Rolling contact fatigue
Pearlite
Bainite
Alloy design
Weldability
Inclusions
Contact mechanics

ABSTRACT

Transport by rail is an efficient way of moving goods and people while managing problems such as congestion and the consequences on the environment. The relatively low energy consumption and CO₂ emissions are attributed to the low rolling-resistance due to the stiffness of the wheel and rail, leading to small contact area [1]. Investments in rail transportation has boomed in recent years. London, with the oldest underground rail system in the world, has added the Elisabeth Line at a cost of some £14 billion; China now has the largest high-speed rail system in the world. All these developments rely on the safe performance of steel rails, which suffer from two primary damage mechanisms, rolling-contact fatigue caused essentially by repeated contact stresses with the wheel, and a variety of wear mechanisms. Factors such as weldability are important, given that all modern rails are continuous. This review deals with the detailed physical-metallurgy of rail steels, including alloy design, microstructure, variety and choice, and damage mechanisms.

1. Introduction

Steel rails enable the movement of goods and people on well-defined pathways that ensure right-of-way. The rolling stock relies entirely on steel wheels so its motion involves metal-to-metal contact that must be optimised to ensure safety and service life. Amongst many variables, the nature of that contact depends on whether the rolling stock is configured for passenger traffic or to carry heavy goods. Conditions often require that the rail path is not straight, in which case the loading on the rail section will not be uniform, causing uneven wear and damage. There is, therefore, a considerable combination of engineering and metallurgy involved in the design of rails.

The metallurgical variables involved in the design of rail steels are really quite complex and difficult to characterise or estimate theoretically [2–4]. They include localised plasticity [5], wear [6], rolling contact fatigue [7], corrosion [8] and impact fracture during service [9]. These mechanisms require a basket of properties to be optimised simultaneously, with the focus on strength, work-hardening behaviour, toughness, hardness, subsurface initiated fatigue, crack growth rates, wear resistance and weldability [10–12]. And these parameters do not work in isolation – for example, a high wear-resistance means that surface-initiated fatigue cracks are not “tribologically machined” away during service.

1.1. Snippet of history

Wooden railways appeared first in Great Britain, in locations where the goods would be conveyed to one place only, such as at coal

* Corresponding author.

E-mail address: wilberths@hotmail.com (W. Solano-Alvarez).

Nomenclature

α, β	Terms involving the Poisson's ratio in contact mechanics
α	Ferrite
α'	Martensite
α_b	Bainite
γ	Shear strain
γ_0	Initial shear strain increment
γ_s	% difference in surface speeds of wheel and rail
γ	Austenite
δ	Tensile ductility
ϵ_a	Strain amplitude in cyclic loading
$\Delta\epsilon$	Difference between maximum and minimum strain components
θ	Cementite
μ_f	Coefficient of friction, dimensionless
ν	Poisson's ratio
ξ	Creepage, the difference between surface velocities of items rolling against each other, divided by the mean velocity
σ	Stress - subscript 'f' for cleavage fracture stress, 'i' for friction stress, 'y' for yield stress, 'u' for ultimate tensile stress, '0.2' for proof stress
τ	Principal shear stress in contact zone
A	Contact area
A_{C_3}	Temperature at which austenite formation begins during heating
d_s	Sliding distance
F	Normal force in Newtons
$F_t\gamma/A$	Tractive force
H	Hardness in Nm^{-2}
k	Archard wear coefficient
k_e	Stress corresponding to radius of Tresca yield-locus circle
k_{HP}	Hall-Petch coefficient
K_{Ic}	Plane strain fracture toughness
\bar{L}	Mean lineal intercept defining grain size
N	Number of rolling-contact cycles
p_0	Hertzian contact pressure
p_0^s	Hertzian pressure at shakedown
P	Contact load per unit length
P	Load corresponding to ratcheting limit
q	Tangential traction
q'	Heat flow
S_I	Pearlite interlamellar spacing
S^{WT}	Smith-Watson-Topper damage parameter
T_E	Eutectoid temperature
$T_E - T$	Undercooling at which pearlite forms
v_r	Relative velocity of rubbing surfaces
V_w	Wear volume
V_V^0	Volume fraction of phase θ
ppmw	Parts per million by weight
CCT	Continuous cooling transformation
RCF	Rolling Contact Fatigue
SEM	Scanning electron microscope (microscopy)
WEL	White-etching layer
WEM	White-etching matter

mines [13]. The wood, though of great strength, “would soon become reduced in depth ... and break long before it was worn through”. The wood was then overlaid with cast iron; fully cast-iron rails were subsequently implemented in 1738 but tended to be short in length, uneven and brittle. This was followed by wrought iron rails which were installed at the Walbottle Colliery (Newcastle-upon-Tyne) in 1805; although ductile, they suffered from low hardness, had a large slag content [14] and tended to wear quickly, so slivers of the steel could be found in the vicinity of the track. Indeed, a report by Robert Stephenson and Joseph Locke in July 1857 is said to have stated that [15]:

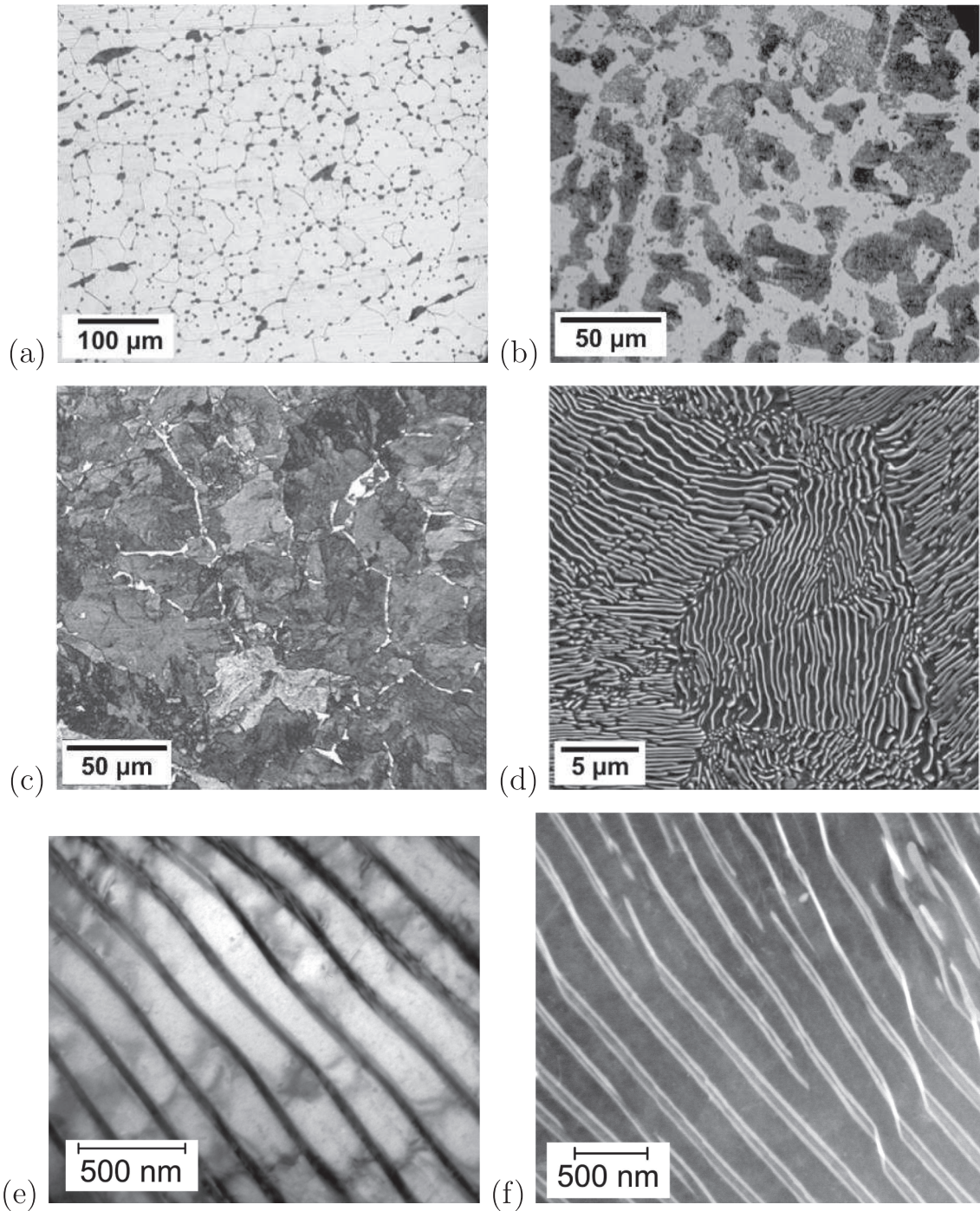


Fig. 1. Structure and carbon concentration of rails over the years. (a) An 1820 wrought iron rail with 0.05C wt%. (b) Mushet's 1857 pearlitic rail with 0.25C wt%. (c) A 1950 pearlitic steel with ≈ 0.55 C wt%. (d) A 1970 pearlitic rail with 0.75 wt% C. Adapted and reproduced with the permission of Dr. J. Jaiswal [18]. (e) Experimental hypereutectoid rail-steel containing 0.92C-0.96Mn-0.32Cr, with a true interlamellar spacing of 203 ± 32 nm [19]. (f) Hypoeutectoid Fe-0.57C-1Mn-0.08-0.2 V wt% rail with an interlamellar spacing of about 200 nm with thin cementite sheets separated by ferrite [20].

“... all attempts have failed to provide a good durable rail – and the consequence is that *destruction* and not fair *wear and tear* results”.

Within two months of this report, Henry Bessemer announced the mass manufacture of *steel*; by 1905 about 11 million tonnes of Bessemer steel was made into rails [16]. The original implementation of a steel rail was by Robert Forester Mushet, installed at the Derby Midlands station in the UK, early 1857 [17]; the rail was a low carbon manganese pearlitic alloy, a disruptive technology that in time completely replaced the cast iron or wrought iron rails. The manufacturing process steadily improved with continuous casting introduced during the 1970s alongside an enhancement in the cleanliness of the steel produced. Rails could be made in longer lengths, minimising the number of joints required.

Fig. 1 illustrates the evolution of the rail microstructure over a period of two centuries. The original metal rail was wrought iron which is ductile but too soft to sustain reliable service over prolonged periods. This was replaced by a higher carbon steel that had a mixture of allotriomorphic ferrite and pearlite, with the carbon concentration increased subsequently to generate fully pearlitic microstructures. Subsequent developments in the modern era focused on the refinement of the interlamellar spacing of the pearlite in order to enhance the strength without excessive alloying which can jeopardise weldability.

1.2. Towards the modern rail

The essential objective over the last 150 years has been the optimisation of manufacturing process and service life, given the ever more arduous conditions the rails are required to endure [21]. This entails the following:

- production of cleaner steels to mitigate damage originating at inclusions such as MnS, Al₂O₃ and SiO₂, some of which become shaped during the hot-rolling of rails [22] or in localised regions even during service [23]. In some scenarios, Al₂O₃–SiO₂–MnO inclusions stimulate the nucleation rate of MnS by providing heterogeneous nucleation sites, thus refining its particle size, which must benefit performance [24].
- It has long been known that phosphorus in a rail steel does not add desirable qualities [25], causing breakage when the concentration is above 0.12 wt% – this concentration is far too high to be tolerated in modern rails given the tendency for prior austenite grain boundary embrittlement. Although this kind of embrittlement may not be common in modern pearlitic rails where the prior boundaries are eliminated as pearlite grows across them, it is a critical feature of rails based on displacive transformations such as bainite [3,26]. Dissolved and diffusible hydrogen is well-established to embrittle all steels [27,28]. It can be present within the rolled rail and evolve during cooling (leading to flaking) [29] and it may enter rail steels through the cathodic reactions associated with corrosion [30]. The role of sulphur in forming MnS has already been mentioned.
- Greater yield strength to avoid gross plastic deformation at the head of the rail, and to reduce the wear rate. There is a large reduction in wear rate when the hardness is increased beyond ≈ 260 HV, with the improvement becoming less sensitive to strength beyond that [31].
- Increase in the rail head cross section to reduce the load, and increased hardness achieved by refining the interlamellar spacing of pearlite using a combination of solute additions and heat treatments [29,18].

All of these aspects are related to rail failures of the type illustrated in Fig. 2, albeit in old rails and details connected to modern rails are described later in the text.

The introduction of the basic oxygen furnace, secondary steelmaking, and continuous casting all help limit inclusions and undesired elements. The topic is still a focus of research in the manufacture of rail steels [e.g., 32–34]. A new understanding is related to the role of slag basicity defined often by the ratio $([\text{CaO} + \text{MgO}]/[\text{SiO}_2 + \text{Al}_2\text{O}_3])$ wt%; the silica is classified as an acidic oxide because it accepts oxygen atoms from the basic oxides. An increase in the basicity ratio changed inclusion compositions from SiO₂–CaO to Al₂O₃–MgO–SiO₂–CaO with a greater alumina content, so they remained only partly liquid during the hot-rolling of rails, and hence were in a more beneficial state in the final rail [34]. The CaO–Al₂O₃ phase diagram has a deep eutectic at 49 wt% of CaO [35], with a slag of that basicity ensuring finer inclusions [36].

Cleanliness using better steelmaking processes has a cost so choices have to be made by balancing the factors controlling service life against the through life costs. It would not, for example, be practical from the point of view of cost, to reduce the phosphorus concentration of rail steel to less than 0.005 wt%, although the technology exists for doing so in other contexts (Table 1).

There nevertheless is a continuing demand on steel quality given the requirements for greater traffic densities, mixed traffic, higher speeds and greater axle-loads from freight trains in response to greater demand [40,41]. Weldability can also be compromised by the cleanliness of the base rail-steel [42]; the rolling contact fatigue limit of a repair-welded rail depends on the steel cleanliness [43]. The welding itself may introduce oxide inclusions in the region that melts and solidifies.

An axle-load is defined by the weight on two wheels joined by an axle, or equivalently, the total permitted weight of a loaded wagon divided by its number of axles. The maximum permitted axle-load in Europe is 22.5 tonnes [44] though it is greater in the USA and on the so-called heavy-haul railroads, where it can be in excess of 40 tonnes [45]. These factors can induce different failure mechanisms such as the loss of rail profile, corrugation, plastic deformation, fatigue and rolling contact fatigue, and catastrophic fracture induced by corrosion or weld repairs, Fig. 3, mechanisms that can jeopardise safety if the damage is not detected and ameliorated following inspections [18,46,47]. In a modern rail-steel containing a typical 0.013 wt% of sulphur, it is possible to find MnS particles that are flattened by the rolling, some 60 μm long; these particles may have oxide at their cores [48].

The complexity of modern wheel-rail contacts is defined by a large number of variables, from rail, pads, clips, sleepers, ballast,

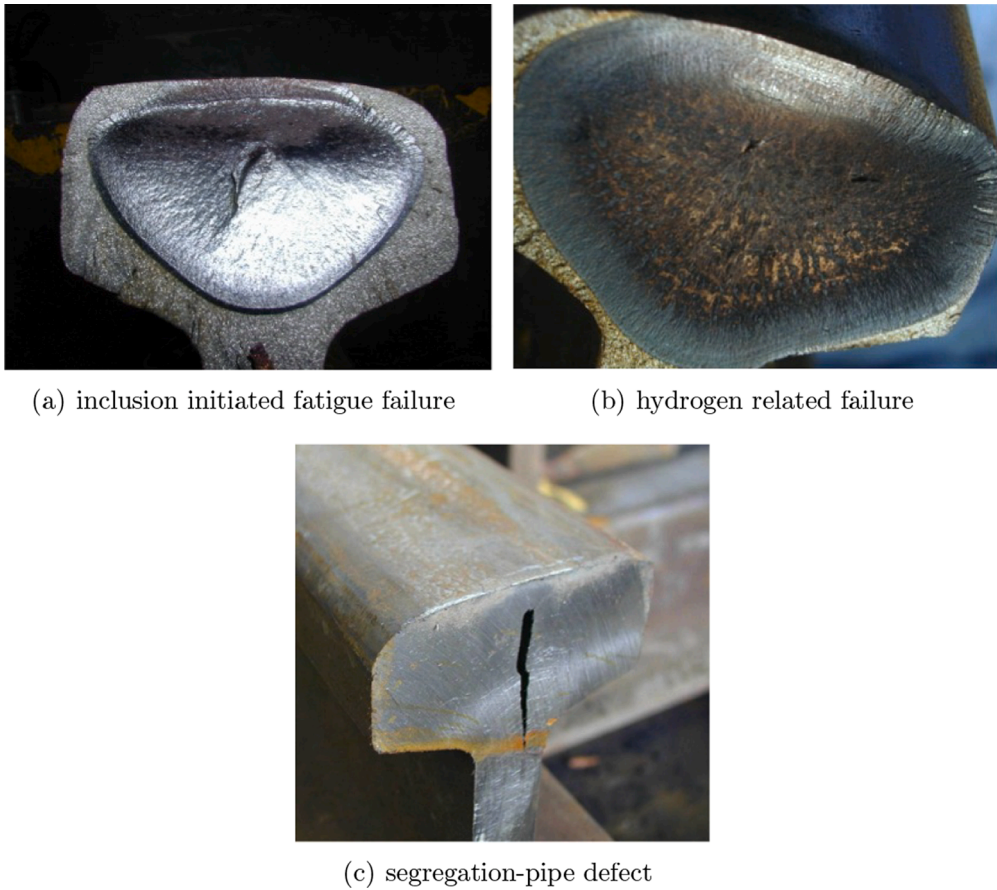


Fig. 2. Examples of rail failures in old rails. Reproduced with the permission of Dr. J. Jaiswal [18].

Table 1

Approximate dissolved impurity levels achievable in commercial steels. From a compilation [37] based on data from [38,39].

Solute	P	C	S	N	H	O	Ti
Concentration/ ppmw	10	5	5	10	< 1	3	10

wheel, suspension, environment, vehicle dynamics and contact mechanics. This makes it difficult to relate microstructure and rail-performance. Reduction of gross damage has, therefore, been focused on reducing contact stresses [49], grinding the rail to remove small surface cracks, improving rail steel, and conducting regular non-destructive inspections [50]. Fatigue initiation and propagation, can be sensitive to the microstructure, as evident in steels for bearings [37]; although both bearings and rails involve rolling contact, there is a huge difference because the former operate while carefully lubricated, whereas the latter may include sliding friction.

Rolling contact fatigue, general wear (a loss $\geq 20\%$ unacceptable), and loss of rail profile are responsible for the replacement of rails that have yet to reach the design life. Early efforts to enhance rail performance focused on increasing the carbon concentration and refining the interlamellar spacing within pearlite in order to make the rail harder. In spite of very early work that indicated a deterioration in the wear performance of rails [51], it is now thoroughly established that making the rail harder mitigates general wear. In rolling-sliding tests on pearlitic rail-steels, the volume of material lost per distance slid correlates nicely with hardness (HV) for a given maximum contact pressure P and creepage ξ^1 [52]:

$$\text{wear rate} / \text{mm}^3 \text{m}^{-1} = -0.008\text{HV} + 3.73 \tag{1a}$$

$$\begin{aligned} &\text{for HV } 280 \rightarrow 400 \quad P = 1300 \text{ MPa} \quad \xi = 0.03 \\ \text{wear rate} / \text{mm}^3 \text{m}^{-1} &= -0.0033\text{HV} + 1.38 \end{aligned} \tag{1b}$$

¹ The creepage is the difference between the two surface velocities of the items rolling against each other, divided by the mean velocity.

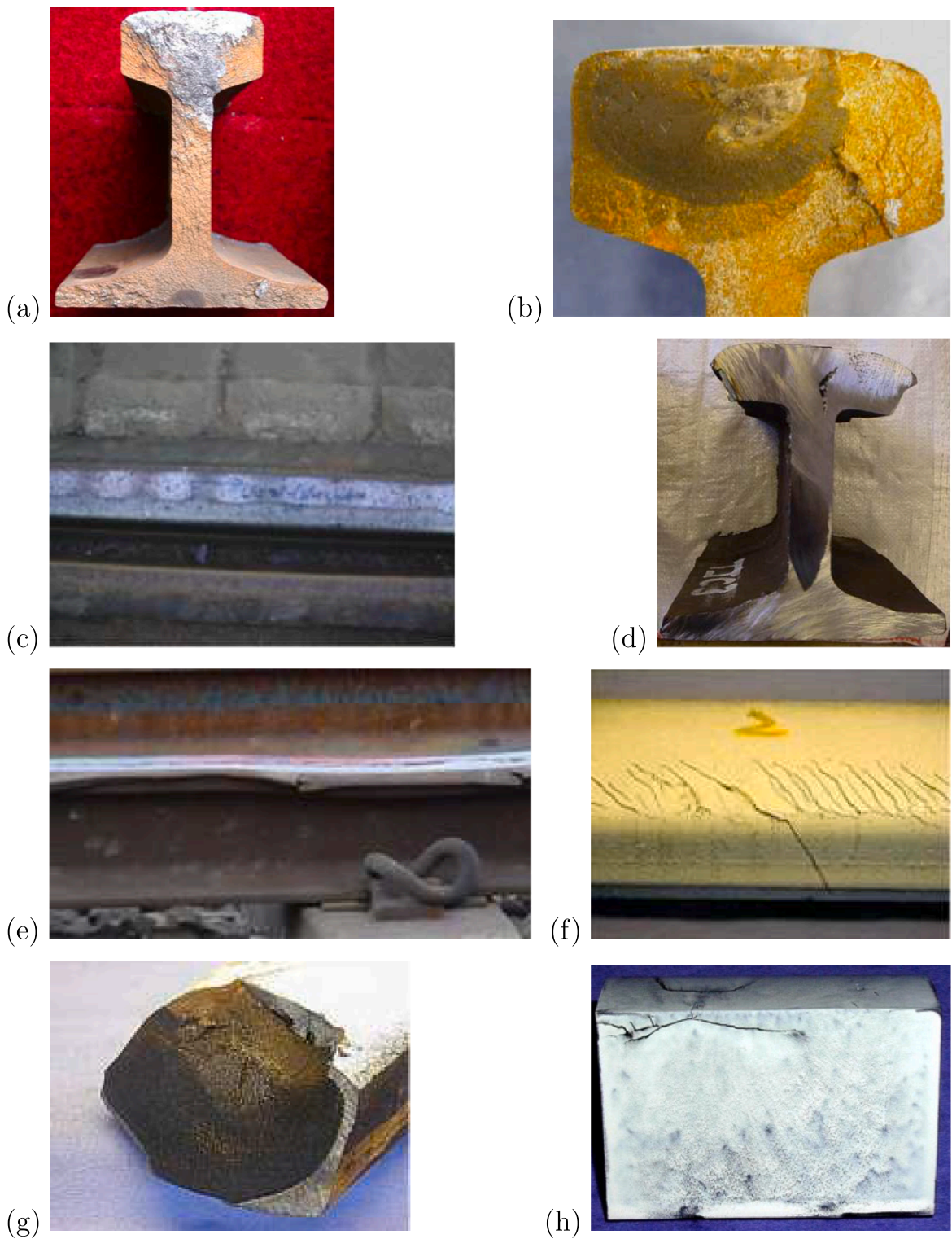


Fig. 3. Failures in contemporary rails: (a) break caused by corrosion at base of foot; (b) fatigue initiated crack at weld repair; (c) corrugation; (d,e) gross plastic deformation; (f,g) rolling-contact fatigue cracks, and (h) squat defect. Reproduced with the permission of Dr. J. Jaiswal [18].

for HV 280→400 $P = 500\text{ MPa}$ $\xi = 0.1$

In unique work, Ueda and Matsuda [53] discovered that the effect of carbon is not simply via the change in hardness. In wear tests done without creepage because the profiled rail disc was driven by pearlitic-wheel disk with an angle of attack of 0.5° and initial contact pressure 2000 MPa, the carbon concentration of the pearlitic rail had an independent effect on reducing both the wear rate and the spalling rate due to rolling contact fatigue, at the same hardness, Fig. 4. It was established that a greater carbon concentration increases the hardness beneath the rolling contact surface, thus suppressing the development of plastic flow needed for damage evolution.

An increase in the hardness of pearlite does decrease wear and enhances rolling contact fatigue resistance [54], but one consequence might be a reduction in toughness and an increase in the fatigue crack growth rate. However, data do not support a systematic dependence of toughness on the yield strength of rails over the range illustrated in Fig. 5. This is likely a reflection of other factors, such as inclusion type and distribution [55], that may influence toughness and at the same time, explain scatter in measured values. In fact, the toughness varies with the location of the sample in the rail cross-section [56,57]. After all, the deformation of the original rectangular bloom used to roll the shape of the rail is not uniform, which affects strength and the shape and size of inclusions.

Some specifications include a minimum value of K_{1C} which presumably is because it allows an estimation of how long it takes for a crack growing by fatigue to reach a critical size:

Minimum yield strength/MPa	Minimum toughness K_{1C} / MPam ^{1/2}
460	26
560	24
460 but head – hardened	30

Hardness of course, is important and its consequences will be discussed in detail in the sections that follow. But it is worth summarising the elementary mechanical properties first and their role in the selection of rail steel.

The stress–strain behaviour in tension of rail steels is similar to other air-cooled pearlitic steels, exhibiting continuous yielding [63]. The head of the rail intentionally can be much stronger if the interlamellar spacing there has been refined by accelerated cooling, Fig. 6, where key properties are summarised. The yield strength and hardness correlate strongly and are both linear functions of $S_f^{-1/2}$, with either parameter controlled to design appropriate steels; the ultimate strength does not feature in the analysis of critical properties such as fatigue and wear.

It is difficult to be explicit about the tensile elongation required to successfully implement rail steels, and oddly, a greater elongation is specified for less-strong rails; lower values of 9→10% are accepted for harder rails, presumably because larger ductility simply cannot be achieved, Fig. 6c. The surface of a rail undergoes plastic shear during service, leading to an accumulation of strain. Cracks initiate when the ductility there becomes exhausted so there must be a tolerable extent of ductility, whether that should be measured in tension or in compression experiments [64].

Cracks in rails usually are initiated at the surface due to fatigue; it is important that these cracks do not reach a critical size for rapid propagation as defined by the fracture toughness, Fig. 5. There is a routine maintenance procedure whereby the surface of the rail is ground down to remove any fatigue damage while maintaining the head profile.

There is a suggestion that it may be possible to achieve the same performance goals by implementing a bainitic microstructure or tempered martensite for better resistance to gross plastic deformation and rolling contact fatigue at lower hardness values than the conventional or head-hardened varieties [18]. The overriding aim of this review is therefore to assess the role that each microstructural parameter plays in the main degradation mechanisms of modern rails so a better understanding of wheel-rail interaction can lead to improved design criteria for rail steels with enhanced properties.

2. Rail metallurgy

2.1. Rail manufacture

Pearlitic rail steels are manufactured by continuous casting at about 0.7 m s^{-1} into rectangular blooms $\approx 410 \times 320\text{ mm}$, which after cooling are reheated to $1200\text{--}1300^\circ\text{C}$ in a gas furnace containing a balanced atmosphere that helps avoid decarburisation [75,76]. This is followed by descaling and hot-deformation in the austenitic condition, using rolls that are shaped so that the cross-section of the rail evolves during multiple passes through roll-gaps to the final shape, as illustrated in Fig. 7.

After rolling, the rails are laid on their sides on a bed where they cool. Given the asymmetric cross-section and consequent non-uniform cooling, the long rails become curved, Fig. 8a,b.

So once they have cooled to less than 100°C , they are straightened first by passing through a series of driven rollers that are located in an alternating sequence above and below the rail. The final hot-rolling pass delivers the required rail-profile; the top rolls of the straightening machine are profiled to the required crown shape and the loads imparted are sufficient to make marginal, final modifications to the shape of the crown. This straightening process subjects the rail to alternating bending of different magnitudes during the passage across the rollers, with the resulting plastic deformation reducing the distortion, i.e., straightening the rail, but leaving it in a state that contains residual stresses, illustrated in Fig. 8. The details of the stress distribution and the signs and magnitudes of the stresses are a function of the straightening machine [77].

While there has been much work on the modelling and measurement of residual stress distributions, it is not obvious that these stresses have a detrimental or beneficial effect on the rolling-contact fatigue performance of the rail. A combination of residual stress

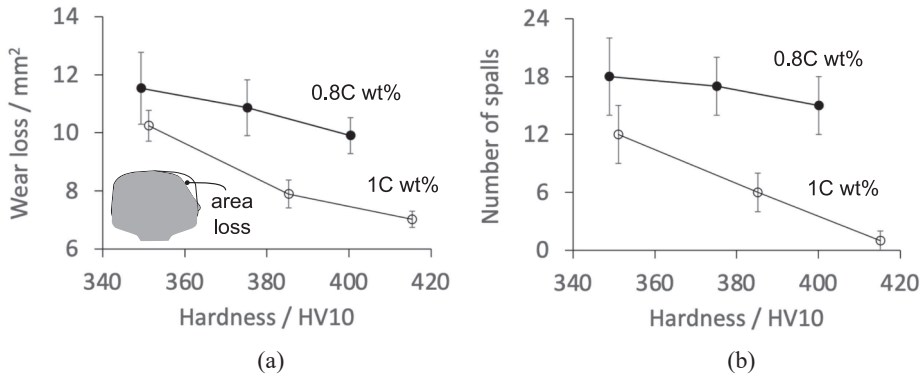


Fig. 4. Test data due to Ueda and Matsuda [53] showing the effect of both carbon and hardness on (a) area loss on the cross-section of the rail; (b) the number of spalls due to rolling contact fatigue when each test was completed.

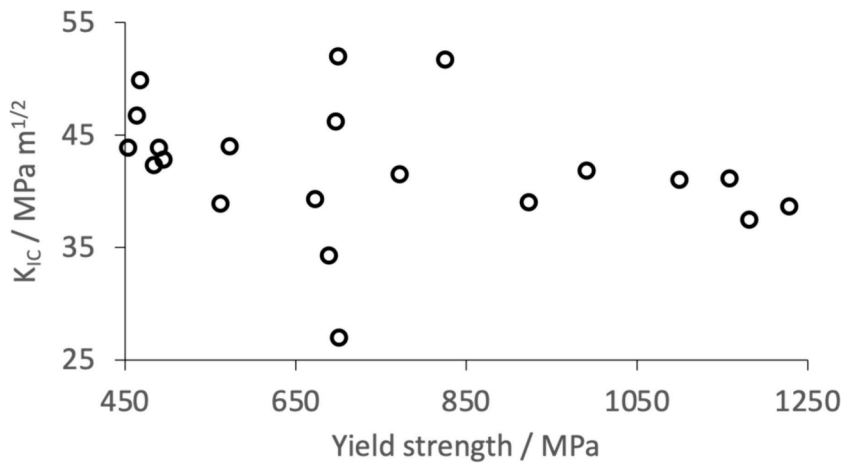


Fig. 5. The fracture toughness of rail heads as a function of the yield strength. Compilation of data from [58–62,55].

and fatigue calculations have been carried out on heavy-haul (30 tonne axle-load) rails that are stress-free and in a second case using a residual-stress field measured from a newly manufactured rail, and a third scenario which used a calculated residual-stress field from a cooling and roller-straightening analysis [79]. Only small differences were found, leading to the conclusion that the large axle-loads dominate fatigue life because any initial states of stress are redistributed after the first wheel passages. It remains to be demonstrated that the same situation prevails with lighter axle-loads.

On the other hand, a clear connection has been demonstrated between fatigue resistance in bending (both vertical and transverse) over 5×10^6 cycles, with the mean residual stress at the rail foot and edge being added to the mean applied stress [80]. The magnitudes of the residual stresses in roller-straightened rails become larger with stronger rails, leading to web fracture both before and in service [81,82], with the effects being exacerbated at the cut ends where the stress intensity at an existing defect can cause the crack to propagate.

In some cases, the rail-head after straightening is hardened by induction heating and rapid cooling using compressed air or water spray, or even cooling rapidly immediately from the rolling heat by dipping the whole head into a coolant-bath to obtain fine pearlite [83]. This accelerated cooling is followed by a second straightening operation. These processes leave a longitudinal residual stress which is tensile in the head and foot, peaking at about 200MPa, balanced by a compressive stress in the web (Fig. 7). This distribution of residual stress remains largely unchanged during service [84]. During the 1990s, Voestalpine developed the “head special hardened” process in which the whole length of the hot-rolled rail is dipped into the heat-treatment bath immediately after rolling. This results in a fine, relatively uniform pearlite, which enhances many of the properties required for high-performance rails [54].

2.2. Flash butt-welding

Rails are produced in lengths up to ≈ 120 m so installation necessitates a method of joining the segments. This was done originally using bolts and fishplates but the method is largely abandoned because of the costs of maintenance, cracking due to stress concentration at the bolt holes, and the gaps between the bolted segments cause the periodic “clickety-clack” sound as wheels traverse the

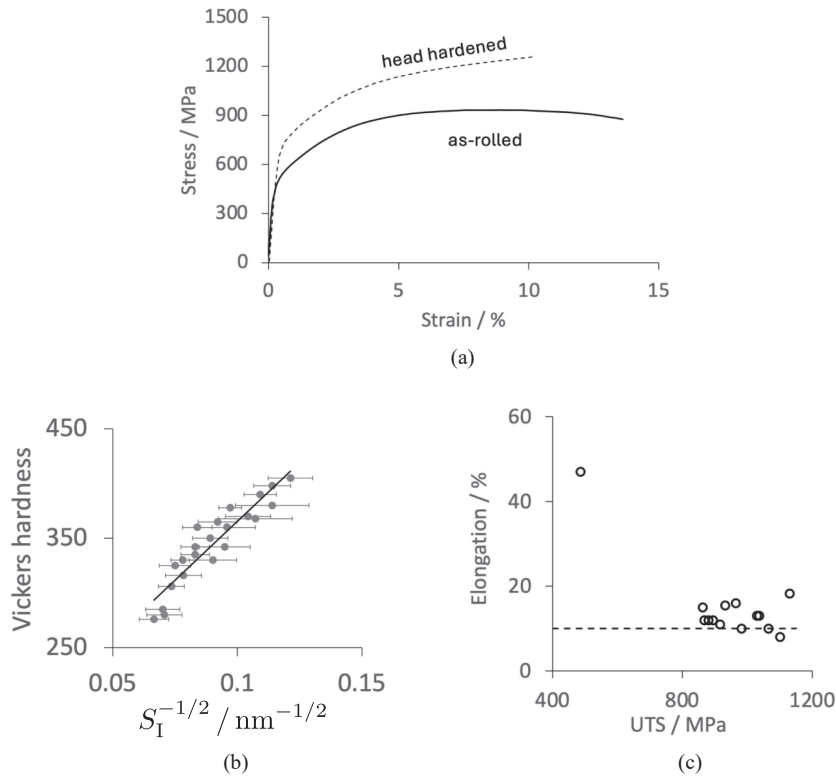


Fig. 6. (a) Stress–strain curves from tensile tests conducted on the head of as-hot-rolled rail with the dashed curve representing a head-hardened rail. Compiled using data from [65,66]. The elongation data have sometimes been corrected to remove the elastic part of the σ - ϵ curve, which often includes machine deflection. The dashed line refers to a 10% elongation often quoted in specifications. (b) Hardness as a function of $S_I^{-1/2}$, using rail steel data due to Perez-Unzueta and Beynon [52]. (c) Compilation of strength and elongation data on a variety of rail steels [65–74]. The data come from individual tensile tests conducted on the head of the rail, rather than the minimum specified values that often are quoted in the literature.

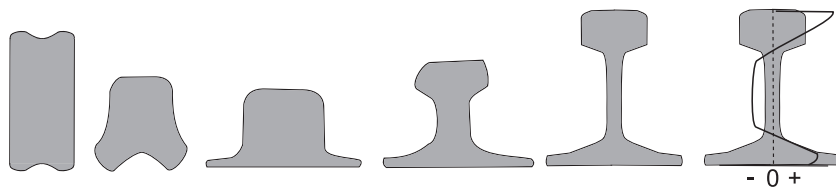


Fig. 7. Schematic illustration of the evolution of the rail-section during hot-rolling. Only a few of the 15 or so steps are illustrated. The final figure on the right shows schematically, the longitudinal residual-stress profile left within the rail following manufacture.

joint. The sound is tolerable but it is a manifestation of impact between the wheel and rail at the joint. Modern rails are mostly joined using flash butt-welding, a process developed originally at the E. O. Paton Electric Welding Institute in the USSR. But in climates where large temperature differences occur, thermal expansion and contraction can lead to long-range distortions in continuous, welded rails. Therefore, the rails are laid such that they are in tension to counter the effects of thermal strains. For a temperature range -5 to 30°C , the tensile stress within the rail laid at an intermediate temperature in this range, is of the order of 10 – 15 MPa [85]. A 15 MPa stress would cause an elastic strain of $\approx 7 \times 10^{-5}$. If the expansion coefficient is $12 \times 10^{-6} \text{K}^{-1}$, then a variation of $35/2^\circ\text{C}$ would lead to a thermal strain of $\pm 2.1 \times 10^{-4}$, which would not be compensated by the prestressing but might be tolerable.

During flash butt-welding, aligned segments of rails are heated locally by the passage of an electrical current (*flash*) across the gap between the touching rail-segments, until melting occurs, when the segments are forced together (*upset*) in a direction parallel to the rails. The contact surfaces therefore become intimately bonded, with sufficient displacement to ensure that some material is expelled away from the joint. This helps ensure intimate contact between the rails and in reducing oxide entrapment. The expelled material is then ground off in stages to produce a neat joint replicating the contours of the adjacent rails. The electrical pulses during welding can be managed to deliver controlled bursts of energy. Pre-heating pulses can help raise the temperature of the segments before the main flash is applied, in order to reduce the forces during upsetting or for controlling the cooling rate after the upsetting is completed so that

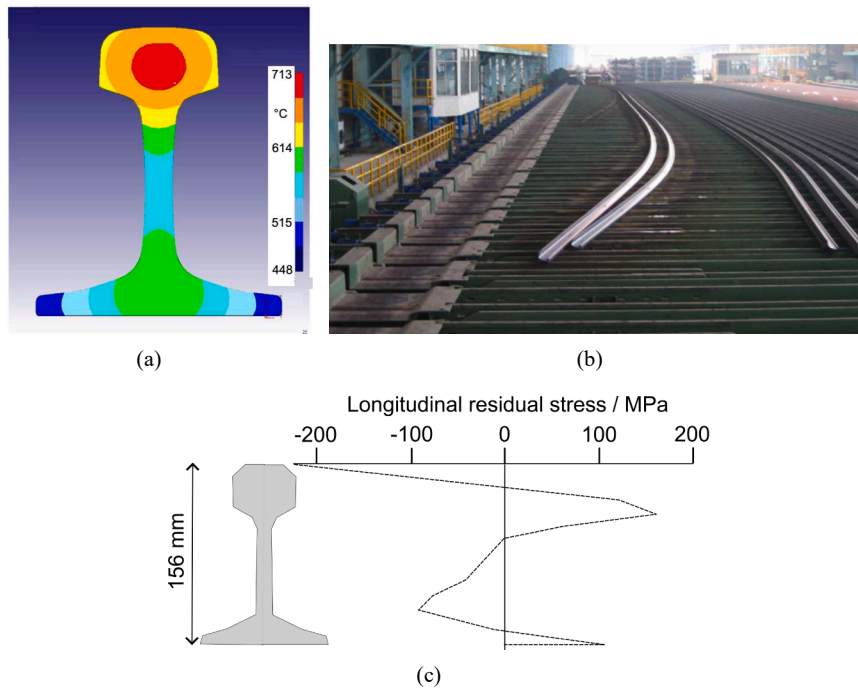


Fig. 8. (a) Calculated temperature field of heavy rail following cooling for 800s after rolling. (b) Because the cooling is not uniform, the rails bend as the temperature decreases. The rails on the right are relatively hot. (a,b) are adapted from Chen et al. [78] with permission of Springer Nature. (c) State of residual stress when a rolled rail passes through a straightening machine consisting of six rollers, three at the bottom and three at the top. The latter were set to impart vertical deformations on the rail by 10, 7 and 4 mm. The measurements were made at a distance 1.6 m from the entry end of the rail. Adapted from [77].

the microstructures in the heat-affected zones can be optimised. With strong rails, it is found that a reduced heat input helps optimise the integrity of the weld [85,40]. Even the implementation of the flash component can be pulsed [85]. Contoured induction heaters are sometimes applied to provide a heat-treatment to the finished joint in order to improve properties and microstructures [86].

If the molten region, which will contain oxides, solidifies too quickly then it will not be removed completely by the mechanical upsetting. Fig. 9 shows that the measured temperature reached as near to the abutting surfaces as experiments permit, may actually be less than that at which the steel becomes completely liquid [87] (Table 2). There is in fact a small gap between the “abutting” surfaces which are, during flashing, put in contact and again slightly separated, while the electrical potential between the rail segments is maintained constant. During these repeated short detachment phases, multiple electrical arcs form between the surfaces. Localised events occur where steel in the immediate proximity is rapidly heated to temperatures well above melting – this largely is expelled from the weld gap because of the explosion-like local events [88]. The flash stage continuously generates sufficient heat in the steel close to the fusion surface, raising the temperature close to melting. This sets the scene for the abutting surfaces to be forged together in the upsetting stage.

Surface preparation prior to welding is not required because the flashing and displacement can in combination remove contaminants, although the contact surfaces should be clean enough to apply the electrical current. The equipment used on-site is illustrated in Fig. 10a with some example process-parameters listed in Table 3. The preheating pulses before the flash help raise the peak temperature achieved prior to the displacement.

Flash butt-welding now accounts for some 80% of rail welds in the world [90] and is recognised as a process that generates welds of high quality [40].

One goal is to avoid a large change in hardness across the weld junction, but metallurgical changes are inevitable in the heat-affected zones [91]. Fig. 11a illustrates both microstructural and hardness variations across the flash butt weld on a pearlitic rail steel. It is interesting that the coarsest austenite grains generated towards the central region of the joint result in the finest interlamellar spacing, similar to that of the base plate, on cooling, because the large grain size enhances hardenability so the transformation during cooling is suppressed to lower temperatures. The partially-austenitised region cools to a relatively soft mixture of pearlite and spheroidised cementite, the latter in regions that did not become austenitic at the peak temperature. The microstructures illustrated in Fig. 11b-c represent the web region of a similar flash butt weld; the degree of spheroidisation in the intercritically annealed region (262 HV) is remarkable [92].

There is, therefore, an undesirable hardness dip in that region which may during service lead to localised plasticity; the softened region is estimated to lead to a reduced rolling-contact fatigue life. What is not clear is how to avoid the softened zone given that there always will be temperature gradients created that leave some regions in a partially austenitised condition during the heating stage.

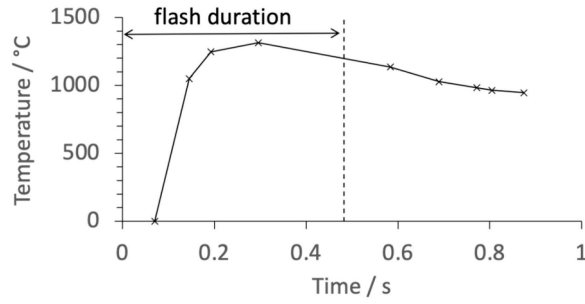


Fig. 9. Measured temperature in the closed proximity of welding face of rail during the flash component of the electrical butt-welding process. Selected data from Weingrill et al. [87].

Table 2

Phase diagram calculations [89] of the melting temperature at which the steel is completely liquid (T_M) and the mass fraction of liquid at 1400 °C.

	Composition / wt%	$T_M / ^\circ\text{C}$	Fraction liquid, 1400 °C
R260	Fe-0.71C-0.3Si-0.95Mn	1473	0.15
R350	Fe-0.76C-0.3Si-0.95Mn	1468	0.20
R400	Fe-0.97C-0.3Si-1.15Mn	1454	0.39

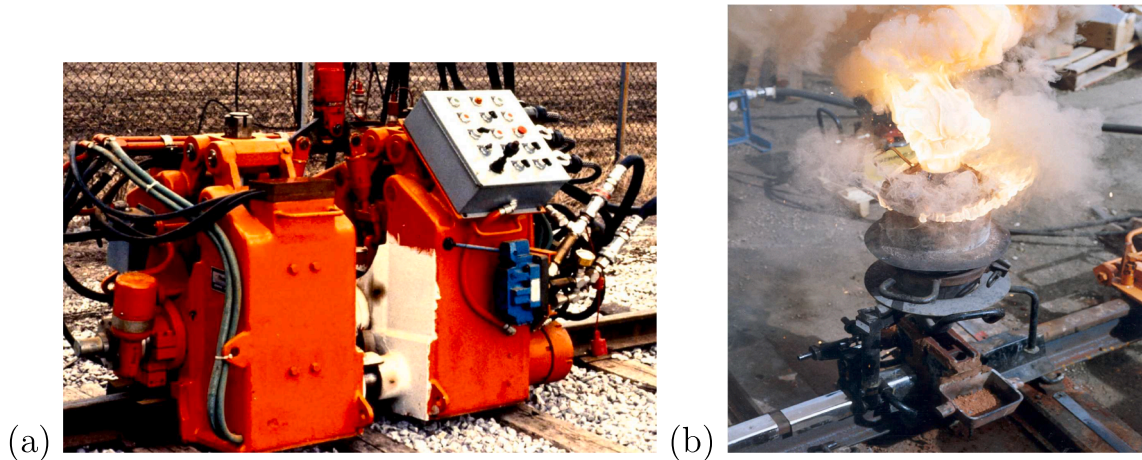


Fig. 10. The joining of rails during installation or repair, using (a) flash butt welding, and (b) thermit welding. Images courtesy of Howard Smith.

Table 3

Example of flash butt welding parameters, data from Porcaro et al. [91].

Parameters	Values	
Intensity and duration of initial flash	77.4 kA	20 s
Number of preheat current pulses and pulse duration	10	3.8 s
Intensity of preheat pulses	45–70 kA	
Force during preheating pulses	106 kN	
Intensity and duration of final flash	38.3 kA	14.4 s
Final force	477 kN	
Total displacement	37–45 mm	

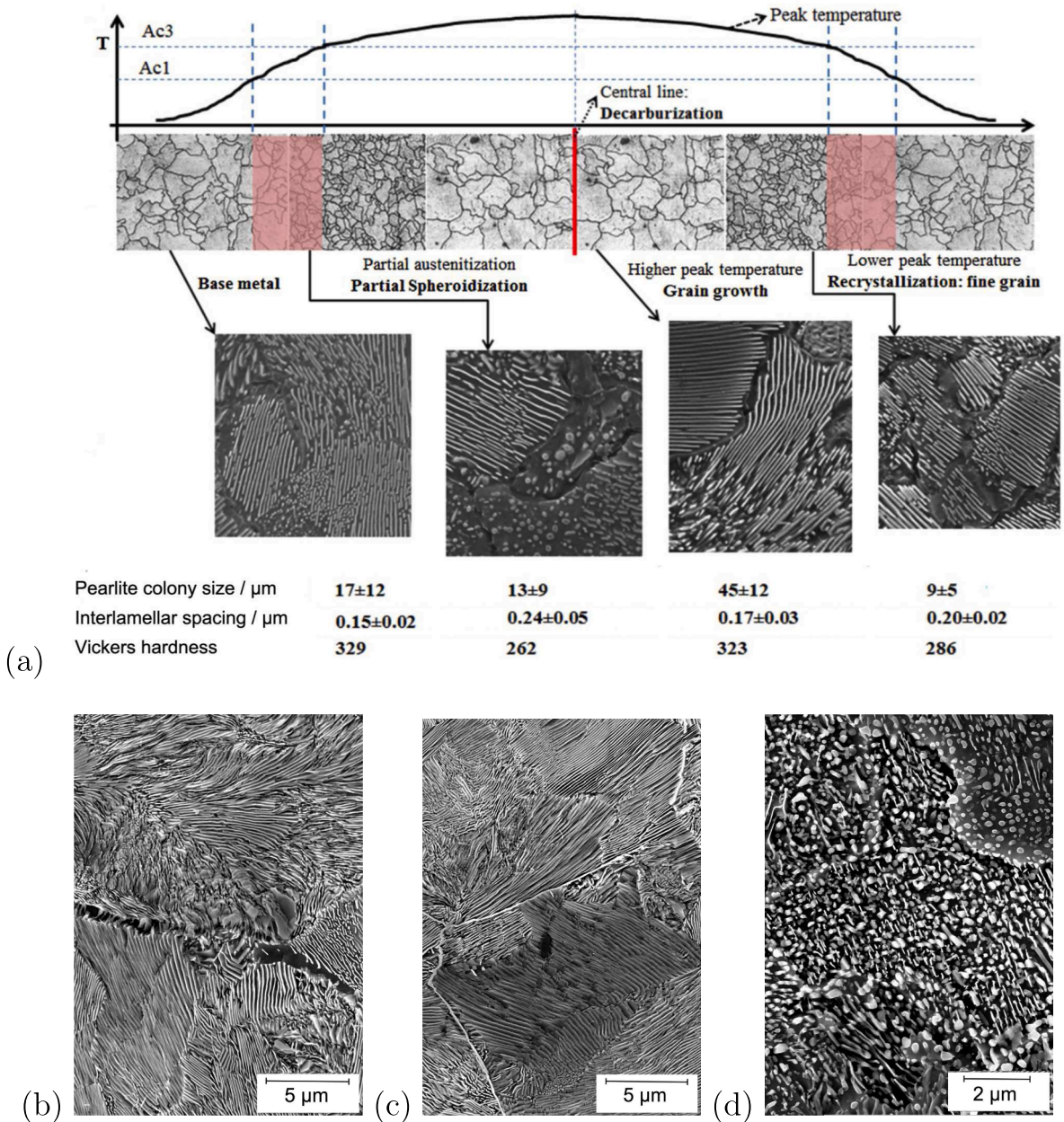


Fig. 11. (a) Changes in microstructure and hardness across a flash butt weld on a rail of composition Fe-0.72C-0.84Mn-0.24Si-0.08Crwt%. The upper micrographs are thermally etched. The metallographic observations were made on the rail head, about 10 mm below the surface. Figure reproduced from Porcaro et al. [91] with permission of Elsevier. (b-d) Changes in microstructure in the web of Fe-0.79C-1.01Mn-0.22Si-0.24Crwt% rail due to flash butt welding. (b) Weld centreline. (c) At a position where the A_{c3} temperature is reached. (d) At a position where the material is intercritically annealed. Images courtesy of Henrique Boschetti Pereira, described in detail in [92].

One solution would be to explore methods of making the softened zones narrow, with the width being specific to the expected axle-load; the constraint from the harder adjacent regions might then prevent the localised plasticity. Another speculative suggestion is to surface harden the softened zone using techniques such as laser hardening, shot peening or cladding.

Modern flash butt welding machines can operate in either the continuous flashing or pulsed flashing mode, with the latter generally associated with a narrower softened zone; in one study the width of this zone was reduced by a factor of two from 80 to 40 mm with the application of pulsed flashing [93]. The flash butt welding process provides the flexibility to adjust the preheating conditions to ensure that the ends of the two rails that are upset and forged are heated to the required temperature as rapidly as possible, while minimising the heat transfer into adjacent regions of the rail.

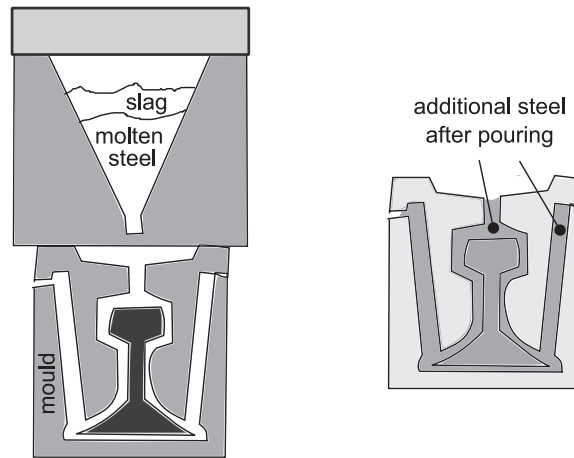
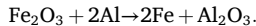


Fig. 12. A ceramic mould is assembled around the rail segments to be joined. The aluminothermic reaction at the top then creates the molten steel covered by a layer of slag, which then is released into the mould. The gap between the rail segments becomes filled with steel (some melting also occurs of the rail segments), thus creating the weld on solidification. The welded region is then contoured by grinding to the required rail profile.

2.3. Thermite welding

This igneous process of welding rails essentially creates a cast weld with heat generated by a reaction of aluminium and iron oxide; the reaction is intense so molten steel is created, which then fills the pre-assembled mould surrounding the rail segments. There will also be some localised melting of the surfaces of the rails within the mould. Solidification results in a weld, with some preparation afterwards to maintain a correct profile at the joint. This is a long-established process which is mobile so amenable to all locations, and has served well for more than a century, with the first rail welded in Essen, Germany in 1899 [94–96] (see Fig. 12).

During thermit welding, aluminium powder reacts with iron oxide to generate molten iron in an exothermic process, Fig. 10b, via the reaction



with an enthalpy change of -16.5kJ cm^{-3} at 298K, which is roughly twice the volumetric energy density of the explosive trinitrotoluene [97]. A pre-formed refractory mould is assembled over the gap between adjacent rails so that the molten metal fills the gap. There are additions to the mixture that result in an alloy of the desired chemical composition on melting, resembling that of the rail itself. The reaction proceeds following induced ignition of the powder mixture to achieve temperatures of the order of 2500°C . After solidification, the mould and excess steel are removed from the tops of the rail with a hydraulic trimmer, and the cold joint is then ground to generate the rail profile. There will be inevitable peak-temperature gradients from the centre of the weld, leading once again to a softened zones where the pearlite has been partially austenitised [98], as in flash butt welds. The softened zones are generally wider than in flash butt welds, but shortening the preheat period during thermit welding helps mitigate the problem. Sometimes, alloying additions are made to the thermit mixture to optimise the properties of the weld metal.

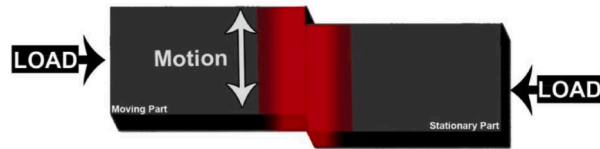
The consequences of a soft zone in welded rails must be assessed in terms of service requirements. At the running surface, the softened zone in flash butt welds generally does not present any concerns with excessive deformation or dipping provided the hardness in the reaustenitised zone is equivalent or slightly above that of the parent rail. However, at the gauge corner, particularly under curved track conditions, where the conditions are more severe (higher contact stresses and surface creepage forces), increasing the risk of surface damage [99].

2.4. Linear friction-welding

With the aim of achieving a weld strength close to that of the rail and minimising any softened region in the heat-affected zone, a friction welding process has been developed for the joining of full-size rail segments [100]. During *linear* friction-welding, two flat surfaces of the segments to be joined are forced into contact by applying a load in the direction normal to the surfaces. One of the segments is held stationary while the other is rubbed repeatedly via a reciprocating motion parallel to the abutting surfaces. This generates frictional heat that plasticises the steel in its vicinity, with material expulsion due to the load-induced forging, and part movement creating a clean joint from the resulting fresh surfaces [101]. The heat generation is given by

$$q' = \mu_f P v_r \quad (2)$$

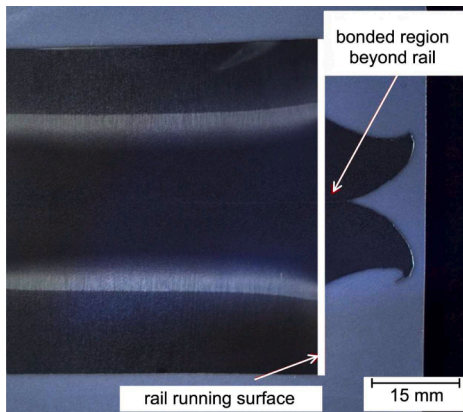
where q is the heat flow (W m^{-2}), P is the contact pressure, v_r (m s^{-1}) is the relative velocity and μ_f is the friction coefficient which may depend on temperature, velocity and pressure [102]. The process is sometimes known as *vibrational welding* because it can join non-axisymmetric workpieces [103], which makes it suitable for the joining of rails. It is important, of course, that when the process is



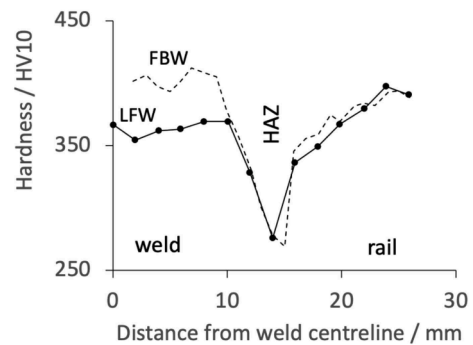
(a)



(b)



(c)



(d)

Fig. 13. (a) Schematic representation of the linear friction-welding process. (b) An actual joint between rail segments, produced using linear friction-welding, with the flash resulting from the expulsion of material from the joint still in place. (c) A macroscopic section from weld. (d) Hardness profile; the dashed curve is from a flash butt-weld [106], for comparison with the friction method. The commercial designation of the rail is 136RE. Images and selected data from US Department of Transportation report [100] that has no copyright restrictions.

completed, the rails are accurately aligned, so the machine is computer controlled.

The process is illustrated schematically in Fig. 13 together with an actual weld of cross-sectional area 85.8 cm². The reciprocating motion frequency was 45 Hz, amplitude 11.5 mm, initial pressure ≈ 26 MPa, and a forging pressure of ≈ 70 MPa. The rails were preheated to 260 °C prior to welding, presumably to avoid as far as is possible, the formation of martensite. All stages of the welding operation could be completed in about 2 min.

Rail alignment at the head was shown to result in a vertical offset of 0.76 mm, a horizontal offset of 1.3 mm and the rail base was offset by 3.2 mm, all assessed to be satisfactory. Macroscopic metallographic examination of joint sections showed that the segments were fully fused with the joint continuing a small distance into the flash, which is good because the integrity is preserved after grinding off the flash. The microstructure of the weld was found to be predominantly fine-pearlite and small amounts of martensite. The hardness variation still shows a significant softening within the heat-affected zone of the weld. The width of the softened zone seems comparable to that obtained in flash butt-welding [91] so linear friction-welding does not seem to offer an advantage in that respect; a comparison is presented in Fig. 13d.

An experimental investigation of small rail steel (≈Fe-0.7C-0.25Si-1.25Mn wt%) samples joined using linear friction-welding found predominantly martensite with hardness reaching ≈ 800 HV and no softened region in the heat-affected zone [104]. However, such levels of hardness and large amounts of martensite make the weld brittle with a recorded elongation of < 1 % and premature failure in tension at ≈ 640 MPa. To ameliorate this, the joints were reheated to 900 °C for 3 min followed by air cooling, to generate a

microstructure of pearlite and Widmanstätten ferrite with a uniform hardness across the joint of about 300HV. Such a treatment is impractical in practice when joining rails.

To avoid martensite in the linear friction-weld, it has been recommended to preheat a steel such as R260 rail up to 350 °C and possibly even increase the welding time [105].

2.5. Orbital friction-welding

In this solid-state process, both of the rail segments are held stationary but the joint is made by using an eccentrically rotating steel disc in between the segments, to generate the heat and form the joint [107]. The goal again is to reduce the extent of heat-affected zone softening. In modelling the process for a particular rail profile (“UIC 60”), the disc is set with a diameter of 0.3m and a thickness of 0.03m, and presumably would be of a comparable chemical composition to the rail (Fig. 14).

It does not appear that there have been any full-scale trials of the process, though it is clear that preheating would be required in order to reduce the cooling rate sufficiently to avoid the formation of martensite [102].

2.6. Friction Stir Welding

Friction stir welding is a solid-state, hot-shear joining process [108–111], [chapter 3, 112] in which a rotating tool with a shoulder and terminating in a threaded pin, moves along the butting surfaces of two rigidly clamped plates placed on a backing plate as shown in Fig. 15a. The shoulder makes firm contact with the top surface of the work-piece. Heat generated by friction at the shoulder and to a lesser extent at the pin surface, softens the material being welded. Severe plastic deformation and flow of this plasticised metal occurs as the tool is translated along the welding direction. Material is transported from the front of the tool to the trailing edge where it is forged into a joint.

The astounding success of the process in the context of aluminium alloys [114] has naturally stimulated exploration of its applicability to other materials such as steel, titanium, magnesium, nickel and copper alloys. There is a “conceptual” study of the friction stir welding of rails [113] that reaches the perhaps surprising conclusion that the process is viable and with a reduction in cost when compared with flash butt-welding, thermit and other less common methods. The work, however, appears to be simplistic in its interpretation of the capabilities of the process. There does not seem to be an accounting for the cross-sectional geometry of rails that have to be welded, with translation of the tool on the top surface only, so it might assume that the whole rail can be joined without making the tool follow the detailed profile. There is no indication of the depth of the weld expected, which cannot conceivably penetrate the whole cross-section section. The costing is flawed, with no account taken of the cost of the tool, which is a major omission given the hot-strength of steel which wears expensive tools quickly [115,116]. The process has not been particularly successful when applied to ordinary steels, for these very reasons.

2.7. Alloy design

The steel used in the manufacture of rails must, above all, be able to resist rolling-contact fatigue and wear; it should also be weldable. Naturally, it must be capable of mass production in long dimensions at a reasonable cost.

Pearlite has a complicated three-dimensional shape. It does not consist of parallel, flat, alternating plates of ferrite and cementite, but has convoluted three-dimensional form with features such as branching, twisting and the passage of ferrite through the cementite [117]. Each θ -lamella has curvature and contains holes through which ferrite permeates, so it can appear to terminate in two-dimensional sections while others sharing the growth front continue unabated [118–120]. Therefore, any spacing that is measured is an imperfect representation of the real structure. It is likely, nonetheless, that the spacing S_1 between adjacent lamellae observed on two-dimensional sections will correlate well with macroscopic properties, given that such measurements represent the collective behaviour of a polyphase, polycrystalline sample.

In this context, the strength of pearlitic rails, whether expressed in terms of macroscopic tension-tests or hardness values, is dependent mostly on the interlamellar-spacing achieved in the final state of the rail. Solid-solution strengthening, for example by silicon additions, can make a small contribution to the strength of ferrite [121–124]. The rail steel R260Mn has $S_1 \approx 0.15 \mu\text{m}$ and contains 1.4Mn-0.29Siwt% [125]. The yield strength from just the pure iron and interlamellar spacing is given by $\sigma_y = 174S_1^{-\frac{1}{2}} + 128 \text{MPa}$ [124] where the units of the spacing are expressed in micrometres; therefore, the contribution due to S_1 alone comes to 450MPa. Using carefully determined solution-strengthening data for ferrite from [126], the contributions of manganese and silicon amount to just $1.14 \times 37 + 0.29 \times 106 = 83 \text{MPa}$.² The solubility of silicon in cementite is close to zero but manganese can dissolve in large concentrations [127]; however, information on its contribution to the strength of cementite is absent.

A fine interlamellar spacing can be achieved by suppressing the transformation temperature. Alloying with substitutional solutes can be effective if as a result, greater undercoolings can be achieved before pearlite forms [128,129]. However, a fine spacing is best achieved by nurturing the transformation of austenite during accelerated cooling. This works because a greater amount of free energy is available to cope with the creation of a larger density of ferrite-cementite (α - θ) interfaces at enhanced undercoolings below the

² There are many empirical expressions claiming to represent the solution strengthening terms, but are not well-founded because they neglect structure or the strength contribution from the iron itself.

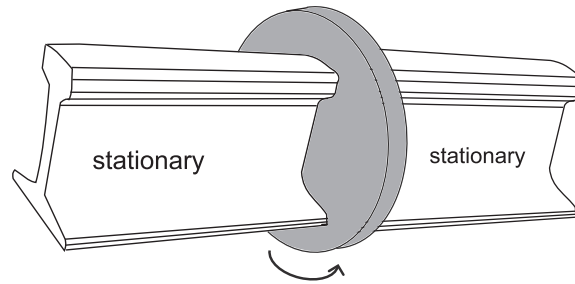


Fig. 14. Schematic illustration of the orbital friction-welding of stationary rails.

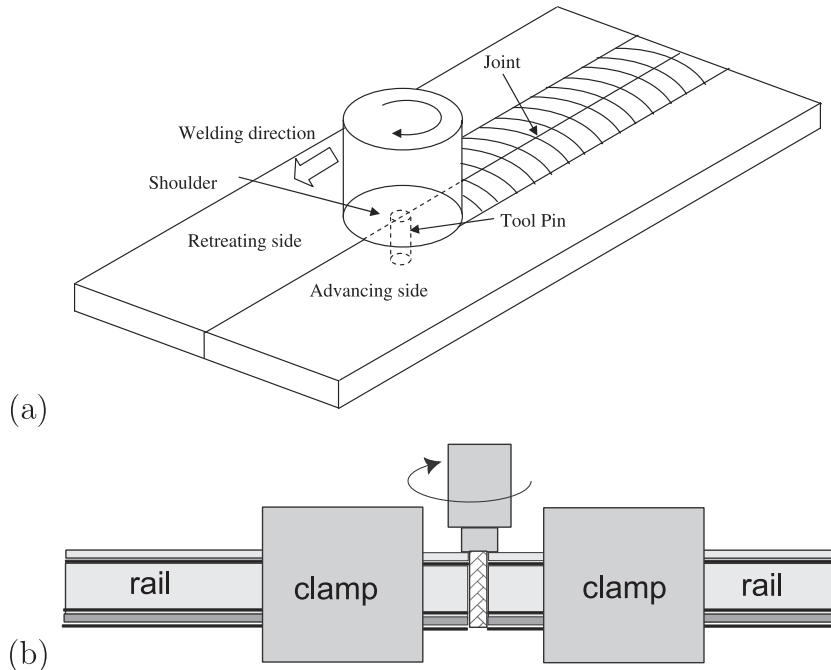


Fig. 15. (a) Schematic illustration of the friction stir welding process. (b) Schematic of machine proposed for friction stir welding of rails, a much simplified version of the detailed diagrams available in [113].

eutectoid temperature. Alloying additions that increase the free energy change for the reaction $\gamma \rightarrow \alpha + \theta$ at a given temperature, will have the same effect [119,130,131].

It is worth noting that rails have large cross-sections with a profile that cannot guarantee uniform cooling; the cooling rate can also vary along the length of the rail when placed on the cooling platform after hot rolling [132]. As a result, both the structure and properties will vary with position [133,56,71]. This applies also to heat-treated rails [134]. From the point of view of service conditions, it is the head of the rail that determines service life. It has even been argued that a heat treatment process needs to be developed that allows hardness gradients to develop on the rail-head, such that lateral wear can be reduced [135].

The alloy composition must permit the formation of a fully pearlitic microstructure in a eutectoid steel that is air-cooled at reasonable rates after hot-rolling. A typical rail steel will contain about 0.8wt% of Mn and not much of any other hardenability enhancing alloying element. Depending also on the austenite grain size, this can lead to a fully pearlitic microstructure if the cooling rate is maintained $\leq 4^\circ\text{C s}^{-1}$ [136]; this is confirmed by the continuous cooling transformation (CCT) diagram in Fig. 16a. In eutectoid rail steels containing 0.8–1.2Mnwt%, the bainite-start temperature during isothermal transformation is found to be about 520°C [137]. This means that the cooling cycle for the rail should be such that pearlite formation is complete above this temperature in order to avoid bainite; in Fig. 16a, the cooling rate 1°C s^{-1} clearly leads to the completion of the pearlite transformation at a temperature well above 520°C , whereas 5°C s^{-1} does not. Small concentrations of alloying elements such as chromium can greatly reduce the cooling rate required. The cooling rate is not constant, so the best approach is to generate a continuous cooling transformation diagram.

Fig. 16b is an interesting study on how hot plastic-deformation of the austenite affects the phase transformations in rail steels. Although the austenite in rail steels is in a recrystallised state after hot-rolling or after reheating, such deformation may be relevant in flash butt-welded segments which will transform after the upsetting operation. From a fundamental point of view, reconstructive

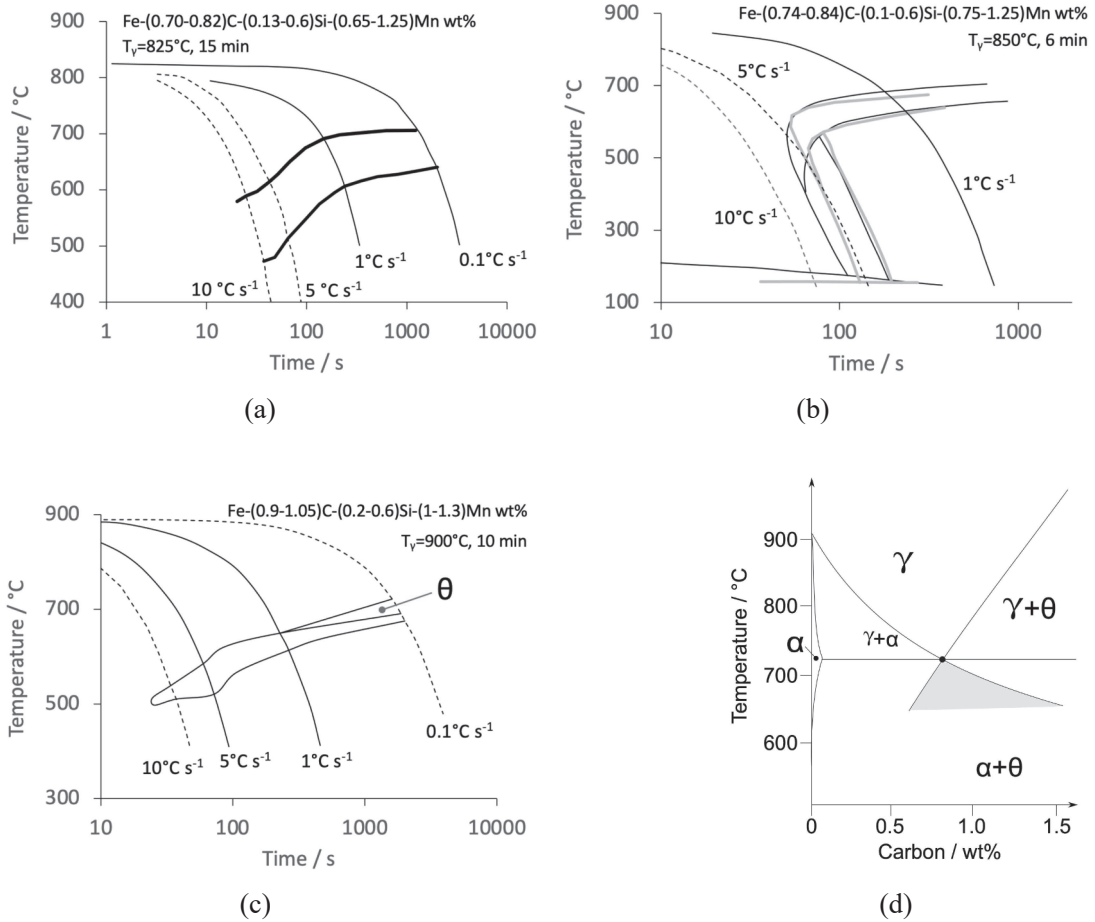


Fig. 16. Continuous cooling transformation diagrams for some rail steels, the exact compositions are not available, nor the austenite grain sizes, in the original publications. In all cases, dashed cooling curves lead to ultimate microstructures that are not fully pearlitic, whereas the other such curves lead only to pearlite. (a) For “R350LHT”. Adapted using selected data from Yuryev et al. [138]. (b) The CCT curves for the undeformed austenite and when deformed (in grey colour) in compression so that the maximum diameter in the barrelled region is increased by 36%. Adapted using selected data from [139]. (c) Hypereutectoid “R400HT” steel. Adapted using selected data from Chen et al. [140]. (d) The shaded region between the two extrapolated boundaries represents the domain into which hypo- or hyper-eutectoid steels must be supercooled in order to obtain a fully pearlitic microstructure.

transformations including pearlite are accelerated when the austenite is a deformed state, because transformation destroys any defect structures, thus providing an additional driving force. Displacive transformation are retarded when the austenite is in a severely deformed condition, because the defects get in way of the glissile γ/α interfaces, a process known as mechanical stabilisation [141–144], [p.314, 131]. Consistent with this Fig. 16b shows that both the bainite and martensite transformations from deformed austenite are markedly retarded, whereas pearlite is less affected.

When dealing with hyper- or hypo-eutectoid steels, it is necessary to undercool the steel below its eutectoid temperature in order to generate a fully pearlitic microstructure, without any proeutectoid α or θ . Fig. 16c shows the range of cooling rates available to avoid anything but pearlite is reduced in the hypereutectoid rail steel. Slow cooling rates can induce the precipitation of proeutectoid cementite. For pearlite to form it is necessary to be able to simultaneously precipitate both of its constituent phases; this only is possible if the alloy is supercooled into the region between the extrapolated $\gamma/\alpha + \gamma$ and $\gamma/\theta + \gamma$ phase boundaries [145,146], Fig. 16. Proeutectoid cementite at the austenite grain boundaries is known to be detrimental to the mechanical properties in rail steels – it contributes to the development of rolling contact fatigue in rails [147]. An increase in the silicon concentration to about 1 wt%, and cooling at a sufficiently large rate through the temperature range where precipitation at the austenite grain boundaries occurs prior to the onset of pearlite, is effective in suppressing the precipitation of proeutectoid cementite in hypereutectoid steels [148,149].

The eutectoid temperature can be estimated using an empirical equation by Andrews, here presented for the alloying elements common in rail steels [150]:

$$T_E / ^\circ\text{C} \approx 723 - 10.7w_{\text{Mn}} + 16.9w_{\text{Cr}} + 29.1w_{\text{Si}} \pm 12^\circ\text{C} \tag{3}$$

and each wt% (w) of molybdenum is assumed here to contribute the equivalent of 1.5Cr wt%, as associated with welding [151]. It is emphasised that the eutectoid temperature is defined uniquely only for a binary Fe-C steel; in substitutionally-alloyed steels there will exist a temperature range within which $\alpha + \gamma + \theta$ can coexist in equilibrium. The best way to deal with this is to use routinely available computer software and thermodynamics databases to calculate the phase diagrams for multicomponent steels.

Takahashi [152] derived the following empirical equation from published experimental data on interlamellar spacings, to cover a range of substitutionally alloyed steels as a function of temperature ($^{\circ}\text{C}$):

$$\log\{S_I/\mu\text{m}\} = -2.21358 + 0.09863 \underbrace{w_{\text{Mn}}}_{0-1.8} - 0.05427 \underbrace{w_{\text{Cr}}}_{0-9} + 0.03367 \underbrace{w_{\text{Ni}}}_{0-3} - \log\left\{\frac{T_E - T}{T_E}\right\} \quad (4)$$

with temperature in the range 600–790 $^{\circ}\text{C}$. It becomes possible using these two equations to estimate the expected interlamellar spacing of pearlite, assuming that $T_E - T = 27^{\circ}\text{C}$ for rails that are air-cooled after hot-rolling, and $T_E - T = 52^{\circ}\text{C}$ for those that are re-austenitised and cooled rapidly using compressed air, the so-called heat-treated rails, Fig. 17a.

Fig. 17 shows that the hardness can be represented reasonably well in terms of the Hall–Petch function of interlamellar spacing, yielding the following relationship:

$$\text{HV} = 2152S_I^{\frac{1}{2}} + 150 \quad (5)$$

which explains about 86% of the variation in observed hardness. There has, over the years, been some discussion about the relationship between the interlamellar spacing of pearlite and its strength [155–157]; however, a detailed analysis of data has shown that the Hall–Petch relationship is the best and most physically meaningful representation of the strength of pearlite [124]. The constant in Eq. 1f has contributions from the strength of pure iron which is ≈ 100 HV at ambient temperature [158] together with solid solution strengthening terms. It follows that much of the hardness of a typical rail comes from the structure of pearlite, the interlamellar spacing.

2.8. Varieties of rail steels

2.8.1. As-rolled rails

Nine types of rails steels have become firmly established for conventional and high-speed tracks [159]. The actual designations vary by country but the essential features described below do not differ much; and many have equivalents in the variety of standards. For example, the grade “R200” in European and US standards is similar to the Chinese designation 50Mn. Rails can be categorised according to their carbon content or by their heat treatment, i.e., whether naturally-cooled after rolling or accelerated-cooled, Table 4.

The softest variety, R200 (as-rolled 0.4–0.6 wt% C), although used much in the past, is now rarely installed. Some applications remain in tram networks due to the ease with which it can be restored by in situ weld deposition, or in sections of track where wear abrades away any surface-initiated fatigue cracks [160]. Due to its low carbon-concentration and hardness (200–252 HV), it has good machinability and weldability, with a reduced tendency for foot-failure, attributed to low residual stresses and relatively high fracture toughness [161]. The microstructure contains significant quantities of soft allotriomorphic ferrite in addition to pearlite. Fig. 18a.

R220 has slightly higher carbon content (0.5–0.6 wt% C) and tensile strength. It is now substituted with R260 (0.62–0.8 wt% C), accounting for 90% of metros and mainline tracks. It has a predominantly pearlitic microstructure, Fig. 18b. There is much accumulated experience in the application and maintenance of R260 rails, but increased traffic density and reduced maintenance budgets have driven the use of harder varieties in curved sections of track that have a radius less than 3000 m. R260Mn has on average a reduced carbon concentration but a greater manganese level (0.55–0.75 wt% C, 1.3–1.7 wt% Mn) to improve toughness without compromising the hardness by maintaining the fine interlamellar spacing of R260; some countries specify a Charpy toughness of 40 J minimum, measured at 20 $^{\circ}\text{C}$. This alloy is considered suitable for high-speed traffic.³ R260Mn has a fully pearlitic structure obtained during cooling at $\leq 2^{\circ}\text{C s}^{-1}$, with the pearlite generated over the temperature range 624–547 $^{\circ}\text{C}$ [162]. Practical rail cross-sections that are 15.6 cm in height and 6.7 cm head-width, will cool slower (0.14–0.24 $^{\circ}\text{C s}^{-1}$), with the head region cooling fastest [163], in which case the transformation temperature range is likely to be in the range $T_E - 25 \rightarrow T_E - 50$.

R320Cr (0.6–0.8 C, 0.8–1.2 Cr wt%) is harder (≈ 320 HV) and more wear resistant but increases the wear of wheels [164], but this adversely affects weldability and weld-repair, for example requiring a minimum time to cool between 800 and 500 $^{\circ}\text{C}$ of 18 min, and therefore, a post-heating treatment [165]. All this makes it less competitive against heat-treated grades [166]. The harder a rail is, the greater is the reduction in hardness ΔHV of the rail hardness HV_{rail} and that of the the softest region (HV_{soft}) of a flash butt weld, as illustrated in Fig. 19. This might be expected because the further the microstructure deviates from equilibrium in a harder rail, such as by possessing a finer pearlite, the greater is the driving force for recovery during tempering.

³ Where the speed exceeds 250 km h $^{-1}$. The rail steel used depends on the detailed characteristics of the route, the type of damage expected and the desired inspection and repair cycles [e.g., 54]

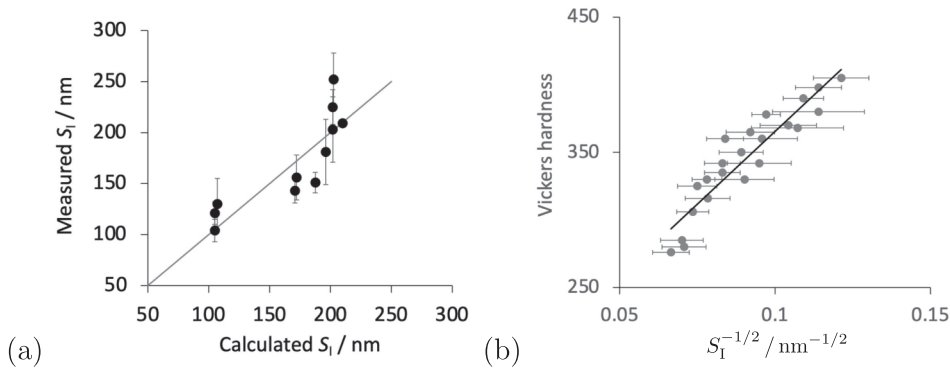


Fig. 17. (a) The interlamellar spacing of pearlite, with measured values plotted against those calculated using Eqs. 1d and 1e. Data from [19,153,154]. (b) Hardness as a function of $S_I^{-1/2}$, using rail steel data due to Perez-Unzueta and Beynon [52].

2.9. Heat treatment of rails

The primary aim of heat treatment is to condition the properties of the rail head by refining the pearlite interlamellar spacing. The details vary and are mostly proprietary, but typical conditions include heating the rolled rail to about 900 °C for 50 min and passing it through a chamber containing a series of symmetrically placed air jets, Fig. 20, which also shows the hardness distribution in the rail-head following cooling [170]. The air pressure used was 0.26 MPa with the jets of air at 28 °C located 15 mm from each surface. The final microstructure was fully pearlitic. The ordinary hardness of U75V rail is 350 HV [171] with values reaching 376 HV following the heat-treatment. This is an illustrative case and details of the heat treatment and hardness improvement achieved will vary with steel composition and the technology implemented for cooling. In the case of R260 which normally is not heat-treated, the hardness increment is larger, from 285→342 HV [172].

Induction heating followed by cooling using jets of air–water mixtures is used in some cases to surface harden the rails [173,174]. Water-polymer mixtures can be used and in some cases, whole rails might be immersed into a cooling bath (p. 18). However, all heat treatments which require separate heating after the rail has cooled, or induction heating as an off-line process, reduce productivity. So, energy-efficient modern practice is to conduct any accelerated cooling as the hot rail emerges from the rolling process [174], with any straightening applied after this in-line heat treatment.

2.9.1. Heat-treated rails

The heat treatment of rails almost always is designed to refine the pearlitic microstructure, taking care to avoid undesirable constituents such as martensite. This usually is achieved by controlled accelerated-cooling using jets of air, the details of which are proprietary.

R350HT (heat-treated 0.72–0.8C wt%) has a similar chemical composition as R260 but is cooled more rapidly to refine the interlamellar spacing of pearlite, resulting in an increase in hardness from \approx 310 HV for heat-treated R260 [175] to a minimum of 360 HV for R350HT, leading to a threefold increase in wear resistance and better rolling-contact fatigue resistance [45]⁴. It is therefore the most common premium grade in European tracks [166].

R350LHT (heat-treated 0.72–0.8C–0.3Cr wt%) is essentially R350HT with added chromium to refine further the interlamellar spacing. It has limited application outside of the Swiss network, because it does not show a significant improvement in gauge-corner wear resistance, nor on rolling-contact fatigue crack development [31]; there also are difficulties during wear repairing and a tendency associated with its greater hardenability, to generate non-pearlitic microstructures in the heat-affected zone. R370CrHT (heat-treated 0.7–0.82C, 0.4–1.0Si, 0.4–0.6Cr wt%) is similar to R350LHT but with added silicon and more chromium to achieve an even finer interlamellar spacing with increased hardenability. Despite needing careful cooling control as well as special welding procedures, thermit and flash butt welding can be performed satisfactorily, but weld repairs are very challenging for this grade. The high wear and RCF resistance of this alloy are targeted towards heavy-haul tracks or heavily trafficked tight radii curves.

R400HT (heat-treated 0.9–1.05C, 1.0–1.3Mn, wt%) is a hypereutectoid variant of R350LHT with enhanced manganese, meant for the most severe loads and curve radii due to its high resistance to wear and rolling contact fatigue [177,178]. Its hardness in the hot-rolled condition is about 350 HV but increases to \approx 410 following heat treatment that ensures a cooling rate of 3→3.5 °C s⁻¹, leaving it with a refined, fully pearlitic microstructure [179]. It is prone to form proeutectoid cementite at the austenite grain boundaries, which is known to be deleterious to RCF (Section 6.7) having to rely on careful cooling to avoid this phase.

⁴ On tracks with a curve radius less than 1000 m, R350HT has been reported to be more susceptible to the penetration of grinding-initiated cracks into the body of the rail when compared with softer varieties of rails [176].

Table 4

Chemical composition in wt% of the most common rail steels. *STD* stands for standard, *HH* for head hardened, *HT* for heat treated (cf. as-rolled), *EPMS* for experimental pearlitic or martensitic steel, and *EBS* for experimental bainitic steel. Hardness values quoted in Rockwell C have been converted to Vickers hardness (HV).

Alloy	C	Mn	Si	Cr	Ni	Mo	P	S	Others	HV	Ref.
R200	0.4–0.6	0.7–1.2	0.15–0.58	<0.15	-	-	-	-	-	200–252	[191,192,161]
R220	0.5–0.6	1.00–1.25	0.2–0.6	<0.15	-	-	-	-	-	220–260	[191,192]
R260	0.62–0.80	0.7–1.2	0.15–0.58	<0.15	-	-	-	-	-	260–300	[191,192,161]
R260Mn	0.75	0.90	0.20	-	-	0.90	0.02	0.03	-	260–320	[193,162,192]
R320Cr	0.6–0.8	0.8–1.2	0.5–1.1	0.8–1.2	-	-	-	-	-	320–360	[191,192]
R350HT	0.72–0.80	0.7–1.2	0.15–0.58	<0.15	-	-	-	-	-	360–410	[191,192]
R350LHT	0.72–0.80	0.7–1.2	0.15–0.58	<0.30	-	-	-	-	-	360–410	[191,192]
R370CrHT	0.70–0.82	0.7–1.1	0.4–1.0	0.4–0.7	-	-	-	-	-	376–424	[191,192]
R400HT	0.90–1.05	1.0–1.3	0.2–0.6	<0.30	-	-	-	-	-	410–460	[191,192]
R450HT	0.80	0.89	0.65	0.95	-	-	0.03	0.03	0.04Ti	474–494	[194]
ML330	0.75	1.25	0.80	-	-	-	-	-	0.1 V	330	[191,192]
HP335	0.95	0.9	0.9	-	-	-	-	-	0.1 V	350	[191,192]
BS11	0.53	1.07	0.26	0.01	0.02	0.01	0.021	0.024	-	227	[195]
STD	0.73	0.93	0.28	0.17	-	-	0.01	0.03	0.001B	262	[196]
HH	0.79	0.91	0.66	0.47	-	-	0.02	0.01	-	351	[196]
GOSTr	0.71–0.82	0.75–1.05	0.18–0.4	-	-	-	<0.035	<0.045	<0.07 V	351–406	[197]
GOSTw	0.55–0.65	0.5–0.9	0.22–0.45	<0.25	<0.25	-	<0.04	<0.04	<0.25Cu	255	[197]
EPMS-1	0.77	0.88	0.24	-	-	-	0.008	0.013	-	271–361	[198]
EBS-1	0.52	0.35	0.23	1.71	1.43	0.26	0.01	0.01	<0.01B	361	[10]
EBS-2	0.10	0.59	0.27	1.71	4.09	0.58	0.008	0.02	<0.01B	332	[10]
EBS-3	0.04	0.73	0.21	2.76	1.91	0.26	0.01	0.08	<0.01B	277	[10]
EBS-4	0.18	2.01	1.13	1.94	-	0.48	0.01	0.01	0.003B,0.03Ti	388	[196]
EBS-5	0.12	3.97	0.027	0.02	-	0.47	0.01	0.01	0.003B,0.04Ti	355	[196]
EBS-6	0.02	2.02	0.027	1.96	1.93	0.48	0.01	0.01	0.003B,0.02Ti	271	[196]
B320	0.15–0.25	1.4–1.7	1.0–1.5	0.3–0.7	-	-	-	-	0.1–0.2 V	335–354	[166]
B360	0.25–0.35	1.4–1.7	1.0–1.5	0.3–0.7	-	-	-	-	<0.03 V	370–400	[166]
DOBAIN340	0.76–0.84	0.8–0.9	0.2–0.35	0.4–0.55	-	-	-	-	-	360–400	[191]
DOBAIN380	0.76–0.84	0.8–0.9	0.2–0.35	0.4–0.55	-	-	-	-	-	400–440	[191]
DOBAIN430	0.76–0.84	0.8–0.9	0.2–0.35	0.4–0.55	-	-	-	-	-	450	[191]

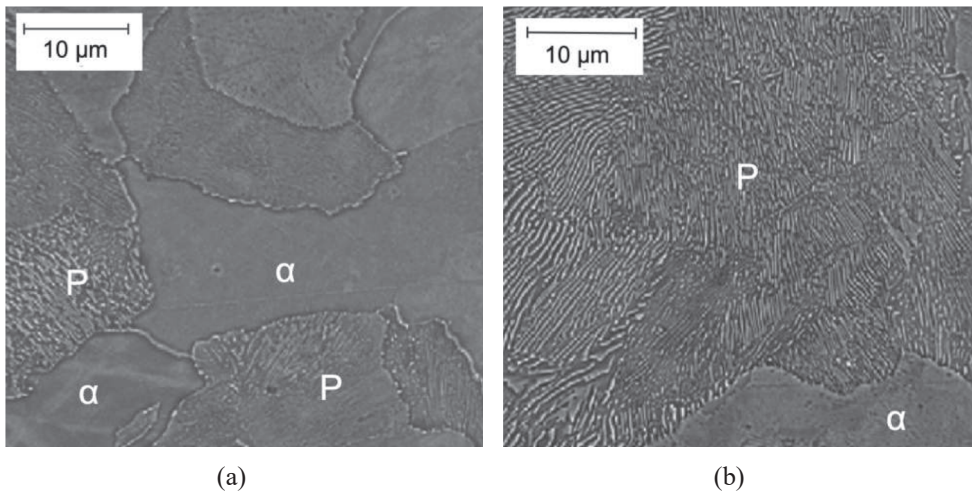


Fig. 18. Optical images of the rail microstructure. (a) R200. (b) R260. Micrographs adapted from Lu et al. [161] with permission of Elsevier.

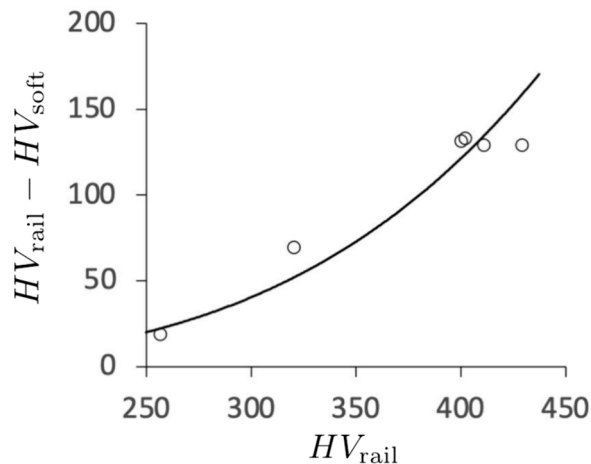


Fig. 19. Maximum change in hardness in the heat-affected zone of a flash butt welded rail, versus the hardness of the rail in the unaffected region. Data compiled from [167,91,168,169].

2.9.2. Other alloys

Additional steels (Table 4) have been approved for use on particular networks. The hypereutectoid HP335 has a composition 0.87–0.97C, 0.75–1.00Si and Mn, 0.09–0.13 V, <0.006 N wt%, tailored to prevent the precipitation of proeutectoid cementite while increasing the fraction of cementite within the pearlite; the silicon also contributes moderately to solution strengthening of the ferrite, with vanadium and nitrogen precipitation additionally hardening the steel though direct observations of this are lacking [180–182]. It has a hardness of about 350 HV [182]. An advantage is that this rail variety does not require heat-treatment following rolling and straightening; tests indicate that HP335 outperforms harder rails in pure sliding test [182] and in dry twin-disc tests (1% slip, 1500 MPa contact pressure), it has been shown to be better than the heat-treated R350HT, Fig. 21 [183]. The difference in strength between the head and foot is just 6% for HP335, whereas it is about 15% for R350HT [184].

Non-pearlitic alternatives include the carbide-free B320 (0.15–0.25C, 1.0–1.5Si wt%), which is a weldable low carbon carbide-free bainitic steel containing Si, Mn, Cr, V, and Mo with similar wear resistance as R260, but much improved RCF resistance; B360 (0.25–0.35C, 1.0–1.5Si wt%) is similar but its greater carbon concentration enhances wear resistance as demonstrated on several track sites across France, Switzerland, and Germany [166]. Carbide-free bainitic rail installed in the Channel Tunnel connecting the U.K. with France has served reliably for more than ten years, after being subjected to > 1 billion gross tonnes of traffic by April 2020, without the need for grinding [185] because of the extraordinary rolling-contact fatigue resistance of these steels. The carbide-free bainitic rail is mostly used on fairly straight tracks; it may not perform as well as the best pearlitic rails on curves, transition curves, or tangents [177,178]. DOBAIN 380 and 430 are high carbon (as-rolled 0.76–0.84C, 0.20–0.35Si wt%) lower-bainitic steels of hardness levels comparable to the pearlitic R400HT; the evidence is that the DOBAIN rails tested on heavy haul tracks revealed no head checks due to their high rolling contact fatigue resistance [54].

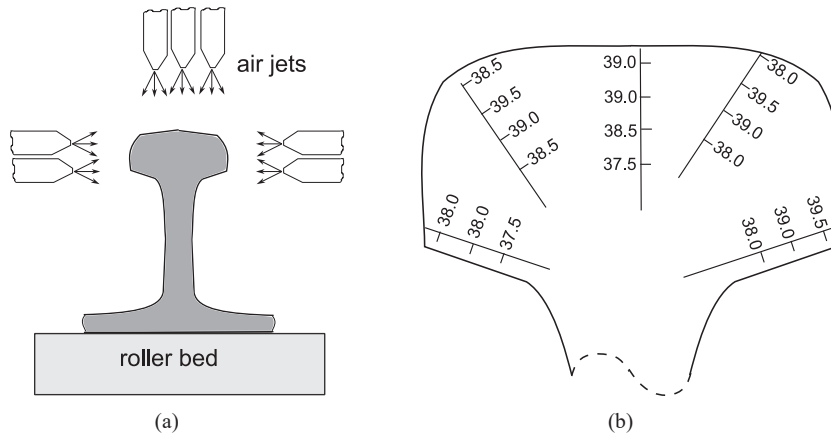


Fig. 20. (a) How the rail-head might be heat treated after austenitisation, with relatively rapid cooling implemented using air jets as the hot rail passes through an enclosed cooling chamber. (b) Distribution of Rockwell C hardness in rail-head. The composition of the rail is Fe-0.75C-0.85Mn-0.6Si-0.084 V wt%, with the commercial designation U75V. A Rockwell C hardness of 39 is equivalent to 376HV. Selected data from Hao et al. [170].

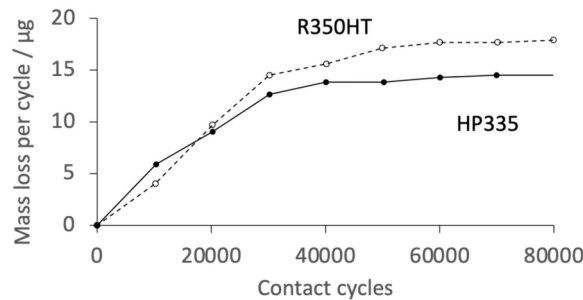


Fig. 21. Wear loss in dry twin-disc tests. Selected data from Wilby et al. [183].

The carbide-free bainite has now been mandated for all new French TGV high-speed movable points⁵ and repair-replacements [186] because of the total suppression of head-checks which are a form of rolling-contact fatigue (p. 79). Apart from initial grinding, no other grinding is necessary during the life of the crossing. The bainitic steel drastically reduced rolling contact fatigue [187]. In contrast, R260 used in these applications requires annual grinding in order to remove the fatigue cracks. The use of the carbide-free bainitic steel saves about 100 k€ per crossing on the life cycle cost, due to life-extension, reduced maintenance and track availability [188]. Crossings like these can be subjected to greater rolling contact fatigue deterioration than the rail itself, due to wheel-rail impacts during the transition [189,190].

In the case of light-weight traffic, such as tramways, it is wear that determines the life of the grooved rails, because of the density of traffic, curved tracks, and the frequent acceleration and deceleration. The wear resistance can be enhanced by precipitation hardening with small concentrations of vanadium. The R290V rail steel has the approximate composition Fe-0.5C-1.1Mn-0.3Si-0.14 V wt%; the low carbon concentration helps weldability. Alternatively, the grooved rails can be hardened by heat treatment, for example, using the Voestalpine method of immersing the whole rail into the cooling bath (p. 18).

3. Rail-wheel contact mechanics

Localised plasticity that extends over many micrometres (Fig. 22)a,c is induced if the cyclic traction⁶ forces operating on rails exceed the elastic limit defined by Hertzian contact stress-fields. The plasticity at large depth is sometimes qualified with the adjective *global* whereas that nearer the contact surface is designated *tribological* because it is associated with wear [201]. These do not of course behave independently but the global component has shear deformation that influences rolling-contact fatigue-crack initiation and propagation. This seems to be important in the modelling of rolling contact, where it is often assumed that the bulk material at depth

⁵ Moveable points allow the train to be continuously guided in one of two directions.

⁶ Traction refers to the tangential force across an interface between two bodies through some sort of friction [199]. The coefficient of traction is the traction force divided by the weight on the tracks [200].

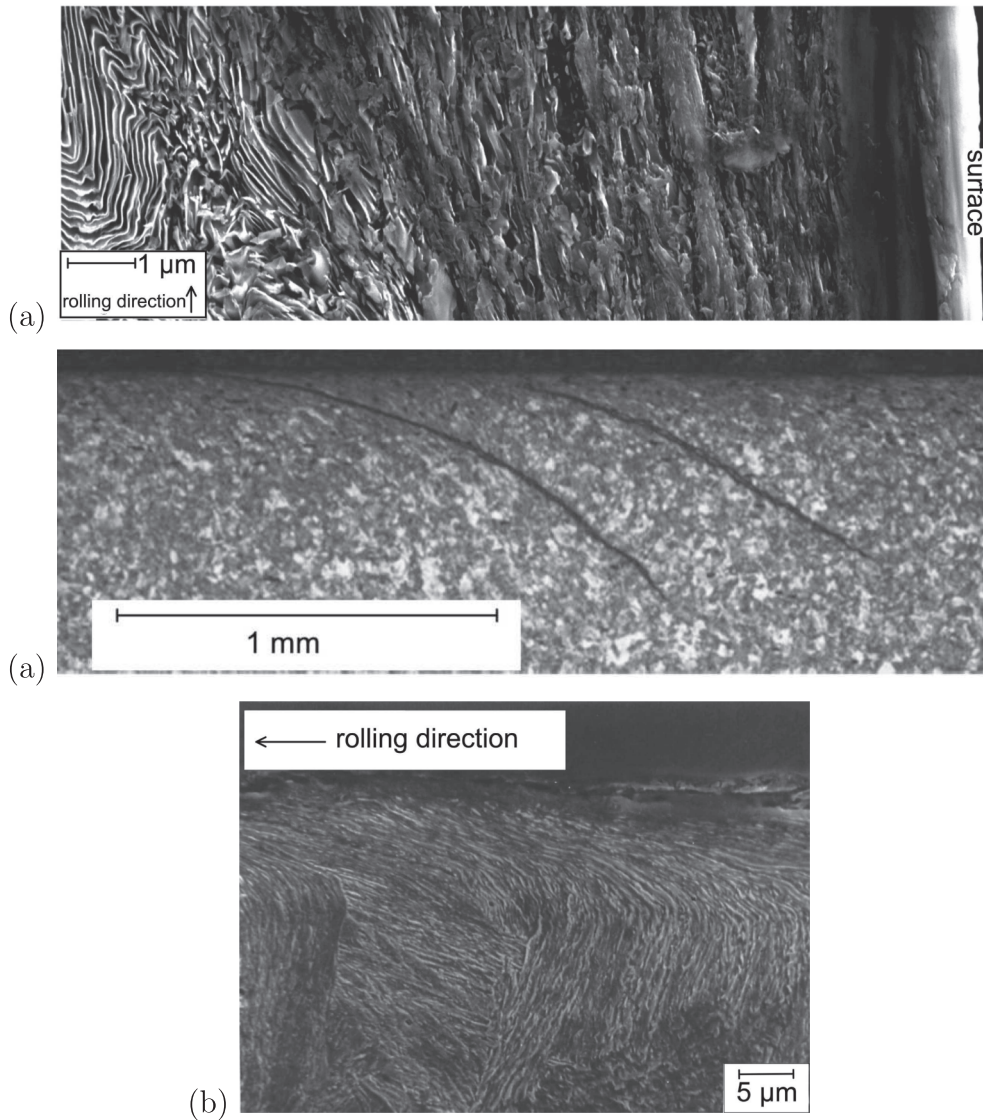


Fig. 22. Plasticity at the contact surface, caused by rolling-sliding. (a) Hypereutectoid pearlitic rail steel. The rolling surface is on the right with the rolling direction vertical. Reproduced and adapted from Chen et al. [203] with permission of Elsevier. (b) Rolling contact fatigue cracks following the directional shear deformation. Image reproduced from Trummer et al. [204] with the permission of Elsevier. (c) Carbide-free bainitic rail steel, showing the shear deformation, image courtesy of L. C. Chang.

below the contact surface responds in an elastic manner; in other words, shear stresses of significance are limited to the locality of the wheel-rail contact.

The amount of plastic deformation is influenced by the normal and tangential stresses within the contact patch, which through constraint influences the properties, including the yield strength, of the asperities [202]. The directional plasticity clearly makes the affected structure anisotropic, which is then replicated by the fatigue cracks that grow along the shear bands, Fig. 22b. Flake formation leading to wear is one consequence, which also influences surface roughness and hence contact behaviour.

In the case of rails, most plastic deformation is accumulated at the surface through a process referred to as *ratcheting* involving the accumulation of small increments of plastic strain over the many cycles as the wheels traverse a specific region of track, Fig. 23. This process is a non-linear function of both the operating/shakedown loads and the number of cycles, but also of the friction coefficient, material hardening response, residual stress state, change in contact conditions, and shear yield strength of the material [205–208,202].⁷ This ratcheting strain behaviour can be described mainly through two variables: the initial shear strain increment, γ_0 ,

⁷ The *shakedown limit* is the maximum contact pressure at which the material does not suffer permanent deformation.

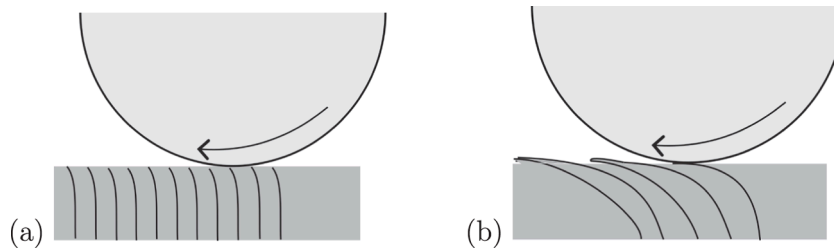


Fig. 23. Schematic representation of ratcheting due to the passage of a wheel on a rail. (a) Early stages. (b) Later stages with considerable accumulation of plastic strain, leading to the laps forming on the surface. Cracks may develop along the deformation lines illustrated and in general spreading underneath depending on vulnerable microstructural features.

and strain accumulation rate, $d\gamma/dN$ [208].⁸ Incremental plastic deformation can be avoided even for applied loads above the elastic limit if there exist protective residual stresses created by the first over-elastic load application, if the material strain hardens, or the geometry of contact changes throughout the deformation [205,207].

Plastic flow can create voids and microscopic cracks that are associated with degradation mechanisms such as the flaking that leads to wear in the tribological layer at the surface, fatigue when those cracks propagate deeper by low cycle fatigue, or rupture caused by brittle fracture or ductile shear through progressive deformation of the surface [209]. The mechanism in each is discussed further in relevant sections.

The normal and tangential traction forces can be modelled in different ways to facilitate analysis [202], for example longitudinal or lateral contact applied either to a line or point on the surface of the rail (Fig. 24). In the case of longitudinal traction the stresses felt are a sequence of tension, shear and compression [205]. The contact mechanism can be mixed rolling and sliding or each on its own. A slip ratio is defined as some function of the distance slid to that rolled [198,206,75,210]. The term *creepage* is often used to describe the ratio of the relative velocity of two rolling bodies, normalised by the rolling velocity; it has nothing to do with creep that is thermally activated deformation at stresses well below the yield strength.

The effective friction coefficient⁹ μ_f is affected by the creepage, normal stresses, speed, surface roughness, lubrication type, and rate of supply according to [211] – rails are not generally lubricated unless weather affected or with the application of “top-of-rail” products [212] or debris at the contact surface [213]. Three stages can be identified in the context of lubrication, when μ_f is plotted against creepage and number of revolutions [197,205,206]:

- at first, the surface of the rail is coated uniformly by a protective film of lubricant ($\mu_f \simeq 0.1$),
- an acceleration stage in which the layer degenerates and μ_f increases,
- the steady state condition in which μ_f can reach values of up to 0.6.

In this last steady state condition, μ_f can become independent of creepage in the 2–100% range according to [197] or above 1% according to [50]. It is recognised that unless there is a standardised test and control system for the friction coefficient, results using different equipment will not be identical. Such steady state behaviour will not apply to conditions of full lubrication in which case the friction coefficient can decrease to values of 0.1–0.2 if slippage is below 30% [197]. Instead, μ_f is dependent on slippage if it is between 1–2% and it will maintain a value close to 0.2 [214]. Such values of 0.2–0.25 can be achieved with slippage ratios of up to 10% although they can vary as the number of cycles accumulates, by approximately 10% due to the degeneration of protective films [197,196]. There are circumstances in which dry rolling whence cracks form, followed intermittently by friction modifiers, can exacerbate wear because the modifier enters the cracks under pressure [215]. Fluid penetration into cracks can, by modifying friction at the crack-faces, accelerate the shear mode of growth [216].

As mentioned earlier, friction coefficients below 0.25¹⁰ locate the maximum orthogonal shear stress below the surface whereas higher coefficients shift its position to the surface. This is why wet service that lowers friction has been recognised to reduce wear but enhance RCF [219,220,50]. The depth of such subsurface stresses can be of around 0.2mm for twin-disc tests or 2mm for actual rails due to the fact that the contact patch is elliptical for rail/wheel contact, but just a strip in the case of twin disc tests (see Section 6 and

⁸ The following equations are for a pearlitic rail with a hardness of about 270HV [208], to illustrate the ratcheting:

$$\gamma_0 = 8.3275 \times 10^{-8} \exp\{0.024867\mu_f p_0\}$$

$$\text{and } \frac{d\gamma}{dN} = \gamma_0 b N^{b-1} = 1.1023 - 0.00127644\mu_f p_0,$$

where γ_0 is the initial shear strain increment, N is the number of cycles, μ_f , the friction coefficient, $\mu_f p_0$ is the maximum shear stress, p_0 is the contact pressure, and $b \approx 0.5$ is a fitting parameter. The numerical coefficients are derived by Su et al. [208] using experimental data.

⁹ Defined as the usable force for traction divided by the weight on the running gear or alternatively, the shear force over the normal load [207,206]. It sometimes is referred to as a traction coefficient but has the same meaning.

¹⁰ This threshold does not have a fundamental basis - indeed, others set it at $\mu=0.3$ [75] 0.36 [217] or 0.4 [218].

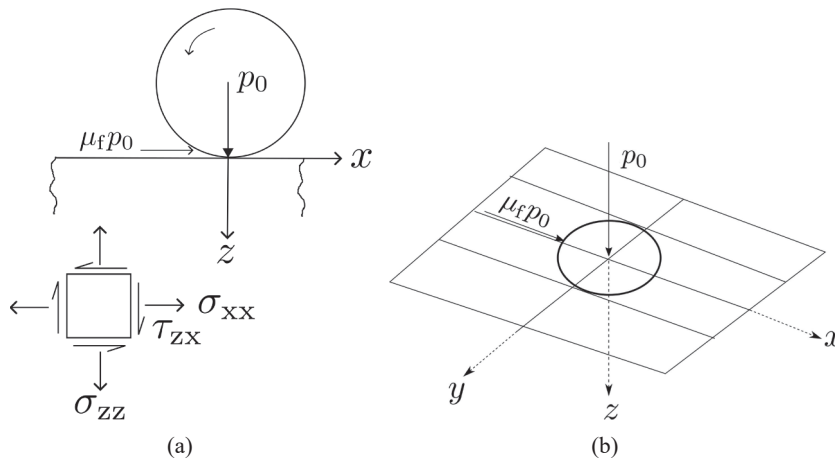


Fig. 24. Schematic of (a) line and (b) point contact. p_0 corresponds to the applied pressure, μ_f is the friction coefficient and σ and τ correspond to normal and shear stresses along the described directions. Redrawn based on [205].

Fig. 25) [221].

At first, dry partial-slip generates only subsurface non-accumulative strain, until the shakedown limit is reached and the friction coefficient rises above ≈ 0.25 , which occurs after just ≈ 100 –200 cycles for $p_0=1200$ MPa or 200–500 cycles for $p_0=1500$ MPa after which, deformation occurs at the surface [206]. Instead, if the number of dry cycles is low or lubrication is introduced, the friction coefficient will remain below 0.25, leading to hardening and eventual damage occurring below the surface. Since the friction coefficient will normally have lower values under conditions of full slip than in dry partial slip, the latter type of contact can cause more surface damage when the traction reaches a steady state [205]. If the cycles and contact pressure are maintained constant and only the circumferential/rolling speed is increased, the effective friction coefficient, without lubrication, has been shown to slightly decrease and therefore, the driven roller (rail) in twin disc tests shows lower wear due to higher deformation speeds at the subsurface [222,223]. With respect to its relation to contact stress, several authors have observed a decrease in the friction/traction/adhesion coefficient with increasing contact force, but no relation was found between this coefficient and crack size or fatigue life [223,50].

The coefficient can be altered by the presence of non-intentional third-body layers that either cause a loss of adhesion between the rail and the wheel such as oil, water, dew, or frost, and fallen leaves, whilst other contaminants such as sand enhance traction and can remove the build-up of leaves but damage the surface by indentation. Fig. 26a shows how a variety of contaminants can affect the traction coefficient for a range of slip values, confirming that leaves, either dry or wet, are a good lubricant as they form layers of 14–58 HV0.001, which can take from 200–600 cycles to be removed [224,225]. Safe train-braking or acceleration can be compromised by the reduced adhesion due to leaf cover [e.g., 226]. The subject has been reviewed [1] but generic conclusions are difficult because of the variety of leaves and their moisture content, whether that is due to dew or rain. Leaves from maple trees reduce traction less than those from the oil-rich ginkgo trees [227].

The influence of water temperature or surface roughness in twin disc wheel-rail contact tests are illustrated in Fig. 26b,c, confirming that an increase in both of these parameters increases the adhesion [228]. The orientation of the rail roughness also influenced the adhesion such that roughness perpendicular to the rolling direction decreased adhesion to its minimum, whilst parallel roughness increased it to its greatest value; nevertheless, it is not clear why these results entirely contradict their earlier simulations on surface roughness orientation [229].

In the spectrum of loading contact, from the perfectly elastic one where the maximum stress does not exceed the yield stress to incremental collapse or ratcheting where every steady state cycle accumulates unidirectional plastic strain, there exists a deformation mode known as *shakedown* that can be either elastic or plastic [207]. Elastic shakedown occurs when there is a load that exceeds the yield stress thus creating plastic deformation and making subsequent cycles to lie once again in the elastic region. The maximum contact pressure which can be carried purely elastically in the steady state is known as the shakedown limit, and it can be approximated as four times the shear yield stress in the case of frictionless rolling/sliding [230,207]. Instead, plastic shakedown refers to the steady state cyclic loading that leads to no net accumulation of uni-directional strain. The maximum load possible in the plastic shakedown region is referred to as the ratcheting threshold, as above it, ratcheting will start to occur (Fig. 27).

The boundaries of each of these loading behaviours with respect to the traction coefficient can be represented in a shakedown map

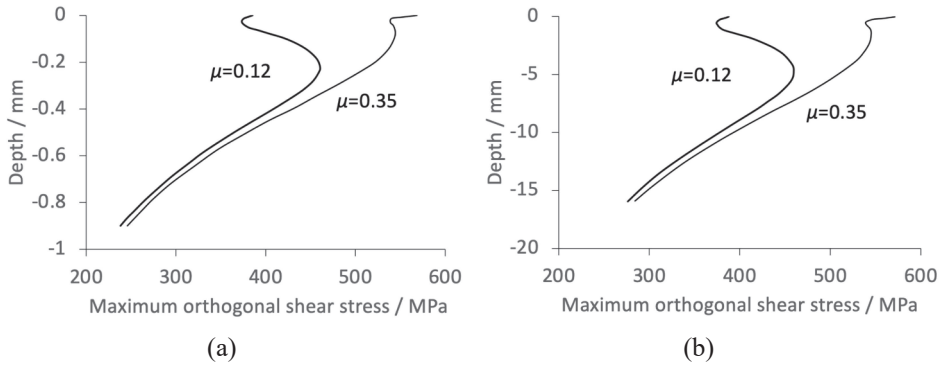


Fig. 25. Maximum orthogonal shear stress as a function of depth below the contact surface. (a) Twin disc line-contact over a half width of 0.31 mm. (b) For wheel/rail line contact over a half width of 6.6mm. Note the similarity in curve shape but the huge difference in depth. Adapted using selected data from Fletcher [219].

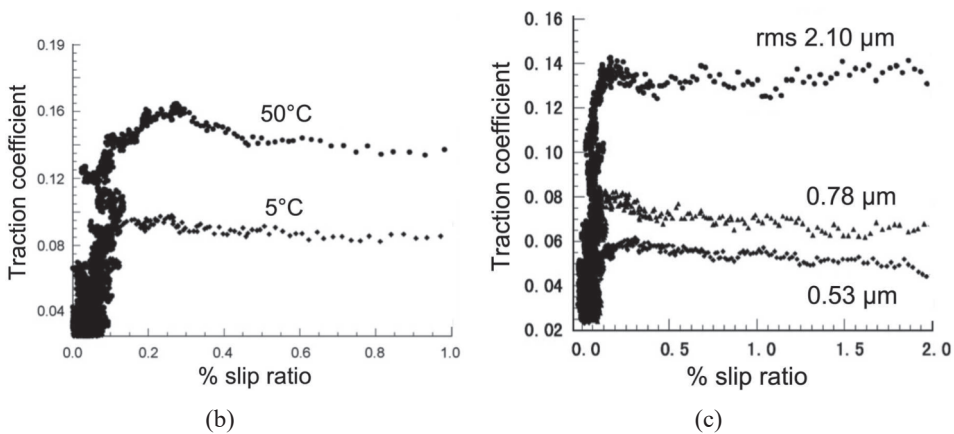
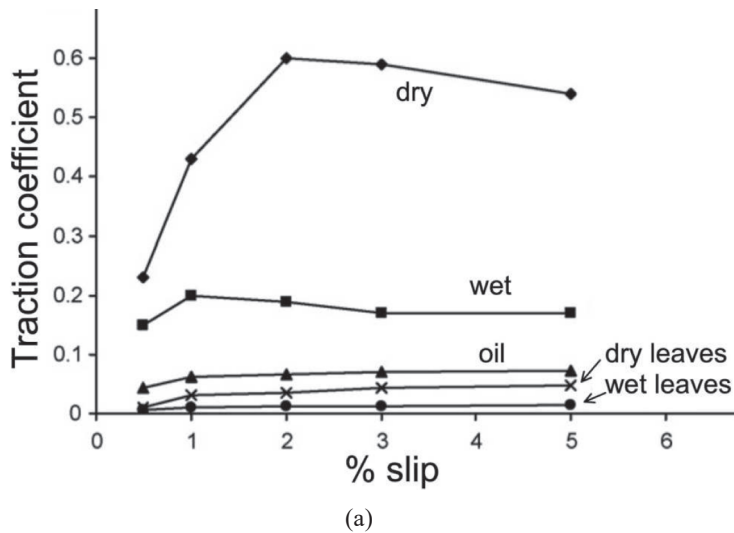


Fig. 26. Relationship between the traction coefficient and slip ratio, while varying other parameters. (a) slip, showing how the coefficient increases with slip, but is reduced by the presence of water, oil, or entrapped leaves. (b) As a function of the water temperature with a rolling speed of 100 km h^{-1} . (c) As a function of surface roughness expressed as the root mean square (rms) value, with a rolling speed of 100 km h^{-1} . Reproduced with the permission from Elsevier [224,228].

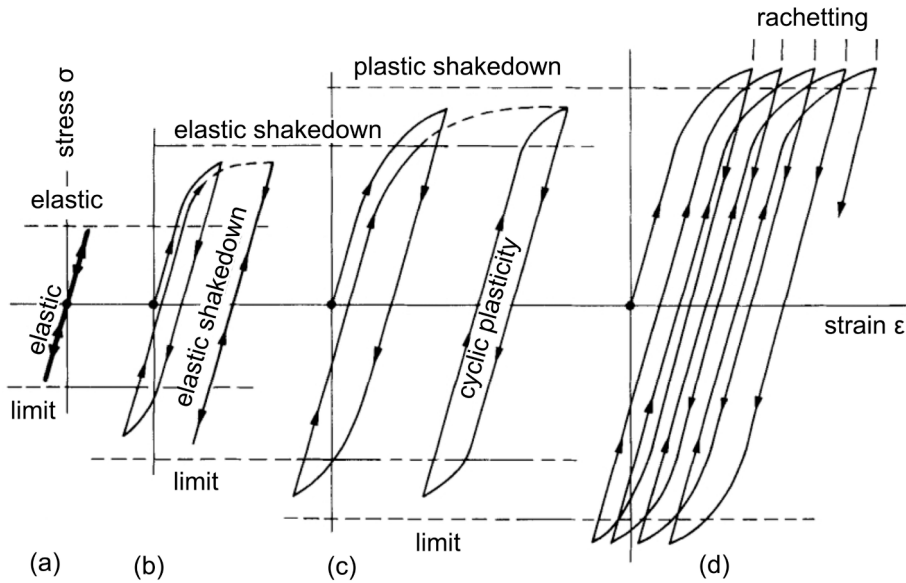


Fig. 27. Stress strain curves for the four different types of cyclic loading. (a) Perfectly elastic. (b) Elastic shakedown. (c) Cyclic plasticity, plastic shakedown. (d) Incremental collapse, ratcheting. Reproduced with the permission of SAGE [231].

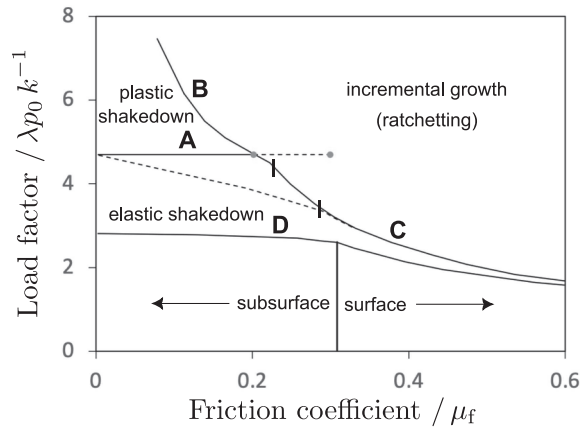


Fig. 28. General shakedown map obtained for a steady state circular region loaded with different normal and tangential loads, where k is the shear yield strength and λ accounts for the shape of the contact area. (A) Upper bound to elastic shakedown limit against alternating plasticity. (B) Upper bound to plastic shakedown limit against incremental growth. (C) Upper bound to elastic shakedown limit against incremental growth of surface strain. (D) Elastic limit. The dashed line represents the lower bound to elastic limit. Reproduced with the permission of Elsevier from [234] adapted by [235].

(Fig. 28), which plots the material response and position of greatest fatigue damage for a specific load, friction, material ductility, and contact geometry. The defining boundaries are variable since the real contact conditions may include friction and surface asperities, which can create peak pressures up to eight times greater than the calculated by a smooth Hertzian contact and whose dimensions dictate the depth of the deformed layers, allowing loads well below the elastic shakedown limit to induce significant plastic flow at the subsurface of rails [230,232]. An example of this is the *Shinkansen* (Fig. 29) where plastically deformed sub-surface layers of 15–20 μm have been observed on a rail whose shakedown limit is 2077 MPa but operates at loads imposing only 900–1180 MPa and a traction coefficient of 0.01 [233].

The shakedown limits for line contact and other scenarios have been estimated by Johnson and co-workers [207,205]. The relevant notation is illustrated in Fig. 24, the stress components are given by:¹¹

¹¹ $c < |x| < a$, where a is the semi-contact width.

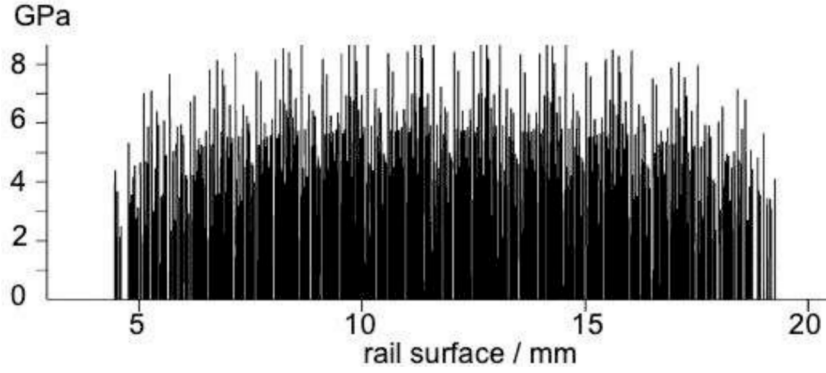


Fig. 29. Pressure distribution map of a wheel pressed against a Shinkansen rail where the idealised smooth Hertzian solution would be of 1 GPa. Reproduced with the permission of Elsevier from [230].

$$\begin{aligned}\sigma_{xx} &= -p_0 \left(1 - \frac{x^2}{a^2}\right)^{1/2} - 2\mu_t p_0 \frac{x}{a} & \sigma_{zz} &= -p_0 \left(1 - \frac{x^2}{a^2}\right)^{1/2} \\ \sigma_{yy} &= \nu(\sigma_{xx} + \sigma_{zz}) & \tau_{xz} &= -\mu_t p_0 \left(1 - \frac{x^2}{a^2}\right)^{1/2} \\ \tau_{xy} &= \tau_{yz} = 0 & \tau &= \left[\frac{1}{4}(\sigma_{xx} - \sigma_{zz})^2 + \tau_{xz}^2\right]^{1/2}\end{aligned}$$

where τ is the principal shear stress inside the contact area, in the plane of deformation. And the shakedown limit is given by:

$$\frac{p_0^s}{k_e} = \frac{1}{\mu_f} \quad (6)$$

where p_0^s is the peak Hertzian pressure at shakedown and k_e the stress corresponding to the radius of the Tresca yield locus circle.

In the case of a longitudinal point contact (of length a) under full slip the tangential traction q is given by [207]

$$q = \frac{3\mu_t P}{2\pi a^3} (a^2 - x^2)^{1/2} \quad (7)$$

where P is the contact load per unit length.

The shakedown limit in such a scenario, calculated by the von Mises criterion, is significantly smaller than in line contact.

A scenario that considers instead longitudinal line contact under partial slip is useful as it replicates the most standard work condition of rails (dry and straight track or soft curves). This scenario, according to Fletcher, is a reasonable assumption since the major axis of the real contact elliptical patch where the maximum stresses are located, is similar to a line contact (Fig. 25) [219]. The traction in this case is given by

$$q = \mu_t P \left(1 - \frac{c^2}{a^2}\right) \quad (8)$$

For point contact, but keeping the longitudinal traction and partial slip, the equation is

$$q = \mu_t P \left(1 - \frac{c^3}{a^3}\right) \quad (9)$$

Lateral line contact under full slip can be represented through the following equations [205]:

$$\begin{aligned}\sigma_{xx} &= -p_0 \left(1 - \frac{x^2}{a^2}\right)^{1/2} & \sigma_{zz} &= -p_0 \left(1 - \frac{x^2}{a^2}\right)^{1/2} \\ \sigma_{yy} &= \nu(\sigma_{xx} + \sigma_{zz}) & \tau_{yz} &= -\mu_t p_0 \left(1 - \frac{x^2}{a^2}\right)^{1/2} \\ \tau_{xy} &= -\mu_t p_0 \frac{x}{a} & \text{with} & \quad \tau_{xz} = 0\end{aligned} \quad (10)$$

For the lateral line full slip contact the shakedown is the same as that given by Eq. 1g. However, for the case of lateral point contact and full slip, shakedown is [205]:

$$\frac{p_0^s}{k_c} = \left[\frac{7}{16}\alpha^2 + \left(\frac{1+\beta^2}{2} \right)^2 \mu_f^2 \right]^{-1/2} \quad (11)$$

where $\alpha=(1-2\nu)/3$ and $\beta=\pi(1-\nu/2)/4$ and ν is Poisson's ratio with a value of 0.5 for incompressible materials or 0.3 for compressible ones.

During longitudinal contact, the surface accumulates shear strain along the length of the rail. In contrast, lateral traction will displace material towards the edges of the rail head. Under normal running conditions, lateral motion tends to be random so no change of geometry is perceived, so the equations of lateral partial slip for line or point contact are not presented here [205].

An alternative to models for the estimation of contact stresses and the size and shape of contact patches during wheel-rail combinations is an experimental method that utilises the coefficient of reflection of ultrasonic waves [236,237]. It can be applied to the real contact areas as a function of pressure [238]. The technique is calibrated against a known contact pressure distribution using a finite element model for given values of surface roughness, wave frequency, and type of material [239,240]. The points of microscopic contact and those of incomplete contact are averaged to generate maps of the size of the contact area with an error of 0.1–0.4 mm. The method agrees with Hertzian theory, is easier to run and calibrate than for example, photoelastic frozen stress techniques [241], and offers the option of performing dynamic measurements in order to investigate other phenomena such as corrugation or loss of adhesion.¹²

A review on the experimental determination of contact geometry of rough surfaces by Woo and Thomas concluded that: “the real area of contact increases with the load and this increase is due mainly to an increase in the number of micro-contacts, their mean size remaining approximately constant; the separation of the contacting surfaces is approximately inversely proportional to the logarithm of the load; the distribution of contact spot sizes is approximately log normal”. However, it appears that the density and average size of micro-contacts can vary over several orders of magnitude for different surfaces at the same load. Contrary to established belief, the real area of contact does not vary linearly with the load but increases as its 0.8th power [242], although the mechanism for this dependence was not obvious. In fact, it is now considered that a linear relationship between the contact area and load is justified for random, rough-surfaces [243,244].

When rough surfaces touch, fractal theory indicates that the contact area must depend on the resolution with which it is measured [245]. Whether this matters when considering engineering scales is not established.

4. Wear

Wear can be defined as the displacement or removal of material as a result of tribological processes, which can be measured either as a wear rate, i.e., material removed over the sliding distance or cycle, for example $1 \mu\text{g cycle}^{-1}$ for R220 [50,75,219], or through the dimensionless Archard wear coefficient k [246],

$$k = \frac{V_w H}{F d_s} \quad (12)$$

where V_w is the wear volume in m^3 , H is the hardness in Nm^{-2} , F is the normal force in Newtons, and d_s is the sliding distance in metres [247,248]. The coefficient k should be equal to unity if every asperity contact at the rubbing surfaces contributes to the worn volume, but in fact is much smaller because they apparently must be rubbed many times before damage, possibly because many are elastically deflected during the rubbing [246]. The coefficient depends on the location on the rail profile; it typically is, 10^{-9} to 7×10^{-8} on the rail head and can reach 2×10^{-7} on rail gauge corners [249].

The variation of mechanical parameters such as load, rolling/sliding speed, temperature, lubrication, and number of cycles during wear testing or actual tribological scenarios produces a variety of material responses, mostly irrespective of the microstructure. The regimes have been categorised based on the intensity of the wear volume, wear rate, and wear particles [250]. There are three main qualitative categories according to Bolton and Clayton: mild (type I), severe (type II), and catastrophic (type III) [195], although some others authors claim the existence of a heavy mode in between the severe and catastrophic modes [251] and others have simulated a severe catastrophic mode where wear rates are still in the severe regime [252].

Each of these modes can be associated with a specific wear mechanism such as plasticity-dominated, delamination, oxidation, melting, and seizure [253]. Maps of these modes and mechanisms during unidirectional dry-wear have been constructed by Lim, Ashby, and Brunton as a function of normalised velocity or sliding velocity over seven orders of magnitude against normalised pressure over six orders of magnitude, based on many experimental data from various types of steels, Fig. 30 [254,255]. A less comprehensive map for lubricated wear was compiled by Akagaki et al. [256]. However, these maps should be regarded only as a first approximation due to the inconsistencies in surface temperature estimation using either experiments or heat-flow calculations [254,250,257]. For example, Fischer et al. investigated how surface flash temperatures change significantly from the ideal smooth contact if roughness is considered due to friction and pressure intensification at individual asperities [258].

Another way of mapping the wear modes without involving surface temperatures is to plot the wear rate expressed as weight loss per metre of rolling per unit of Hertzian contact area [$\text{mg m}^{-1} \text{mm}^{-2}$] against $T\gamma/A$ where T is the tractive force (normal force times the

¹² Corrugation occurs when the rail profile does not strictly conform to that of the wheel, especially on curves. It can be mitigated by using rails that are more resistant to plastic deformation, and regular maintenance of rail and wheel profiles.

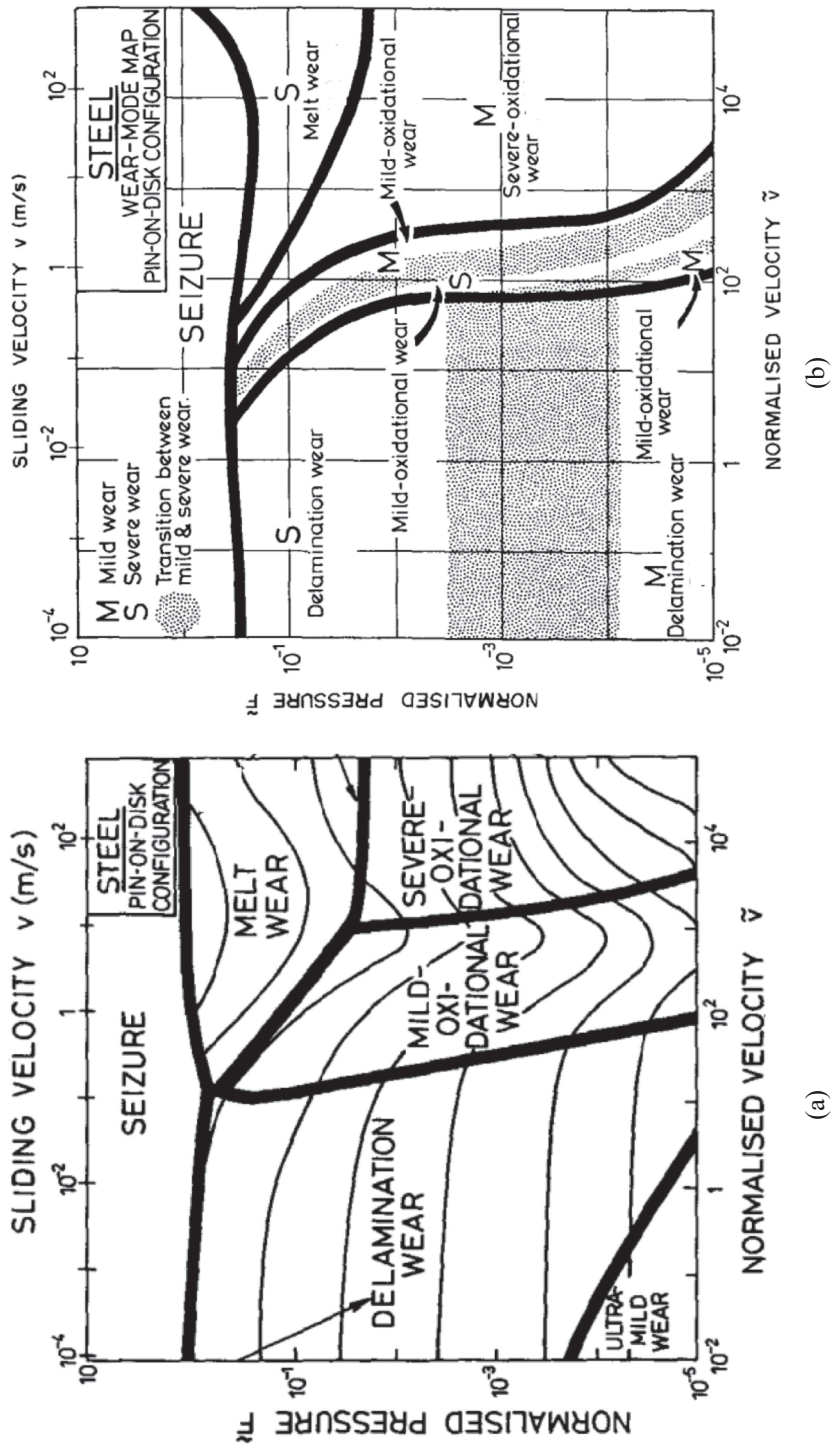


Fig. 30. Empirical maps by Lim, Ashby, and Brunton plotted for sliding velocity against pressure obtained using an unlubricated pin on disc setup for: (a) wear mode with constant normalised wear-rate contours. Each labelled field identifies the dominant wear mechanism. (b) Wear mechanisms, where the grey regions represent transitions between modes and the solid lines the boundaries between mechanisms. Reproduced with the permission of Elsevier [254,255].

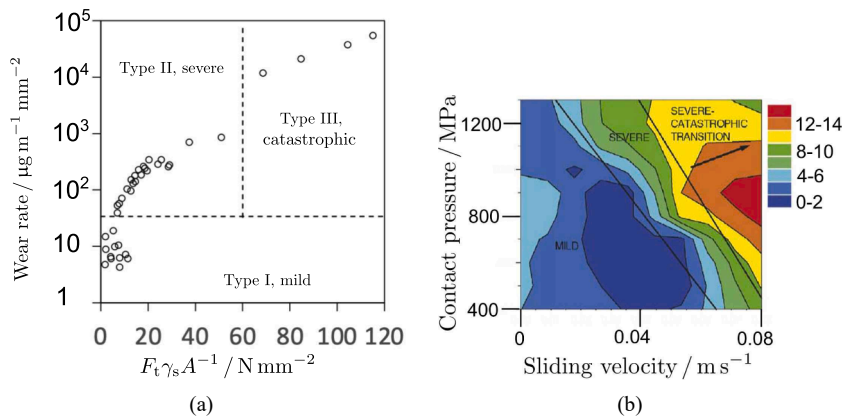


Fig. 31. (a) Typical map of wear modes using the $F_t\gamma_s/A$ method of BS11 grade in twin disc testing and (b) wear coefficient map by Lewis and Olofsson for BS11 grade. Reproduced with the permission of Elsevier [252].

friction coefficient), γ the slide/roll ratio or slip, and A the Hertzian contact area [195]. Although these maps allow transitions to be easily identified and comparison between different materials; plotting the wear coefficient against contact pressure and sliding speed allows a more precise understanding of the contribution of these last two variables, Fig. 31 [252].

Wear modes occur sequentially as a result of increasing contact pressure, slide/roll ratio and greater wear volumes [195]. **Type I** wear occurs at low slide-roll ratios (1 m s^{-1}) or contact forces (20 N) and refers to the process of material removal by the progressive growth and mechanical breakdown of an oxide layer. For example, Wang et al. observed smooth surfaces with little ploughing, signs of minimal plastic deformation, and the presence of thin flakes generated from the shear of asperities and oxidative particles removed from the thin oxide layer or simply metallic particles that were removed and became oxidised [250]. This mode is often used to model wear at the rail head or wheel thread [6,252]. The wear rates (see Table 5) are classified as mild and correspond to $< 10^{-6} \text{ mm rev}^{-1}$ if derived using a twin disc setup (Amsler type) [197] or $< 1 - 2 \times 10^{-8} \text{ mm}^3 \text{ N}^{-1} \text{ mm}^{-1}$ for pin-on-ring rigs and bearing steels [250] although most authors agree that the dividing line between wear modes is not strict and depends mostly on the morphology of the worn surfaces and the number and size of wear particles. In another context, 52100 bearing steel, the boundary has been explained in terms of frictional heating temperatures with the boundary occurring at about 200°C [257]. Others attribute this boundary to the change from partial slip to full slip contact [259]. Some of the most important degradation mechanisms associated with this mode are mild to severe oxidation or delamination.

In **type II** wear there is extensive plastic deformation sometimes ripples on the surfaces and metallic debris particles which can adhere to the deepened wear grooves and lead to deformation and fracture without necessarily having fatigue cracks. Such a mode of wear is common at the wheel flange/rail gauge-corner contact [252]. For this mechanism, the wear rate follows a linear relationship against $F_t\gamma_s/A$ where F_t is the tractive force (normal force $\times \mu_t$), γ_s is the slip (% difference in surface speeds between the rail and wheel) and A is the contact area. It is the wear mode for which small-scale twin disc test results have been found to better replicate full-scale tests, presumably due to a more accurate estimation of friction values [6,260]. The wear rates of type II are normally severe ranging from 10^{-6} to $10^{-4} \text{ mm rev}^{-1}$ in twin disc setups [197]. It is possible within this mode to observe severe delamination, mild to severe oxidation, or local melting. Delamination refers to the increased plastic shear strain below the contact surface, that nucleates cracks, which then propagate parallel to the surface and eventually grow to the surface resulting in wear flakes [209] (Section 6). Rosenfield [261] suggests that the energy required to create a new surface by wear is much higher than that for tensile cracking. Contact temperatures can range from $200\text{--}300^\circ\text{C}$, resulting in a reduction in the strength of the locally heated region [259].

Type III involves a break-in period or shakedown that leads to the production of large debris particles (spalls) that cause gouging abrasive wear at the surfaces in contact; such a mode is used to simulate unlubricated curved track with gauge face wear, and is associated with catastrophic wear rates in excess of $10^{-4} \text{ mm rev}^{-1}$ [6,262,197]. The number of running-in cycles during this regime is inversely proportional to the slippage but directly proportional to the thickness of the contamination film on the rail [197]. According to Welsh, the upper limit of this mode represents the minimum load at which frictional heating is maintained at a high enough level to cause hardening,¹³ [263,264]. In Type III wear, it is possible that in some circumstances, the surface can be induced into localised melting, with surface temperatures ranging from $1340\text{--}1580^\circ\text{C}$ [265,266]. The energy required to create a new surface during severe grooving deformation is negligible compared to the deformation energy, at least during single-pass abrasion tests [267].

Micrographs of the surface and profile of rails under the different wear regimes are presented in Fig. 32. It is worth noting that the

¹³ The hardening presumably occurs because the steel is locally austenitised and then cooled rapidly by the underlying material, resulting in transformation products such as martensite.

Table 5

Range of wear rates on Russian, American, British and German railways for different contact conditions. Wear rates are given as the change in roller radius (in units of mm) per revolution $W = \Delta r/n$ [197].

Wear rates	Longitudinal contact	Lateral contact	Wheel skidding
Lubricated	10^{-8} to 10^{-7}	10^{-7} to 10^{-6}	$\geq 10^{-4}$
Not lubricated	10^{-7} to 10^{-6}	10^{-6} to 10^{-5}	

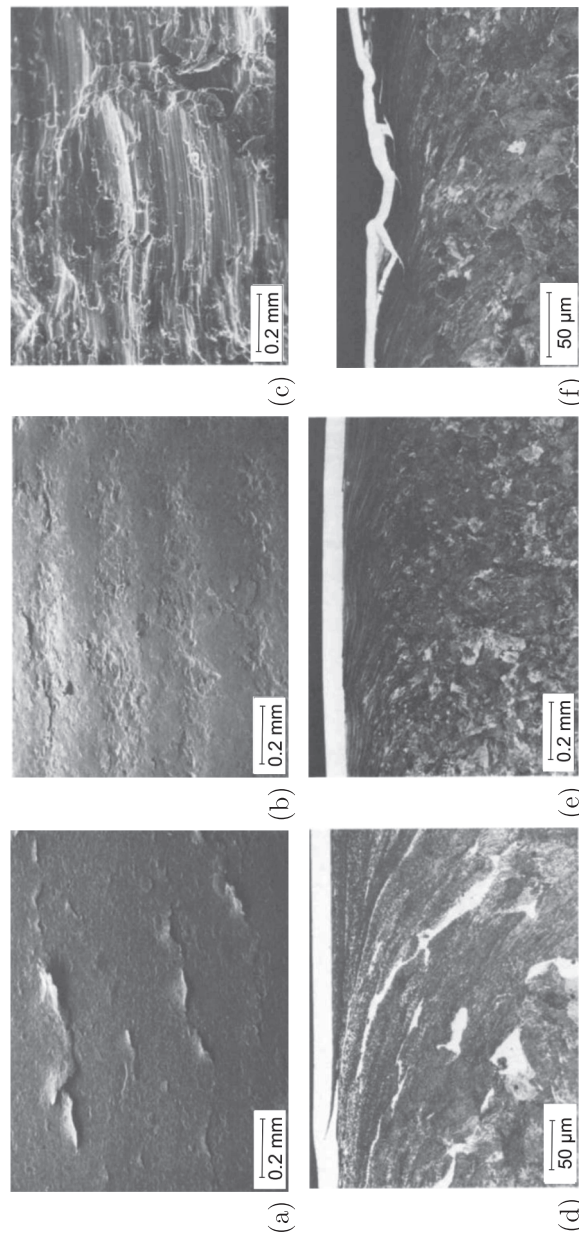


Fig. 32. Wear modes at the surface of a rail-steel Fe-0.53C-1.07Mn-0.26Si wt%. (a) Type I, 1% creepage, $P = 1050 \text{ MPa} \downarrow$, where the arrow indicates the direction of the creepage force. (b) Type II, 7% creepage, $1050 \text{ MPa} \downarrow$. (c) Type III, 34% creepage, $1150 \text{ MPa} \rightarrow$. (d-e) represent longitudinal sections. (d) Type I, 2% creepage, $1075 \text{ MPa} \rightarrow$. (e) Type II, 10% creepage, $1250 \text{ MPa} \rightarrow$. (f) Type III, 30% creepage, $1250 \text{ MPa} \rightarrow$. Creepage is defined as $2(1.104D_2 - D_1)/(D_1 + 1.104D_2)$, where D_1 and D_2 are the top and bottom rollers diameters. The 1.104 is the ratio of the rotation speed of the bottom shaft to the top shaft. Reproduced with the permission of Elsevier [195].

stresses and work-hardening behaviour during twin disc wear tests may not be representative of actual rail-wheel wear [222].

Due to the myriad of metallurgical and engineering parameters that are involved in the contact between wheels and rails such as wheel load, track curvature¹⁴, track support system, track elevation, train suspension system, slip forces, friction, lubrication, operating temperature, humidity¹⁵, surface contamination, and material properties amongst other, a general empirical model can be very complicated to produce [6]. Instead, Clayton advocates experiments that relate the wear rate to metallurgical factors, and investigation of the strain accumulation per cycle during wear to outline the boundaries of the different regimes. However, it is worth considering that most of those parameters, especially, surface roughness, hardness, and other microstructural parameters like volume fractions of phases, strain hardening, and the scale of microstructure, will change throughout the life of the component making wear a dynamic process that cannot be modelled based only on the initial values. The information can nevertheless be useful as the basis for alloy design.

One option to simulate and predict wear in order to develop an optimal maintenance schedule that encompasses lubrication, grinding, and wheel turning, was carried out by Jin et al. who combined twin disc experiments using the contact geometry and loads used in service, three dimensional elasto-plastic finite element modelling to compute the contact stresses and locations, and computation of a modified version of the Archard coefficient¹⁶ in an iterative process that recalculates the loads and mean slip ratio as the profiles wear down, Fig. 33 [249]. The only parameters that required recalibration in the twin disc tests were the longitudinal slip due to sizing effects and work hardening, which is 1.5–2 times greater in the laboratory than in real rail tracks.

Another dynamic ratcheting model for studying wear rate was developed by Kapoor and Franklin by dividing the material in layers across the depth and allowing each layer to accumulate plastic shear until the ductility is exhausted and is removed as wear debris [268]. Later improvements allowed also the variation of properties through the plane represented by each layer in order to examine the role of the microstructure in ratcheting wear.

4.1. Hardness

It is a common belief that for a given microstructure, an increase in hardness reduces the wear rate. However, parameters such as the type of contact, slippage, load, and difference between rail, wheel, and total wear rates, indicate that there is no singular dependence of wear rate on hardness [269,197,270]. Using a well-known Amsler-type machine, Markov proved that during *longitudinal contact*, the slippages of the top and bottom rollers are different so their wear rates are not identical even at constant hardness; the total wear rate decreased as the hardness of the wheel increased. However, when the friction coefficient was kept constant, as during steady state contact, the wear rate of a roller was inversely proportional to its hardness, but proportional to the hardness of the counter-roller. During *lateral contact*, the slippages of top and bottom rollers are the same, so at equal hardness (370 HV), their wear rates were the same.

Therefore, increasing the hardness of one roller decreases its wear rate but at the same time increases that of the counter-roller; increasing the hardness of both does reduce the total wear rate. Experiments by Jin et al. confirmed this during the *early* stages of wear, but concluded that increased rail hardness can at the later stages reduce the wear on the wheel since the rail-gauge corner is maintained longer [249]. Others support this but also point out that size of the contact patch is minimally changed if the hardness is increased (Fig. 34a) [271,272], although variables such as the hardening response, friction coefficient, and residual stresses can also influence the patch size. During *skidding* or pure sliding, increasing the hardness of one or both rollers causes reduction of the rail and total wear rates. Also, the wear rate of the driving roller is inversely related to its own hardness and independent of the hardness of the driven roller [197].

Rail tracks are in general harder than the wheels because the latter usually have a hypoeutectoid chemical composition. Therefore, Fig. 34a would indicate that wheels wear at a greater rate than rails. However, this general conclusion fails if the microstructure is engineered so that the rail becomes relatively innocuous in its contact with the wheel. In particular, carbide-free bainitic rails fare well in this respect (Fig. 34b). In independent tests, it has been shown that the carbide-free bainitic steel has a wear rate ten times smaller than a head-hardened pearlitic rail-steel [273]. The origin of the good properties of carbide-free bainite in the context of rail steels lies in the absence of brittle cementite, the ability of the microstructure to undergo large surface-deformations without the creation of excessive debris and the mechanically induced transformation of retained austenite into hard martensite [274],[p.436, 275].

Two regimes of hardness dependence are found as a function of slippage. Below 5% (mild wear), the total wear rate is independent of the hardness due to the larger fatigue component that redistributes plastic deformation at the surface of the rollers. When slippage is 5–100% (severe wear) increasing the hardness of any of the rollers or both will decrease the total abrasive wear at the surfaces. These observations lead the author to conclude that when working below 5% slippage, increasing the hardness of the wheel or rail has no effect on wear, but at larger values of slippage, a higher hardness of rails is much encouraged [197]. Although the hardness of rollers was varied, the compositions of the wheel (GOSTw, Table 4) and rail (GOSTr) were different and the microstructure was not indicated,

¹⁴ As angle of attack, used in twin disc tests to simulate curved tracks, increases or thrust load (lateral) is induced, the wear rate of the wheel flange and rail gauge corner increase, whilst those of the wheel thread and rail head slightly decrease due to an larger slippage on the contact surface of the rail gauge corner [249].

¹⁵ For example, humidity is responsible for varying the average wear rate from $1.26 \times 10^{-7} \text{ mm rev}^{-1}$ during winter down to 0.73×10^{-7} in summer [197]. Water lubrication can reduce the wear rate at the wheel flange by a factor of 65–80, but only by a factor of 7 at the rail gauge corner [249].

¹⁶ $\text{wear} = k_i \sigma_i \delta_i L / H_i$, where i is the distance from the gauge corner, k the wear coefficient, σ the contact stress, δ the mean value of the longitudinal and lateral slip ratios, L the rolling distance, and H the hardness

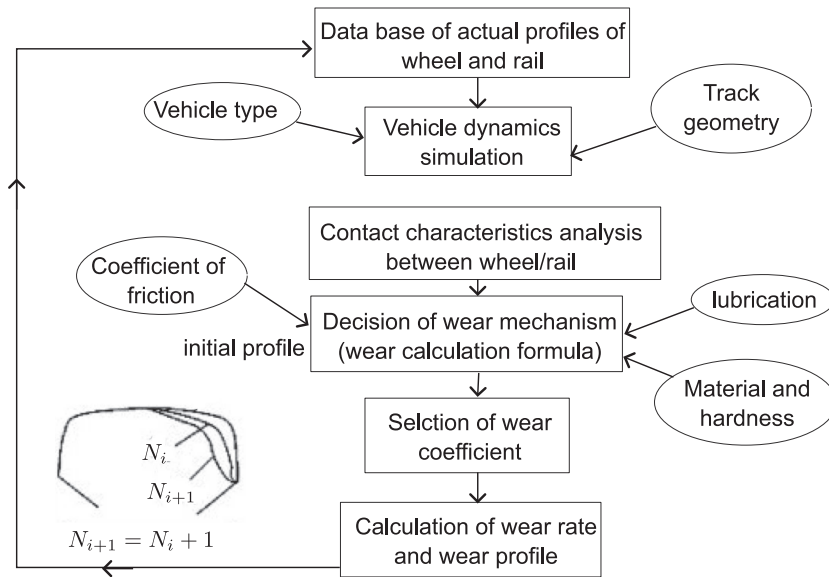
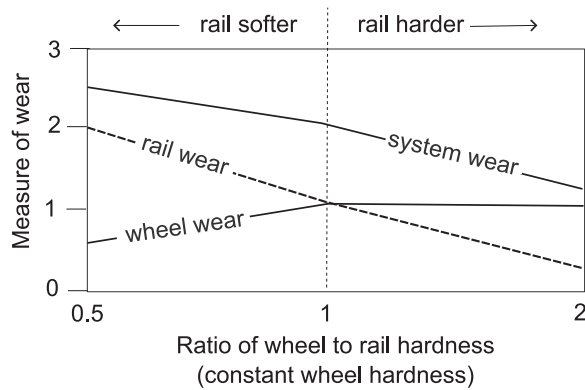
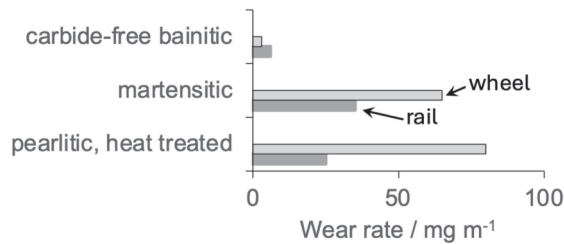


Fig. 33. Rail wear prediction procedure. Reproduced with the permission from Elsevier [249].



(a)



(b)

Fig. 34. (a) Map of the wheel and rail hardness ratio against wear of each component and the whole system. After [271] in [272], with permission of Elsevier. (b) Wear data on a number of rail steels against the same wheel composition [21]. The yield strengths of the pearlitic, martensitic and bainitic rails are 850, 950 and 800 MPa respectively, with the ultimate tensile strengths 1250, 1350 and 1350 MPa respectively.

so its influence and that of other metallurgical parameters is not clear.

At constant hardness, the wear rate is proportional to the load and independent of the apparent area of contact [247]. At small loads (20–50N), the influence of the original hardness on wear volumes is found to be small over a range of microstructures in a eutectoid and a bearing type hypereutectoid steel containing 1.0wt%C. If the load is increased (80N) but kept constant, a decrease in hardness actually leads to a slight decrease in wear volumes [270]. High-carbon specimens austenitised at the lowest possible temperature in the $\gamma + \theta$ field and transformed to either to bainite (345–366 HV) or martensite (772 HV) with carbides and retained austenite, showed no wear volume increase as hardness almost halved. This led to the suggestion that the thermal stability of the microstructure at the operating temperature, is more important for wear resistance than the original hardness [270].

Pointner pointed out that newly installed rails develop a conformal profile with the passage of wheels, that increases the contact area and hence diminishes the contact stresses [272]. Softer rails develop a conformal profile faster than the harder versions, thus showing a smaller initial wear rate, but the advantage obviously diminishes with the progress of service. Therefore, comparisons between different rails should be at the same stage of profile evolution. This is Rotthäuser's explanation of why some decarburised rails, with a softer and more easily worn ferritic surface, exhibit smaller fatigue crack growth rates [276]. However, it has been suggested that decarburisation has a negligible effect on rail performance and that the Rotthäuser observations were attributable to the faster removal of asperities from the soft ferrite, leading to a shorter duration of non-conformal contact stresses, and therefore a longer time to ductility exhaustion needed to nucleate fatigue cracks [277,75]. In twin disc water-lubricated tests [75], greater decarburisation was associated with much increased total and rail wear-rate. Some images of decarburisation and the microstructural change on testing are illustrated in Fig. 35.¹⁷ This result is confirmed in wear studies of mixed ferritic-pearlitic steel as will be discussed in the next section [154,279]. It seems nevertheless that the effects of decarburisation in real rails are likely to be minimal since its maximum allowed depth, as regulated by the British Standards Institute, is 0.5 mm [277,280], necessitating only 25Mt (~1 year of service) for the decarburised layer to wear away and for the ferrite remaining to work harden to a level consistent with the rest of the microstructure [281,75].

4.2. Microstructure

By varying the microstructure at constant composition, it has been shown that wear rates can be similar but the mechanisms different [282,283]. During dry abrasive wear, hard, untempered martensite wore rapidly due to a higher degree of fragmentation or flaking associated with a low fracture ductility [284], whereas nanostructured carbide-free bainite had the highest abrasion resistance attributed to stress-induced martensite hardening at the surface, which also led to minimal pitting; fine pearlite showed extensive pitting due to the stand-out of effect of cementite that halts the sliding motion of abrasive particles [283]. Although dry-abrasion occurs only at the unlubricated gauge face of curved track or after any protective layer of rails has been removed due to high slip-page, this study is effective at pointing out that wear depends not only on bulk hardness, but also on other microstructural parameters which are phase dependent [285].

Consistent with these studies, Wang et al. compared the sliding wear behaviour of five different microstructures in a eutectoid (1080) and hypereutectoid steel (52100), to reach the conclusion that during mild wear ($P \leq 20$ N) there is no significant difference in wear volumes and the degradation mechanism is oxidational wear for all samples. However, for severe wear ($P \geq 50$ N), adhesion and delamination were the dominant mechanisms so harder microstructures did not give better resistance to wear: lamellar pearlite was the most resistant followed by ordinary-bainite,¹⁸ martensite, spheroidised cementite, and tempered martensite with retained austenite [270]. Ductility at a microscopic level matters. Others have found the dry wear-rate of pearlite to be less than that of ordinary-bainite or tempered-martensite, when all three microstructures were generated with the same hardness, in the same rail steel [287]. Pearlite performed the best because of pronounced work hardening at the contact surface. It is interesting that the transition between mild to severe wear modes depends more on testing conditions than microstructure, a conclusion that is difficult to reconcile with notions of microstructural ductility or toughness [250]. Nevertheless, a change in the carbon concentration of steels does lead to a change in the transition conditions between wear modes [263,264].

4.2.1. Pearlite

Cementite-ferrite interfaces in pearlite have a modicum of coherency, which is why the stress-strain curve does not show a Lüders extension even after strain ageing [288,156,289]. The interfaces act as dislocation sources which under stress leads to dislocation pile-ups against cementite lamellae, causing slip band formation. The smaller the slip distance, the more localised the plastic strain, making crack initiation more difficult. This is why lamellar pearlite, which offers a smaller slip distance within the interlamellar ferrite, has a greater sliding wear-resistance than spheroidised pearlite [290,291,270].

Microscopy suggest that cementite can sometimes be sheared at the intersection with the slip bands within the ferrite, Fig. 36 [288].

¹⁷ The depth of decarburisation is defined here as 98% of the bulk carbon content. In this study the carbon profile was estimated through a smart metallographic approach. However, sequential X-ray diffraction measurements using electropolishing are routinely used in the bearing industry and can provide a more precise determination of the carbon content as a function of depth [278].

¹⁸ The adjective *ordinary* is to distinguish cementite-containing bainite from the carbide-free version [286].

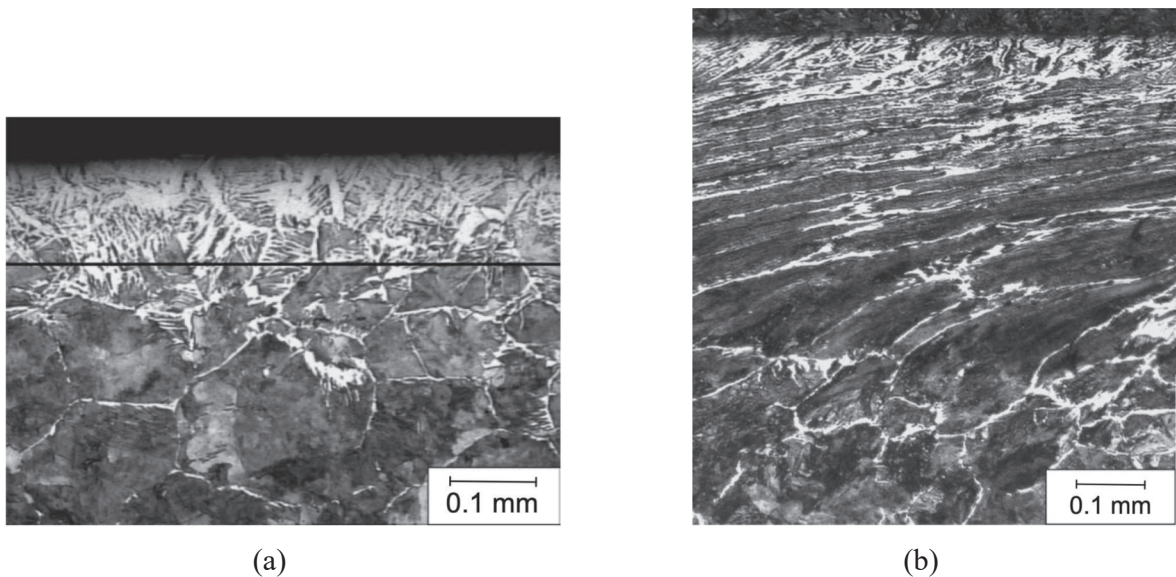


Fig. 35. Decarburisation in: (a) R220 twin disc sample heat-treated in air at 1000 °C for variable times and then ground to the black line. (b) Deformed surface after twin disc testing at 1500 MPa. Reproduced with the permission of Elsevier [75].

Since dislocations pile up at the ferrite-cementite interface, the key to achieving a higher wear resistance in fully pearlitic steel is the reduction of the mean free path of dislocation motion in ferrite, λ , which is achieved by reducing the interlamellar spacing¹⁹, S_I [10,279]. Reducing S_I can be accomplished through chemical composition so that a greater undercooling can be achieved without interference from other transformation products, by the addition of solutes such as chromium or manganese [293], or by employing accelerated cooling from the austenitic state using compressed air or water mist²⁰[166]. Heat-treated grades therefore refer to rails subjected to accelerated cooling in which the hardness is a consequence of the heat treatment itself and therefore, a function of depth. Fine interlamellar spacings of around 70 nm at the railhead surface have also been achieved through thermo-mechanical controlled processing leading to high wear and RCF resistance [294,295].

A reduced interlamellar spacing has been shown to decrease the wear rate almost logarithmically [154], increase the flow stress and work hardening rate [156,288] as well as the hardness (Fig. 37) and yield strength, σ_y , according to the Hall–Petch relationship [296–298,52,299,300,124]

$$\sigma_y = \sigma_i + k_{HP} S_I^{-1/2} \quad (13)$$

where σ_i is the friction stress in the ferrite and k_{HP} is the Hall–Petch parameter, a measure of stress intensity needed at the tip of an arrested slip band to stimulate slip in the adjacent grain [153,301]. The value of σ_i depends slightly on solid solution strengthening but should be about 128 MPa given the small carbon concentration expected within the ferrite and relatively small concentrations of substitutional solutes; $k_{HP} \approx 174 \text{ MPa} \sqrt{\mu\text{m}}$ [124].²¹

The role of cementite here is neglected other than in providing barriers to plasticity, since it is assumed that yielding must first occur in the softer phase ferrite. Therefore, it is no surprise that an increased pearlite hardness, due to interlamellar refinement, decreases the wear rate in a linear fashion with the slope reflecting the contact load and the slip [6,52]. Nevertheless, Perez-Unzueta et al. emphasise that such a relationship is not necessarily linear anymore in the plastically deformed pearlite after wear testing [52].

Decreasing S_I reduces the wear rate during dry rolling wear tests as shown by Das Bakshi et al. who produced nanostructured pearlite (85 nm of interlamellar spacing) with a steel grade meant to form carbide-free nanostructured bainite, and it achieved less wear roughly at the same hardness than some nanostructured bainite alloys [302] or similar wear than other nanobainitic grades but at a lower hardness [303]. Despite a lower specific wear rate, the nanostructured pearlite showed three times as much surface roughness after testing than the nanostructured bainite under the same loading conditions, which according to the authors can exaggerate stresses, induce plastic deformation and hardening up to a depth of 50 μm , increase friction leading to deeper shearing inside the material, and trigger some carbide dissolution as confirmed by X-ray analysis.

Another study performed on an actual nanostructured pearlitic grade with similar bulk hardness but with a much higher slip (20%

¹⁹ Since pearlite is a 3D microstructure of intervening layers of cementite surrounded by ferrite, often visualised as a lettuce (cementite) submerged in water (ferrite), the measurement of distance in two-dimensional sections requires a stereographically correct method such as the mean true interlamellar spacing defined by Underwood [292].

²⁰ The implications in residual stress generation for each cooling method are discussed in more detail in Section 6.

²¹ The units of S_I are assumed to be in micrometres.

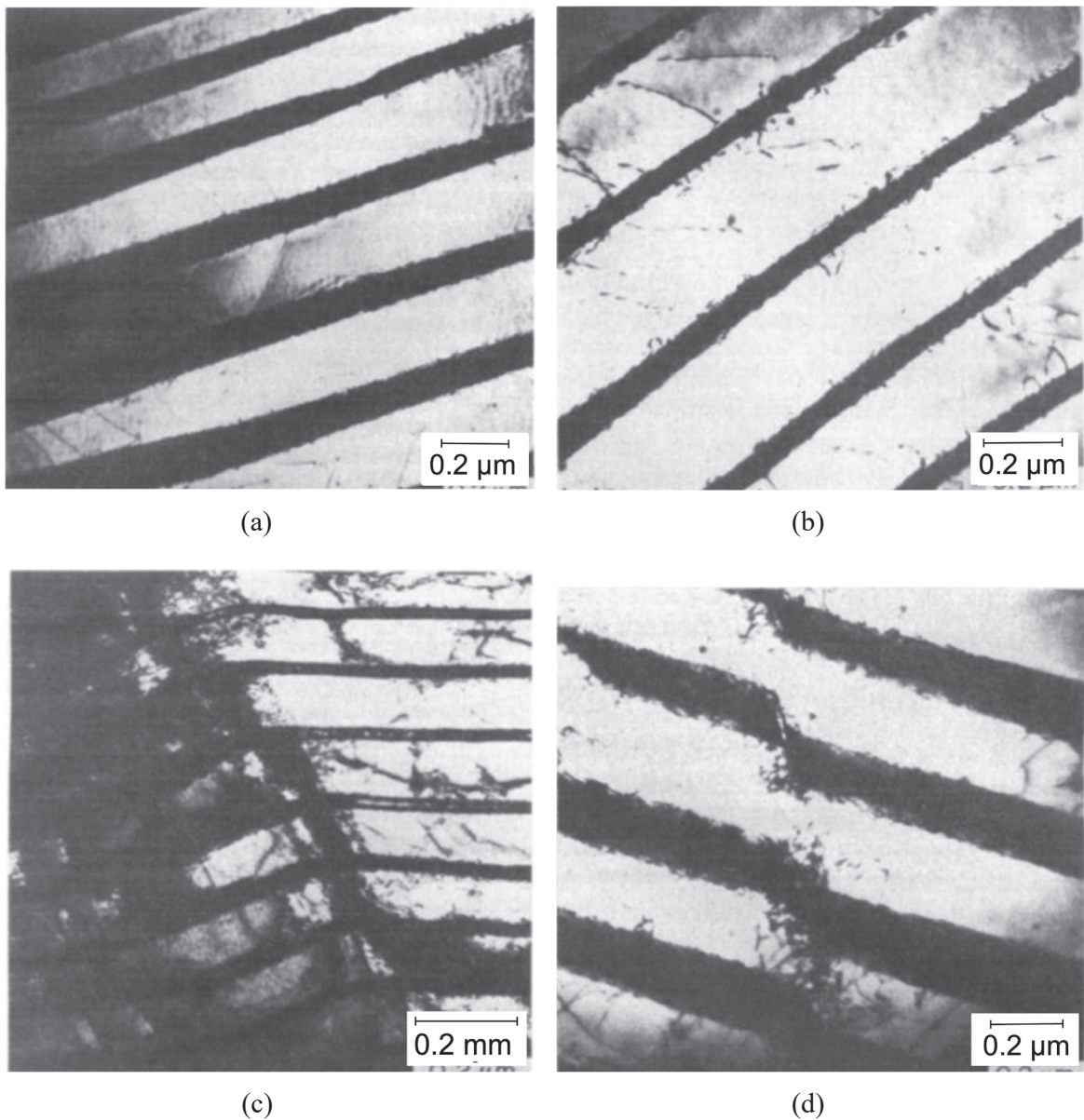


Fig. 36. Transmission electron micrographs of pearlite: (a) undeformed, (b) after deformation with lamellae aligned parallel to tensile axis, (c) after deformation with lamellae aligned perpendicular to tensile axis, and (d) deformation of cementite plates by shear bands. Reproduced with the permission of Elsevier [156].

cf. 5%) in order to simulate extreme wear showed no cementite dissolution, but a large reduction in interlamellar spacing (10-fold), which doubled the hardness at the surface compared to the undeformed matrix [304]. The absence of cementite dissolution may be inconsistent with the measured dissolution in another study [303] which used a fourth of the slip, half the load, a third of the cycles, higher Si content, and the same temperature control during testing. In any case, the observations suggest that moderate wear first realigns the ferrite and cementite lamellae towards the direction of strain and once this has happened, the cementite lamellae thin down, which increases their ductility, permitting them to cope with intense plastic deformation before fracture [305,306]. MnS inclusions also deform and flatten, aiding the generation of flake-like wear particles [52,307,23]. Manganese sulphide is relatively soft, and certainly influences rail performance, but harder inclusions such as alumina, are more harmful in initiating cracks [308], presumably because they do not deform in compliance with the surround steel.

In the context of abrasive wear, the resistance of the pearlite can be expressed as the base wear resistance of ferrite plus a contribution from the cementite particles that is proportional to their volume fraction and inversely proportional to the inter-particle distance [284]. Likewise, for a ferritic/hypoeutectoid steel, its abrasion wear resistance will no longer be related to the pearlitic interlamellar spacing, but will be proportional to the abrasion resistance of the ferrite plus a contribution from the pearlite that is

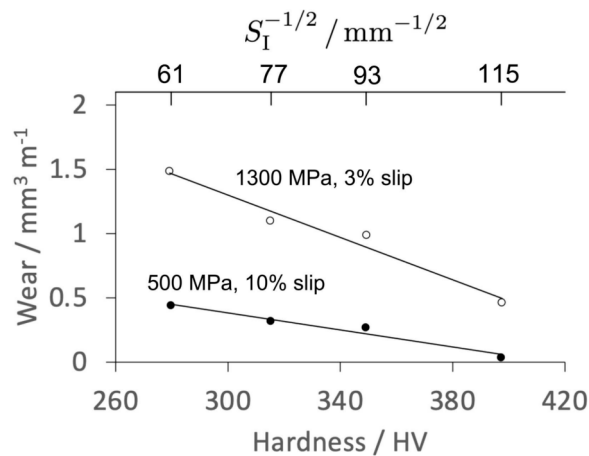


Fig. 37. Wear rate as volume loss per distance slid against initial bulk hardness and interlamellar spacing for different contact pressures and creepage. Redrawn based on data from [52].

proportional to its volume fraction [309,284,299]. In a study of decarburised rails which consisted of ferrite and pearlite at the surface, it was found that wear rates were very similar when the carbon content was above 0.5 wt% (with lower carbon meaning greater ferrite content) making the authors conclude that above this limit, lower amounts of pro-eutectoid ferrite at the surface are unlikely to have a better wear performance [75,50].

Other parameters such as the fracture stress σ_f and ultimate tensile stress σ_{UTS} have been found to increase with decreasing interlamellar spacing, whereas the fracture toughness, K_{IC} , appears to decrease with decreasing interlamellar spacing down to around 170 nm, below which it increases for even finer pearlite [153]. The tensile strength increases with prior austenite grain size if the value of interlamellar spacing is kept constant [293]. The dependence of ductility on interlamellar spacing is less certain or moderate [10,293,153].

As mentioned earlier, the thermal stability of microstructures and their thermal conductivity ($\approx 40 \text{ W m}^{-1} \text{ K}^{-1}$, [310]) can be important at large loads or slip when frictional heating becomes prominent, since properties such as hardness depend on temperature. Data recorded using a thermal camera permitted the modelling of the frictional temperature field, which indicated that for high load/slippage during pin-on-disc testing, pearlite can heat up to 620 °C, martensite to 745 °C and carbide containing tempered martensite with retained austenite to 1340 °C [257]. It is, however, unlikely that those temperatures are reached in normal rail contact²², but the results are consistent with the thermal conductivity trends, with pearlite $51.9 \text{ W m}^{-1} \text{ K}^{-1}$, martensite $29.3 \text{ W m}^{-1} \text{ K}^{-1}$, and cementite $4.2 \text{ W m}^{-1} \text{ K}^{-1}$, respectively. Knowing also that pearlite would only anneal if heated above 700 °C compared to high-carbon martensite, which begins tempering at ~ 200 °C, it makes sense that pearlite had the lowest wear volumes in that study. All the same, such theory is questionable since a spheroidised structure displayed higher wear volumes than martensite despite having higher thermal conductivity and thermal stability than the latter, which suggests that the existence of large and hard incoherent particles such as carbides that can favour the formation of voids and cracks at their interfaces due to plastic flow [314] is a predominant factor for wear resistance than thermal stability.

Niobium, an element commonly added to structural steels to control the austenite grain size and provide precipitation hardening has been shown to increase the tensile strength of pearlite for a given interlamellar spacing, but for reasons that are not clear, it slightly coarsens the interlamellar spacing for a given prior austenite grain size, effectively reducing the wear resistance [293]. However, contradictory results have been reported in [315] where the niobium addition led to a refinement of S_1 and of the pearlite colony size. The microalloying technology has been tested for heavy-haul rails in Brazil [316,317] where it is found that the microalloyed steel has better properties than the one without niobium, and has good flash-butt and thermit welding capabilities. There are other investigations which show enhancements in rail properties and even full-scale rails produced on the normal production lines [318–320]. Unfortunately, there are no report of in service performance of microalloyed rails.

However, microalloying high-carbon rail-steels with niobium can be difficult because it is necessary to ensure that the niobium does not segregate during solidification and form large ($\approx 10 \mu\text{m}$), primary carbides by precipitation from solute-enriched liquid [321]. The amount of niobium must be limited so that even the coarser particles can be taken into solution in austenite during a reasonable reheating treatment. Indeed, adding in excess of 0.05 Nb wt% has been proven to lead to a large deterioration in the toughness of pearlitic rail-steel due to the precipitation of coarse NbC at high temperatures [320]. The concentration in rail steels should therefore be limited to 0.01–0.02 wt% so that precipitation occurs at temperatures where hot-rolling into the rail profile is implemented. Using this design philosophy, it has been possible to produce pancaked austenite grain structures in rails, with a significant improvement in

²² For normal rail contact, contact temperatures have been predicted theoretically to be between 204 °C [311] and 230 °C [312] and determined experimentally to be 300 °C [311,312], although other authors claim it to be up to 1300 °C [313].

wear resistance [321].

4.2.2. Bainite

The ability of ordinary-bainite to resist wear is attributed to its high strain hardening rate and ductility, with the surface hardening but not necessarily detaching which can create abrasive debris [10]. If retained austenite is mixed with the bainitic ferrite in the carbide-free version, the work hardening derives from the strain-induced transformation of the austenite into untempered but very refined martensite [3]. The role of dislocation accumulation at the surface layer during wear that can occasionally produce a cell-like structure has been studied [322]; the cell size depends on factors such as the stacking fault energy, applied stress, and temperature. It can influence the severity of wear and the size of wear particles or to the extent to which cementite dissolves in preference to carbon locating at dislocations [323]. The cell structure is relevant to the discussion of white-etching layers, Section 6.10.

Initial studies concluded that the wear rate of bainitic rail-steels is higher than that of the pearlitic counterparts despite their superior strength [324,325]. Others have shown that mixed bainitic-pearlitic microstructures underperform against fully pearlitic steels, presumably because of the greater work hardening capacity of the latter [326,287,327]. Since then, it has been shown that high-carbon lower bainite can surpass the wear resistance of upper bainite [328], and that low carbon bainite can have comparable or even better wear resistance than pearlite whilst exhibiting better ductility and toughness, making them useful for crossings that are subject to impact erosion and fatigue [329,330]. In the automotive industry, spheroidal graphite cast iron gears transformed to bainite have even shown a similar mass loss during lubricated wear to that of carburised steel during the steady state mode [331] in [282].

Many of the early studies on bainite neglected to consider experimental parameters such as the sliding/rolling ratio, and whether specimens are the upper or lower ones in cylindrical roller testing. In a study that did include these parameters²³, it was seen that a low carbon (0.04 wt%) as-rolled carbide-free bainitic microstructure exhibited a greater wear resistance than pearlite, whereas the higher carbon variants that had banded microstructures of bainite and martensite due to solidification-induced segregation, underperformed. Failure occurred due to a concentration of iron borocarbides at the prior austenite grain boundaries where cracks nucleated and propagated along the bands [10]. However, the low-carbon bainite has a worse wear resistance than pearlite under less severe contact [332,3,6].

A different study that compared wear and rolling contact fatigue of pearlite against bainite at the same hardness, but without mentioning any other experimental parameters, concluded that despite bainite (DOBAIN380 and 430) having approximately 2–3 times less wear resistance than pearlite (R260)²⁴, its RCF resistance was almost four times higher than pearlite, making bainite it a strong candidate for low slip, medium radius curves (1200–1500 m) where RCF damage is enhanced [272].

Other examples exist that compare different types of bainite against each other or against martensite. For example, the wear of a carbide-free bainite was shown to be 50% less than a lower bainite one at similar hardness using a dry 5% rolling/slide ratio, attributable to its advantageous hardness-toughness combination [333]. When comparing it against martensite, bainite had a higher wear resistance due to its higher toughness, work-hardening ability, and smaller hardness differences within the microstructure [270].

4.2.3. Martensite

When pearlite and tempered martensite of identical hardness are generated in the same rail steel, the pearlite is superior in wear, presumably through the role of the cementite lamellae. In fact, for a hardness less than 350 HV, pearlite has a lower specific wear rate than martensite at any given hardness, the difference vanishing for harder martensite [334]. On the other hand, the martensite is less prone to cracking given the fine state of the carbide precipitates within the tempered microstructure [198,270,287]. The martensitic steel always has a low carbon concentration to avoid the brittleness associated with carbon in solid solution, and the hardenability of the steel may not be sufficient to achieve a uniform microstructure in large sections.

In fact, carbides, if they are detached from the martensite during sliding wear, can not only act as abrasives but also cause voids to develop during plastic deformation because of the incompatibility in deformation rates between hard carbides and the softer matrix [314,335]. This is particularly the case at large sliding speeds; in fact, at low speeds the wear resistance seems to be insensitive to the carbide content [336,337]. For these reasons, martensitic steels destined for crossings and switches are based on fully austenitised grades without primary or residual carbides [338].

4.3. Substitutional alloying

Some of the most common alloying elements of rail steel are silicon, manganese and chromium, whilst avoiding impurities such as phosphorus, sulphur, hydrogen, and nitrogen. Silicon is added to carbide-free bainitic steel because it is most effective in suppressing the precipitation of cementite from austenite but has a relatively limited effect during the tempering of supersaturated ferrite. These effects are attributable to the negligible solubility of silicon in cementite; the driving force for precipitation from austenite is much smaller than from ferrite, which is why the influence is much greater in the former case [339–341]. These observations are only relevant when precipitation occurs at temperatures where substitutional solute diffusion is limited so the cementite is forced to accept silicon. At higher temperatures, such as during the formation of pearlite, the effect of silicon on transformation kinetics is very small.

Manganese, on the other hand, under equilibrium distributes preferentially to cementite and lowers the temperature at which it forms, and it enhances hardenability so can reduce the amount of pro-eutectoid ferrite that might precipitate in hypoeutectoid steels,

²³ 35% slide/roll ratio

²⁴ Although the wear rates of these bainitic grades were very similar to harder pearlites such as R350HT and R370CrHT[191].

thereby increasing the hardness [342]. Chromium works in a similar way. Cobalt has been shown to help refine the interlamellar spacing of pearlite by increasing the driving force for pearlite formation from austenite [343]. However, it is probably too expensive in the context of rail steels.

Molybdenum is used for two reasons, it enhances hardenability, but more importantly, it mitigates austenite grain boundary embrittlement due to the segregation of impurities such as phosphorus. This kind of embrittlement is particularly important for transformations that are displacive because bainite and martensite are limited to the grains in which they nucleate and hence leave vestiges of the austenite grain boundaries, where impurities can continue to segregate [344,345]. Other solutes such as vanadium and niobium have been added to experimental pearlitic rail-steels, primarily to attempt a refinement of the austenite grain size [346].

5. Rail breakage – human factors

Breakages develop from cracks that nucleate at weak spots for example at welds or at the foot of the rail when defects are present, although such incidents should be rare due to inspection procedures, commonly using ultrasonics [347]. One of the major rail disasters in the U.K. was the Hatfield crash where apart of the rail fragmented into some 300 pieces as the train passed, probably due to cracks originating in rolling-contact fatigue. Such fatigue is well-known in the rail industry, but the official investigation found that the maintenance contractor at the time failed to manage effectively the inspection and maintenance of the rail at the site of the accident, and that the infrastructure controller at the time, failed to manage effectively the work [348,349].

If detection, for example at the foot, is difficult, cracks can grow unnoticed leading to breakages, assisted perhaps by residual stresses created during heat treatment or track layout. As will be discussed in Section 6, off-line heat treatments and slab track offer lower levels of tensile residual stress at the rail foot than in-line heat treated rails or ballasted track [166]. In the case of manual metal arc weld deposition repairs, the welder's competence and onsite conditions can lead to porosity or slag inclusions that initiate sub-surface cracks that can merge with RCF surface initiated cracks leading to breakage [166].

6. Rolling contact fatigue

Bearing steels, which usually are hard and brittle, suffer from rolling contact fatigue with the cracks originating at surface irregularities or from inclusions or microstructural damage below the contact surface [37,350–352]. The rolling elements of the bearing usually are well lubricated and smooth. In contrast, although rolling contact is clearly a feature of rail traffic, deliberate lubrication is absent, and the process involves some sliding; an interesting consequence of the sliding is that the location of the maximum shear stress caused by the contact moves towards the surface. Fig. 38 shows calculations to illustrate how the location of the maximum shear stress moves towards the surface with increasing sliding component.

Rails also have a much lower hardness than bearing elements. The fatigue cracks in rails nucleate at surface irregularities or asperities that create contact pressure peaks [355,230], sub-surface inclusions/defects [356,357], or at microstructural damage identified as “white-etching” [313]; initiation can also occur in an initially defect-free region when the plasticity in the vicinity of rail surface becomes exhausted (Fig. 39) [198,205,358,206].

Other types of damage due to RCF include pits, squats or head-checks, which are closely spaced cracks, appearing mainly on the rail's running edge. Spalling can occur at the advanced stages of fatigue when bits of the rail fall off as the cracks become sufficiently continuous to lead to detachment. Once “visible” on the rail surface, the cracks are found to penetrate at least 5 mm below the railhead [359]. Therefore, the surface crack length can be used as an indication of crack depth by assuming a penetration crack angle [166]. However, caution needs to be exercised in the interpretation of such data because the direction of crack propagation can change with depth; even ultrasonic measurements of crack depth have been shown to be unreliable when compared with measurements made by sectioning the rail [360].

The life of a fatigue crack can be categorised into two periods: stage I, driven by shear stress, with initiation at the surface, and stage II driven by shear decohesion at its tip in a plane normal to the maximum principal strain with crack growth parallel to the direction of minimum principal strain [362]. This applies to rails as well, where most cracks initiate at the surface by mode II loading fracture (Fig. 40) at an acute angle to the surface due to irregularities or Hertzian contact when elastic shakedown is exceeded, i.e. accumulation of shear deformation due to repeated rolling contact loading. A high surface roughness will increase the stresses and deformation at the surface [230], but a lubricated contact will reduce the friction coefficient locating the peak contact stresses below the surface, at a depth of around 0.2 mm for twin-disc tests and 2 mm in the case of actual rails [221,363,364]. Therefore, cracks nucleated at the surface need to propagate through a region of relatively low stress²⁵, where the microstructure matters in controlling crack propagation, before reaching the deeper peak stress regions. Depending on factors such as shakedown level, material thresholds, and wear rate, newly formed cracks may not propagate if their size is between 10–20 μm . The observation of a low damage subsurface region in gears and bearings under fatigue corresponds to a threshold stress intensity factor ΔK_0 , which is microstructure sensitive [362]. ΔK_0 has been observed to be linearly inverse to the tensile yield strength, proportional to the cyclic yield stress, and independent of the

²⁵ This region has been defined before as a *quiescent zone* or a relatively low shear stress region between the near surface asperity induced field and the subsurface maximum stresses [365].

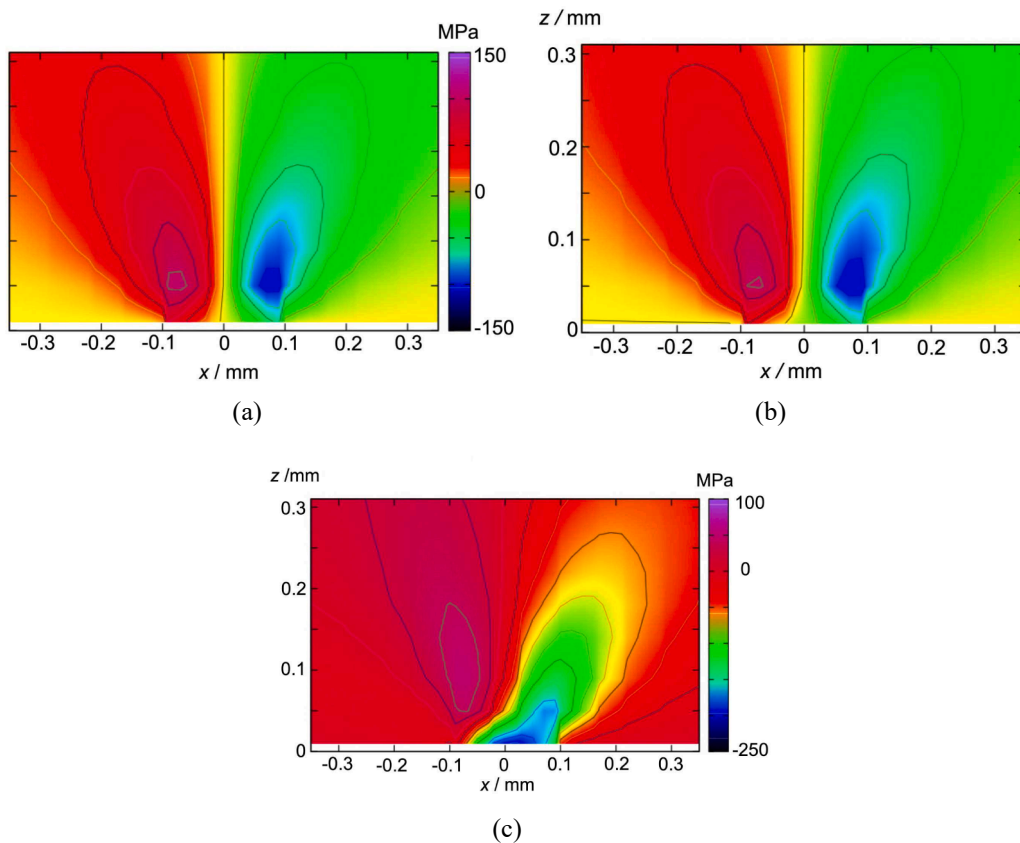


Fig. 38. Calculation according to [207,353] of shear stress τ_{xz} at depth z during rolling contact of two cylinders (each of radius 22.5 mm) pressing together at a load of 200 N. The vertical scales for (a) and (b) are identical, as is the colour scheme. (a) Assuming perfect rolling, (b) roll-slide parameter $\xi = 0.95$, which means that there is 5% sliding, i.e., marginal slip. Note that the vertical depth (z) and colour scales on (a,b) are identical. (c) Assuming perfect sliding of rolling/sliding cylinders. After [354].

fracture toughness [366,367]. Therefore, crack-growth resistance can be improved by cyclic softening,²⁶ coarsening the prior austenite grain size (Section 6.7), and limiting impurity segregation at grain boundaries [368]. If cracks manage to propagate through the quiescent zone, they can grow in mode I fracture, sometimes with the help of near-surface inclusions, in either a co-planar or branching mode (normally at 70° to the initial orientation) [217].

In a pure dry-rolling scenario, RCF cracks have been observed to originate at the surface with a 30° orientation with the surface, penetrate approximately $400\ \mu\text{m}$, branch or propagate parallel to the surface, and rise up again towards the surface creating a macroscopic pit or flake [217]. This behaviour is also referred to as delamination in wear studies [268,209]. If lubrication is added, wear is reduced and macroscopic pits appear after longer duration, but they may grow relatively rapidly [217,356]. Kaneta et al. link the traction coefficient or friction to a particular crack propagation mode such that dry rolling promotes shear mode fatigue growth into the core of the material, whereas lubricated rolling can lead to fluid entrapment at cracks, which decreases friction between the crack faces and gives rise to a tensile growth mode that generates pits [369].

Others conclude that the selection of either of these mechanisms depends on the anisotropic accumulation of shear strain, such that narrow regions of exhausted ductility surrounded by others which are less strained will be preferential sites for crack propagation into the core of the material; uniformly strained regions simply produce wear debris [370]. The microstructural parameter responsible for the anisotropic accumulation of strain is not clear since the modelling uses rectangular elements with assumed local properties. Su and Clayton find that for lubricated rolling/sliding, the cracking behaviour during RCF depends more on the contact pressure and shear yield stress than on the friction coefficient or microstructure [196]. This result is supported by the findings of Beynon et al. [50] who found a critical contact stress of around 1500–1800 MPa for lubricated rail discs below which cracks formed networks and above which they grew isolated and deep into the material (Fig. 41).

A factor often neglected in the analysis of fatigue cracks in the context of rails, is the influence of residual stresses due to heat

²⁶ Cyclic softening can be induced by the rearrangement of the dislocation substructure and a reduction in dislocation density with alternating load. The softening occurs because some of the plastic strain becomes reversible, similar to phenomena during the Bauschinger effect. It has a noticeable beneficial effect on the threshold fatigue crack growth resistance.

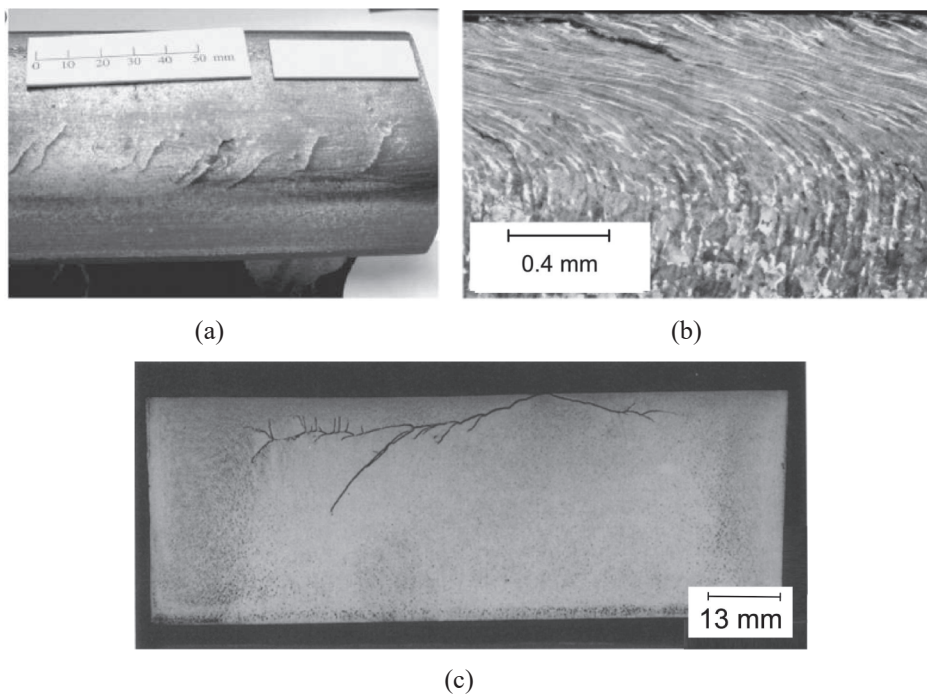


Fig. 39. Damage due to rolling-contact fatigue on rails. (a) Family of surface cracks at the gauge corner aligned normal to the resultant of the axial, spin, and transverse creepage directions. (b) Matrix strain below the contact surface, illustrating a crack growing in the direction of plastic flow. (c) Branched crack visible in a longitudinal section of a rail in a high-speed curve, also referred to as a squat defect. Reproduced with the permission of Elsevier [361,50].

treatment and track layout. A ballast-less slab track, Fig. 42, where the rails are fastened onto rigid concrete slabs with some sort of elasticity engineered into the system, exhibits a smaller subsurface crack growth rate, due the increased and continuous support that reduces rail bending, when compared to the traditional ballasted track [166]. Data suggest that the ratio of sub-surface crack depth to surface crack length is much lower for slab track than for the ballast equivalent, although it is noted that many of the slab track installations are located in tunnelled sections that are sheltered from the possible effects of fluid pressurisation in helping crack advance.

It is also argued [166] that an off-line heat treatment mitigates residual tensile stresses at the rail foot, leading to an increased fatigue life. This is caused by the fact that off-line heat treated rails do not undergo roller straightening after their controlled forced air cooling as opposed to in-line heat treated rails, which are cooled using water, air-mist or polymers after rolling. In-line heat treatment would also give rise to a larger prior austenite grain size whereas the off-line process requires a shorter and lower temperature re-austenitisation stage resulting in finer prior austenite grains, which can reduce hardenability, but increase the toughness.

There are two main approaches to the modelling of crack initiation:

1. a defect tolerant one in which the material is assumed to be inherently full of small cracks and it is the number of cycles to propagation to a critical size that is calculated based on material parameters and crack growth data.
2. A total life one where the cycles to crack initiation in a defect-free material are considered either in a stress or strain based model [235].

The material properties are then considered using a constitutive model, for example the Armstrong and Frederick nonlinear kinematic hardening law for steady state ratcheting [371], the Lemaitre and Chaboche model for a more accurate description of low cycle ratcheting [372], or the Jiang and Sehitoglu model for long term constant or decaying ratcheting rate and transient loading [373,374]. A loading contact model, normally done using a finite element method, then needs to be added. Different fatigue prediction approaches, reviewed carefully by Ringsberg [235] and compared by Ekh et al. [375], can be incorporated using concepts such as equivalent strain, critical plane, energy and energy-density, combined energy-density and critical plane (recommended for rolling contact fatigue), or empirical models. These theories can then help predict the most critical point and orientation for a crack to nucleate due to ratcheting or low-cycle fatigue, grow according to fatigue damage calculations, and be compared against experimental tests that calibrate the output. Since ratcheting leads to a change in the material parameters, plasticity models need to account for this anisotropy evolution, which has been attempted before by splitting up the bulk of the material into elements designated “bricks”. Each brick is assigned different properties such as initial shear yield stress and critical shear strain depending on depth, so each accumulates plastic shear strain at varying rates and can fail individually when the threshold is reached and form wear debris or cracks [376,221].

RCF cracks can be partially or entirely eliminated by the wearing away of surface material, since rails are systems where wear and

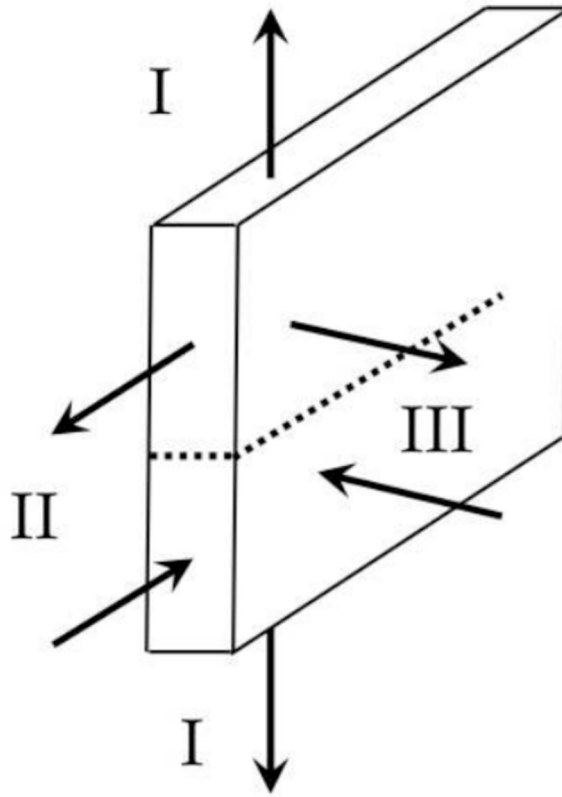


Fig. 40. Three modes of crack loading. Redrawn based on [362].

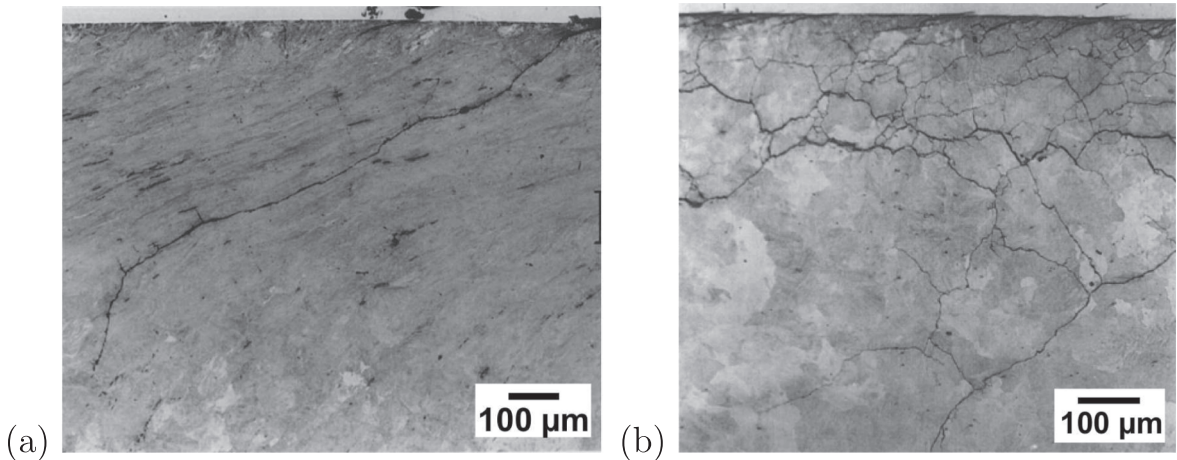


Fig. 41. Optical image of eutectoid grade showing: (a) isolated crack while tested at $p_0 = 1800$ MPa and (b) fine crack network while tested at $p_0 = 1500$ MPa. Reproduced with the permission of Elsevier [50].

rolling contact fatigue take part concurrently [377,221,378]. The competitive role between these two mechanisms has been simulated [217] by calculating the depth of the wear per cycle and the Paris law propagation rate of fatigue cracks as shown in Fig. 43 such that the higher curve dictates the prevalent mechanism. They also developed a ratcheting model based on Lemaitre and Chaboche [372] that estimates RCF shear band crack formation in competition with wear, calibrated experimentally by extracting the hardness and



Fig. 42. A ballast-less track between rail tunnels under a river in the Netherlands. Reproduced under CC BY-SA 3.0, <https://creativecommons.org/licenses/by-sa/3.0/deed.en>, courtesy of Hullie.

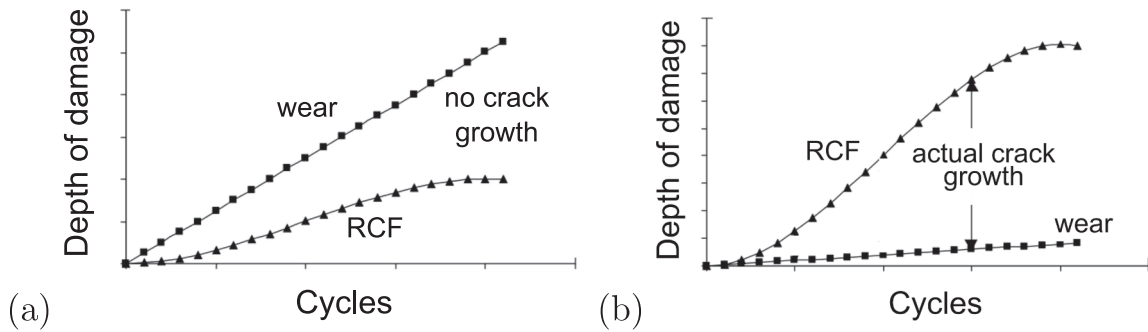


Fig. 43. Qualitative graph showing a scenario where a) wear is predominant so no surface crack failure can be expected and b) RCF is predominant so wear does not manage to remove surface cracks that can ultimately lead to failure. Adapted and reproduced with the permission of Elsevier [217].

forward displacements along the depth of twin-disc samples and the thickness of the layer removed by wear [379]. The wear stabilises the strain field at high cycles and during the steady state, crack length is almost constant due to wear removing the same thickness of material as the distance advanced by the crack tip²⁷.

Another model to simulate the competition between fatigue and wear is based on a graphical representation of a brick model, with a black or white pixel for a failed or un-failed brick, respectively; cracks are then identified as a chain of black pixels, or wear debris if a whole layer of bricks is black [370]. Although this does not predict cycles to wear initiation or rates observed experimentally [380] due to the lack of microstructure and roughness simulation, the depth of RCF cracks was similar to experiments after 15,000 cycles but the crack length was under-predicted, probably due to the neglect of stress concentrators at the tips of the cracks.

The wear rate of rails has decreased by over an order of magnitude over the past two decades due to a better understanding of damage mechanisms and of microstructural tailoring, but with consequent increase in the occurrence of fatigue damage [252]. RCF cracks can be removed by wear, but there is currently no quantitative description of what magnitudes of speed, load, creepage, and cycles should be for wear to grind only the necessary amount of cracked rail surface (*magic wear rate* [378]), although Olofsson

²⁷ The constant crack length was established to be 40 μm by Fletcher and Beynon in unlubricated tests [220].

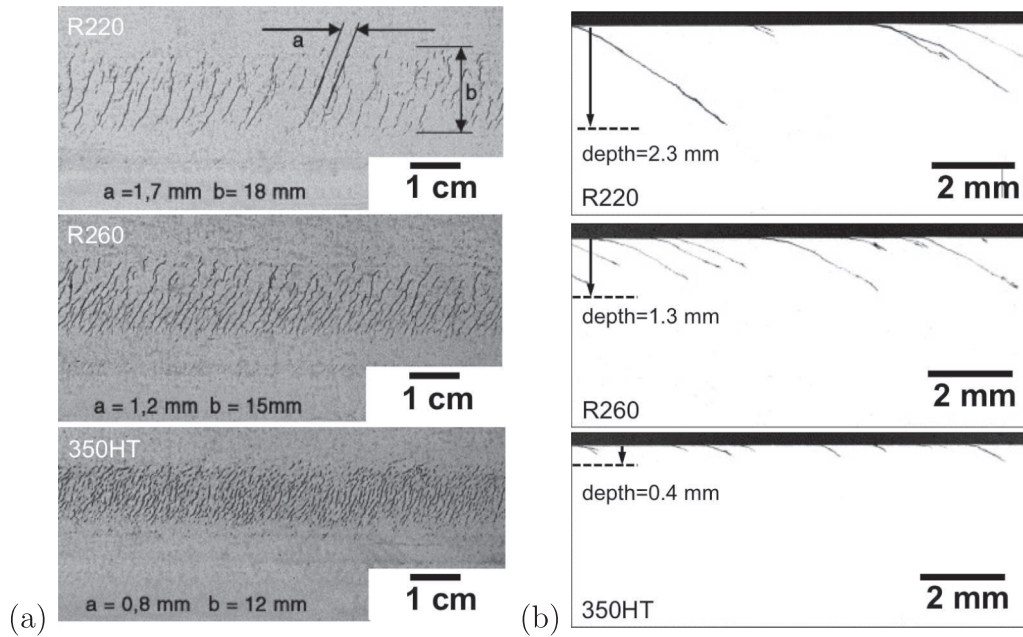


Fig. 44. High-speed lines made with grades R220 (as-rolled), R260 (as-rolled), and R350HT (head hardened through heat treatment) showing: a) density, size, and spacing of head checks using magnetic particle inspection of the head surface near the gauge corner after 90MGt (million gross tonnes, 3 years) of service and b) angle (25°) and depth of head checks in longitudinal micrographs after 85MGt (2.5 years). Adapted and reproduced with the permission of Elsevier [54].

concluded that if the steel grade is too wear resistant²⁸, lubricants with friction modifiers (lithium-based grease with graphite) can slow RCF crack propagation rates so they match removal by wear [381]. Recent efforts to model the process of RCF crack nucleation and growth taking into account steel composition and wear by the UK's Rail Safety and Standards Board, have been validated against historical site data, allowing the optimisation of grinding schedules [382].

6.1. Hardness

It is well documented that a refined interlamellar spacing in pearlite increases its hardness and consequently, decreases its wear rate [6,52,293,154]. Such dependence with hardness has not been studied as much in the case of RCF, but the most data certainly originates from a large set of over 1200 laboratory twin disc tests performed at TATA Steel since 1976 covering a wide range of steel grades that showed a linear dependence of hardness with RCF resistance measured as cycles to crack initiation despite the uncertainty of accurately detecting crack initiation [166]. Since hardness is commonly achieved through a combination of adequate alloying and accelerated cooling, it should be taken into account when assessing RCF resistance that hardness can vary along the length and depth, and therefore with material loss through wear or maintenance grinding activities.

Fracture toughness has been observed to decrease with increasing hardness for the as-rolled rails, from $\approx 35 \text{ MPa m}^{-1/2}$ for R200 (220 HV) to $26 \text{ MPa m}^{-1/2}$ for R320Cr (340 HV). However, for the heat-treated grades (370–420 HV) the minimum mean values were similar to those of R260 (280 HV), which is around $29 \text{ MPa m}^{-1/2}$ [166], suggesting an independent effect of interlamellar spacing [166], perhaps because the cementite lamellae becomes thinner.

Fatigue crack growth rates are greater for harder steels, increasing from of $\sim 21 \text{ mGcycle}^{-1}$ for a hardness of 230 HV to $\sim 35 \text{ mGcycle}^{-1}$ for 370 HV [166]. Another study that compared as-rolled (240–280 HV) and heat treated rail steels (370 HV) in actual wheel-rail conditions found that head the hardened rail showed not only the shortest head check cracks with the smallest distance between cracks, but also a crack depth 3–6 times lower than the as-rolled rails (Fig. 44), meaning that harder rails do offer more RCF resistance together with reduced wear [54]; this should not surprise because in ordinary push-pull tests, the fatigue limit correlates well with hardness over a wide variety of steels and microstructures [383–385]; after all, the resistance to plastic deformation as measured by hardness indentations, determines also the resistance to the plasticity required to initiate and propagate fatigue [386].

It follows that head-hardened rails require less maintenance by grinding, offering an improvement of 2–3 times in operating efficiency with respect to R260 [54]. Nevertheless, it is worth pointing out that the larger linear density of cracks in the hard heat-treated rails and the short distance between cracks can increase the propensity of spalling or shelling as a result of cracks merging together

²⁸ New pearlitic rail with a composition of 0.7C-1.0Mn-1.0Cr wt% and a UTS $\geq 1080 \text{ MPa}$ installed in a 346m curve which experienced speeds of 75 km h^{-1} and an average traffic of 6 Mt year^{-1} .

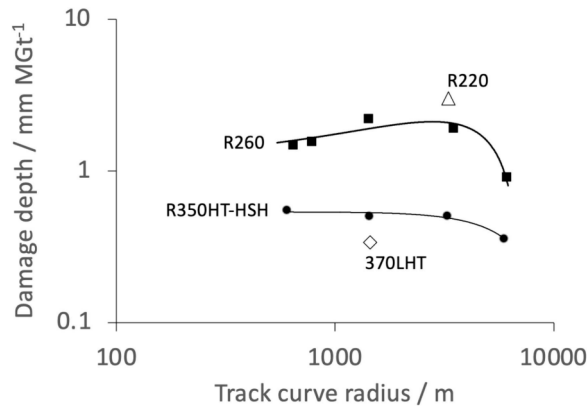


Fig. 45. Depth of RCF cracks as a function of track curve radii. The hardness values are 240 HV for R220, 280 HV for R260, 370 HV for R350HT, and 390 HV for R370CrHT. Adapted using data from [272] based on [387].

under the surface [166]. A similar dependence with hardness was found by Beynon et al. who varied the contact pressure and creepage in a twin disc machine concluding that a head hardened eutectoid pearlite (0.76 wt% C) had the best resistance to RCF followed by an as-rolled eutectoid grade (0.78 wt% C) with a similar composition to STD, and last came a low strength BS11 grade with only 0.55 wt% C [50].

When including also the track curve radius in the analysis, it was found not only that harder rails form shallower head check cracks irrespective of curve radii, but also that the maximum condition of RCF damage in terms of deeper cracks occurs in curves of 1200–1500 m in radius (Fig. 45) [272,387].

6.2. Single empirical parameters

Rolling contact fatigue is a function many parameters including surface roughness, load, rolling speed, steel cleanliness, heat treatment, chemical composition, and response to thermomechanical deformation. The influence of each of these can be quantified by direct measurement [194]. Using such data, attempts have been made to rationalise clusters of variables into a single empirical parameter, e.g., the *shelling index* that in some respects accounts for inclusions and hardness, to allow comparison of RCF performance between alloys [388]:

$$\text{shell index} = \ln \left\{ \frac{\text{oxide volume fraction} \times \text{stringer length}}{\text{hardness}^2} \right\} \tag{14}$$

A shell is a bit that falls off a rail because of a fatigue-initiated crack, often referred to as a spall; Eq. 10 clearly does not have a physical basis, but is consistent with the discussion in the previous section that in general, a greater hardness offers better fatigue resistance, since the tendency for shelling has been shown to be smallest when the shell index is smallest [388]. The shell index is probably less relevant for modern rail steels which have a high cleanliness level due to, for example, vacuum degassing and continuous casting [389] or calcium treatment [390], Fig. 46.

Some have tried to include other variables, such as the volume fraction and size of alumina particles, the austenite grain size, degree of structural homogeneity, intensity of thermomechanical deformation, and carbide volume fraction [194]. However, the degree of empiricism increases and it may then be better to use neural network analysis [392].

Other attempts to use a single parameter for rolling contact fatigue analysis, such as the *Smith-Watson-Topper* method [393], designed originally to help estimate the fatigue life during uniaxial loading in push-pull tests, involves a damage parameter $S^{WT} = \sigma_{\max} \epsilon_a$ that is the product of the maximum tensile stress and the strain amplitude. The idea is that fatigue failure under different mean stresses and range all can be rationalised as a monotonic function of the parameter; the original work [393] demonstrated this vividly for a wide range of data. In the context of rails, finite element analysis is used to estimate the location of crack nucleation and the direction of its growth under multiaxial cyclic loading based on a phenomenological approach considering the maximum normal stress component σ_{\max} in a specified direction, and $\Delta\epsilon$ is the difference of the maximum and minimum normal strain components in the same direction:

$$S^{WT} = \sigma_{\max} \frac{\Delta\epsilon}{2}$$

S^{WT} is therefore a function of position in space and is assumed to be constant for a given life. Using this in a scenario to estimate fatigue life under three-dimensional cyclic loading requires the calculation to be performed over a whole structure and to find the location of the maximum S^{WT}_{\max} value that would correspond to the location of crack initiation making this method computationally intensive for large sections of rail [394]. However, one of the strengths of this approach is that it can predict if crack initiation occurs in the

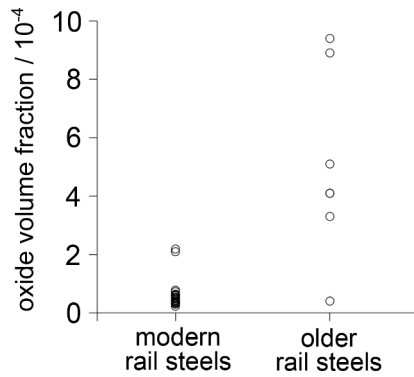


Fig. 46. A comparison of the volume fractions of oxides in rail steels used to derive equation 1o [388] and a large number of modern rail-steels sourced from Russia, Japan, France, Austria and Poland [391].

subsurface of the rail head. Nevertheless, still the most common way of assessing rolling contact fatigue resistance is to test samples under standardised conditions such as load and speed until the first signs of damage are evident and the test is stopped for characterisation.

6.3. Contact pressure and creepage

In general, RCF life increases with decreasing contact pressure but the exact relationship these two variables follow was initially thought to be linear using standard pearlitic steels in twin-disc laboratory tests [395,396,50]. Instead, increasing creepage up to 3% was found to increase the RCF life in hypoeutectoid and as-rolled eutectoid pearlites [50].

When using a broader range of lubricated contact pressures from 850–2300 MPa, it was observed by Su et al. that a more accurate description would be a power law (RCF life = $A p_0^b$), where A and b are empirical constants. Nonetheless, microstructural characterisation in that study revealed two different failure modes: low RCF lives and shear band cracks in loading cases above the theoretical shakedown limit or branched cracks that originate from an apparently undeformed material when loaded below the shakedown limit allowing a longer RCF life. These modes suggests a bimodal distribution based on the normalised values of contact pressure p_0/k where k , the shear yield stress, is $\sigma_{0.2}/\sqrt{3}$ [196]. In either case, the initial failure mechanism is shear flow at the surface that leads to work hardening, exhaustion of ductility, and eventual crack formation and orientation along the flow lines. However, a shear band cracking mode would require different aspects to be addressed such as the ratcheting strain rate to avoid crack nucleation, whereas the branch cracking mode could be mitigated via austenite grain size refinement or by increasing wear resistance if these branched cracks are the early stages of delamination flakes.

The contact pressure at the tip of RCF cracks can be exacerbated by the presence of lubricant inside the cracks. Under constant lubrication, the traction coefficient decreases giving a slower build-up of ratcheting damage so the time to crack initiation is longer [221]. However, normal rail-wheel contact is not constantly lubricated but is a combination of dry and wet contact depending on the weather. If cracks have been formed during a dry stage and lubrication is then applied, it is believed that liquid can enter the crack mouth cavity creating mode I crack propagation, reducing the friction between faces, and accelerating the crack growth rate; this known as the hydraulic pressure penetration effect [356,217,397,369]. Upon loading, the liquid can also escape the crack mouth and lubricate the crack faces causing mode II propagation [398,206]. By using such model and measuring the effective dry cycles N_{eff} that a sample sees once the shakedown limit is reached and the friction coefficient raises above 0.25, but before lubrication is applied, and then calculating the load above the ratcheting limit P_r , it is possible to calculate the decrease in RCF life according to [206]:

$$\% \text{drop in RCF} = 2.74 P_r N_{\text{eff}}^{0.5} \quad (15)$$

Its is worth mentioning that this hydraulic pressurisation effect is inversely related to the liquid viscosity and directly proportional to the crack length [217]. Other models available to simulate such phenomenon include quasi-static two dimensional approaches where lubrication seepage was found to be proportional to increasing surface traction and crack inclination with respect to movement [369], 3D models (used to determine relations to approximate 2D to 3D cracks such as a stiffening reduction factor and a growth rate reduction factor)[399], and models that couple internal and external pressure applied by internal fluid flow and external contact load [400].

Although many authors talk about fluid penetration at cracks and its essential role in RCF crack propagation [401], the actual mechanism by which fluid enters those shallow angle 3D thin RCF cracks is not entirely understood. In order to corroborate a common assumption that water gets sucked into newly formed RCF cracks during the first cycle due to a sub-atmospheric internal pressure, Bogdanski coupled a Hertzian 2D FEM model of a surface-breaking shallow-angle crack and a one-dimensional Reynolds squeeze film fluid model for pressure dependent viscosity liquids [400]. He showed that for the liquid to get sucked in, the liquid layer needs to be continuous, but already train speeds above 0.9 ms^{-1} will break it suggesting that other mechanisms may be more plausible explanations for this phenomenon, such as slow capillary flow after the cracked faces have been eroded due to friction. Nevertheless, crack

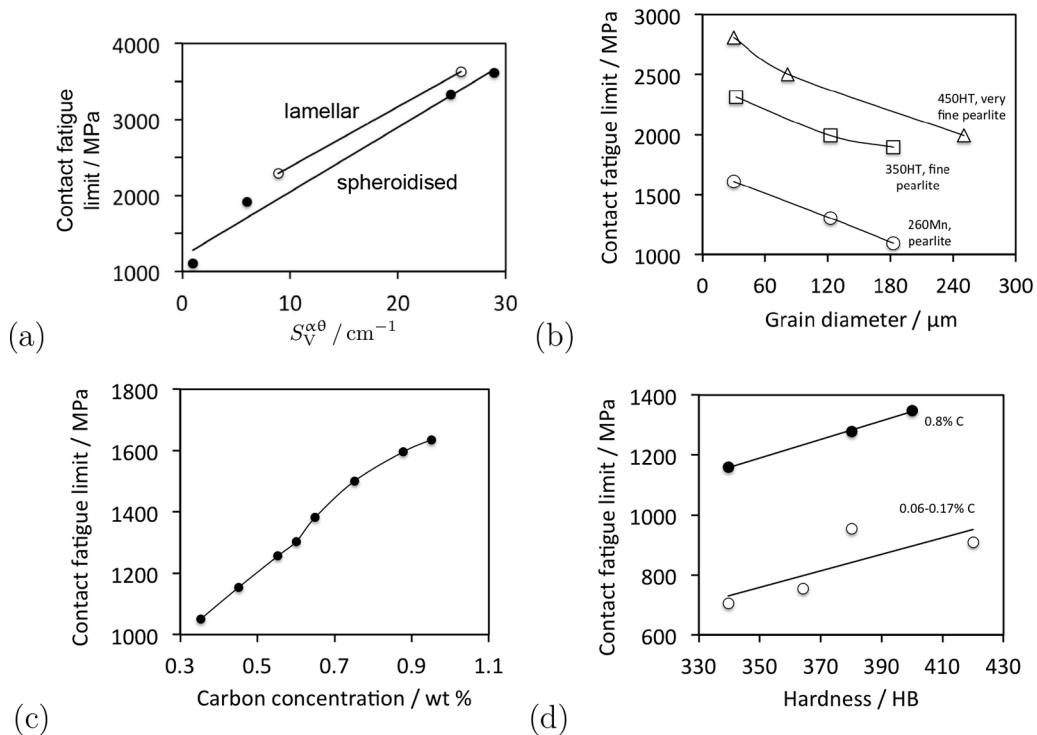


Fig. 47. Rolling contact fatigue dependance on (a) interphase surface of pearlite (lamellar vs spheroidised), (b) austenite grain size, (c) carbon content and (d) hardness of a low carbon martensite vs a high carbon fine pearlite, The exact definition of the contact fatigue limiting stress is not clear from [194] but may relate to the maximum contact stress during roller-roller tests necessary to achieve a determined number of cycles without crack initiation, as described in [406]. Similarly, the definition of austenite grain diameter is not specified in the original work. Data from [194].

propagation due to entrapped fluid seems to be negligible knowing that the continuous passage of trains pushes the entrapped fluid out due to the contact pressure ahead of the crack making refilling very difficult in busy routes [402].

6.4. Microstructure

6.4.1. Pearlite

By using grade R260Mn (Table 4) and applying different cooling rates to achieve different grades of pearlite from lamellar to globular, Shur et al. concluded that lamellar structures, as opposed to spheroidised ones have a higher RCF resistance, Fig. 47a, because of the ability of such microstructure to strain harden to relatively large depths, thus spreading the deformation and reducing the gradient of mechanical properties from the surface to the subsurface [194,403]. This ability comes from the ease of dislocation generation at the carbide lamellae that can then create a fine ferritic cell substructure, a mechanism well-established in studies of heavily drawn pearlitic wires [404,405].

The same conclusion that lamellar pearlite is more RCF resistant than a spheroidised one was also reached whilst simulating high speed train conditions in wheel steel (500 km h^{-1}) despite the fact that the spheroidised structure had a 30% greater yield strength and 5% higher ultimate tensile strength at the same hardness than the lamellar pearlite [407]. It is important to point out that the degradation mechanisms of each structure were quite different with the spheroidised pearlite showing a higher weight loss but a smoother surface with some deep pits, whereas the lamellar one had shallower flake pits but a more fragmented surface due to cracks propagating along the direction of plastic flow, formed presumably when plasticity is exhausted, as depicted in Fig. 39b.

In an evaluation of the effects of microstructural variations on the mechanical properties of eutectoid rail steels, it was concluded that fatigue crack initiation was dependent on the interlamellar spacing, making coarse pearlite more susceptible to cracking, but with little or no effect during the propagation stage [293]. Since most cracks in rails are not initiated by a process of fatigue but rolling contact fatigue through plastic shakedown, ratcheting, or squats, it can be then said that refining the interlamellar spacing will not necessarily improve its rolling contact fatigue properties, as it can its wear resistance [279,154,6,52,10].

6.4.2. Bainite

In a study that compared standard (STD) and head hardened (HH) pearlitic steels against three different bainitic steels: EBS-4, carbide free with some granular bainite, EBS-5, lower bainite, and EBS-6, granular bainite (Table 4), it was seen that EBS-4 showed the largest RCF resistance. This was attributed to its higher hardness, leading to the conclusion that RCF resistance increases with strength irrespective of microstructure or work-hardening capacity [196]. The slip-roll ratio was not varied, which could highlight the

role of microstructure on rolling contact fatigue. Other studies have shown conflicting results, where not only the hardness but the size and morphology of the bainite were strongly related to RCF since coarse/granular bainite provided less resistance to crack initiation than the acicular type due to its high angle boundaries [408].

In full scale tests using commercial pearlitic and bainitic grades at specific points of the German railway network, bainitic grades (DOBAIN380 and 430) showed as few head-check cracking as heat treated pearlitic steels (R350HT or 370LHT) in a 1300–1500 m radius curve and the same wear rates, but in a heavy-haul track or at tight curves, the bainitic DOBAIN430 track showed no head-check cracks, whereas R350HT exhibited such cracks even after 70 MGt, proving the superior resistance of the bainitic grades not only in RCF but also by matching the wear properties of head-hardened pearlite [191].

6.5. Mixed microstructures

Mixed microstructures can be achieved either intentionally through heat treatment or accidentally due to chemical segregation, stress-induced transformations, or localised temperature spikes due to friction that can induce tempering, recrystallisation, or even partial re-austenitisation [313]. In most cases the unintentional creation of additional phases compromises the RCF resistance [194], but the focus here is on intentional mixed microstructures.

In one study, grade 450HT (Table 4) was heat treated in different ways to achieve either a mixture of martensite and fine lamellar-pearlite (the latter in amounts from 5–50%) or a fully martensitic state, adequately tempered to achieve the same hardness as the mixed phase samples. The RCF resistance abruptly decreased as the amount of fine pearlite increased, inferring that mixed microstructures perform worse than those that are homogenous [194], presumably because deformation becomes focused in the softer phase.

As a comparison, mixed microstructures have performed well as bearing steels, where fully nanobainitic structures are not hard enough²⁹ to provide enough dimensional stability, but a mixed microstructure containing martensite, residual carbides, retained austenite, and 0.21 volume fraction of nanobainite (average hardness 825HV) had a greater impact toughness (12J) than the fully bainitic steel (3J), leading to a fivefold increase in the RCF life [411]. The reason for these differences between rail and bearing steels is not clear, but the production scale in the former case is much larger, meaning that the heterogeneities are likely to be on larger length scales, for example, as banding, rather than as a uniform mixture of phases.

6.6. Damage in wheels

Some of the most prevalent types of rolling contact fatigue damage in freight car wheels include spalling, shelling, and thread cracking [218,412]. Spalling occurs when heavy braking/gross sliding raises the surface temperature above austenitisation giving rise to martensite layers of 0.1–1.2 mm thick upon cooling, which can then fracture and spall. These spalls are normally caused by defective brakes or due to inadequate lubricant use. Thread cracking refers to fine, angled surface cracks nucleated at the circumference of the wheel thread as a result of ratcheting, which can develop into spalls (Fig. 48a).

Finally, thread shelling (Fig. 48b) resulting in craters \approx 5 mm deep, with characteristic fatigue rings initiated at inclusions [218,413]. By modelling the contact geometries of new and used wheels and rails, it was found that increasing the friction coefficient proportionally increases the longitudinal and lateral maximum shear stresses and shifts the region of plastic flow from below the surface (4 mm deep) to the surface, whereas changing the creepage alters the size and position of the contact patch [218]. The particular combination of parameters that gives rise to these defects is, however, not established.

In order to investigate the qualitative influence of different parameters such as wheel diameter, radius of rail, residual stresses, and vertical and horizontal loads on the rolling contact fatigue damage of wheels without tread braking, Ekberg constructed an equivalent stress criterion model that evaluates the magnitude of the local shear stress, compares this against the fatigue limit of the material in pure shear to dictate if damage occurs, quantifies damage as the number of cycles to failure for the current magnitude of stress, and applies it to a failure criterion [414]. Results confirmed an increased damage for increasing load, decreasing wheel diameter, and decreasing rail radius, as well as confirmation of the well-known [415,416] beneficial influence of compressive residual stresses, the detrimental role of tensile residual stress, and the displacement of subsurface shear stress damage towards the surface for increasing horizontal load. These parameters indicate that faster/heavy-haul trains as well as rail grinding (if it increases rail radius) increase the propensity of wheel fatigue failure over wear.

6.7. Austenite grain size and pro-eutectoid phases

Using rail grade R260Mn (Table 4) heat treated to fine and spheroidised pearlitic microstructures with different austenite grain sizes, R350HT, and a variation of R450HT containing Zr, V, Nb, and Ce (detailed composition not specified) but similar tensile strength and hardness, it has been shown that smaller austenite grain sizes lead to a higher contact fatigue limit, as long as large carbide clusters are absent [417,194,418,419], as illustrated on Fig. 47b. The mechanism for this improvement of the RCF performance is not explained.

Other studies in a different context indicate that the austenite grain size has a minimal or no effect on rolling contact fatigue or the

²⁹ maximum of 670HV [409] compared to the minimum required 690HV [410]

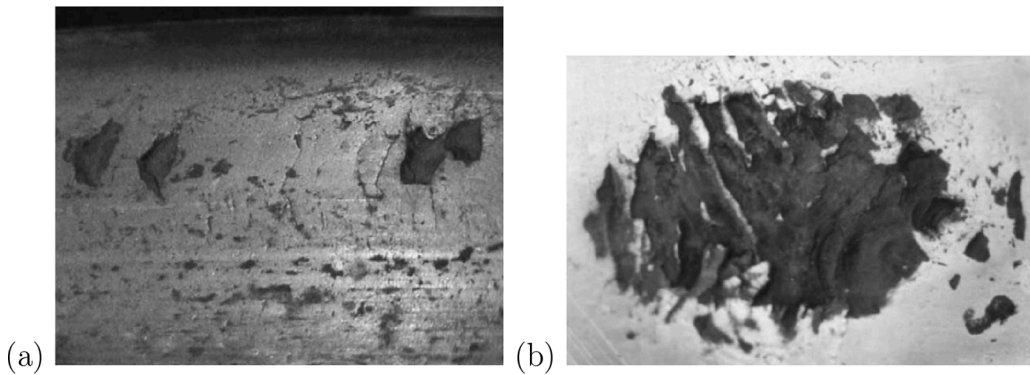


Fig. 48. Wheel damage in the form of (a) spalls caused by advanced thread cracking and (b) thread shell (no scale in original source). Reproduced with permission of Elsevier [218].

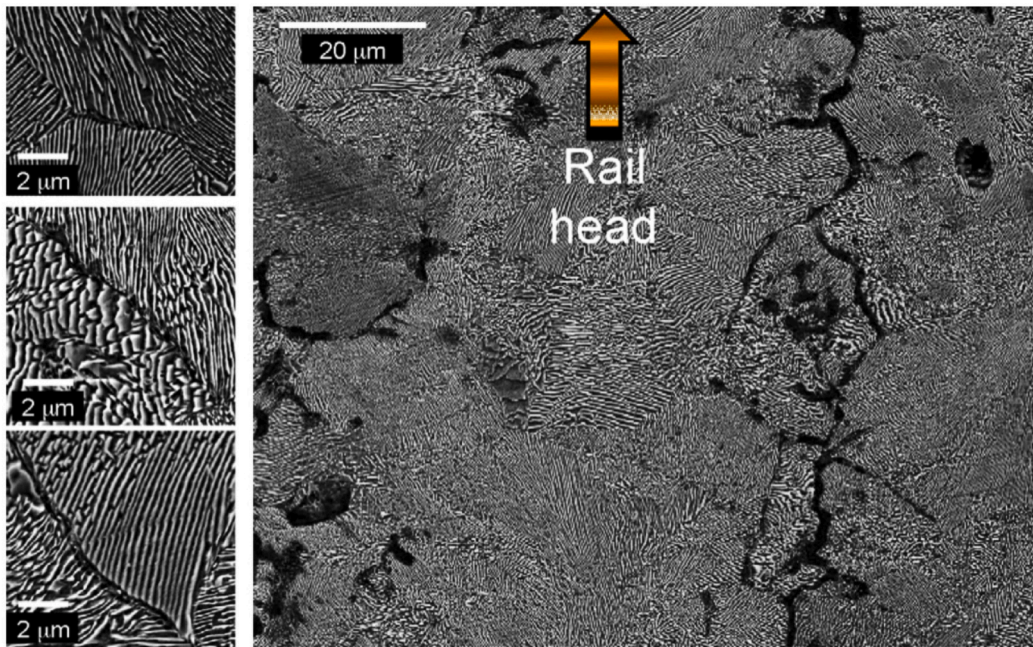


Fig. 49. Intergranular rolling contact fatigue cracking along prior austenite grain boundaries due to the presence of pro-eutectoid cementite. Reproduced from [342] with permission of Elsevier.

time for crack initiation if the wear rate is so low so that cracks are not worn away [408]. RCF cracks can begin at the prior austenite grain boundaries and then propagate intergranularly to a depth greater than the plastically deformed layers, suggesting that the toughness at grain boundaries is important. This study was performed using cast bainitic grades intended for back-up rolls in hot rolling mills.

In a study that characterised the microstructure of thirteen different premium rails from a variety of manufacturers, over a period of five years, and numerically modelled the influence of microstructural features on mechanical performance, it was found that a smaller austenite grain size (\bar{L}_v) has a lesser effect in improving the yield strength and rolling contact fatigue resistance than solid solution strengthening, pearlite colony size and interlamellar spacing [342]. In fact, it was not \bar{L}_v but the presence of pro-eutectoid cementite ($V_v^0 \approx 0.05$) along prior austenite grain boundaries, as seen in Fig. 49, that was most detrimental to RCF performance, fracture toughness, elongation and wear resistance. Lowering the carbon concentration whilst keeping a slow cooling rate or increasing the cooling rate from the hot-deformation temperature, as done for bearing steels [420], can suppress pro-eutectoid cementite with the excess carbon leading to a greater fraction of cementite within the pearlite. If the pro-eutectoid cementite does form, one option is to spheroidise the cementite at temperatures ranging from $\sim 600\text{--}700^\circ\text{C}$, in the case of plain eutectoid steels. Such process can be accelerated by applying concurrent deformation, since the vacancy generation that aids lamellar fragmentation, rounding off, and coarsening was shown to be proportional to the applied strain rate [421] – but this may not in practice correspond to the

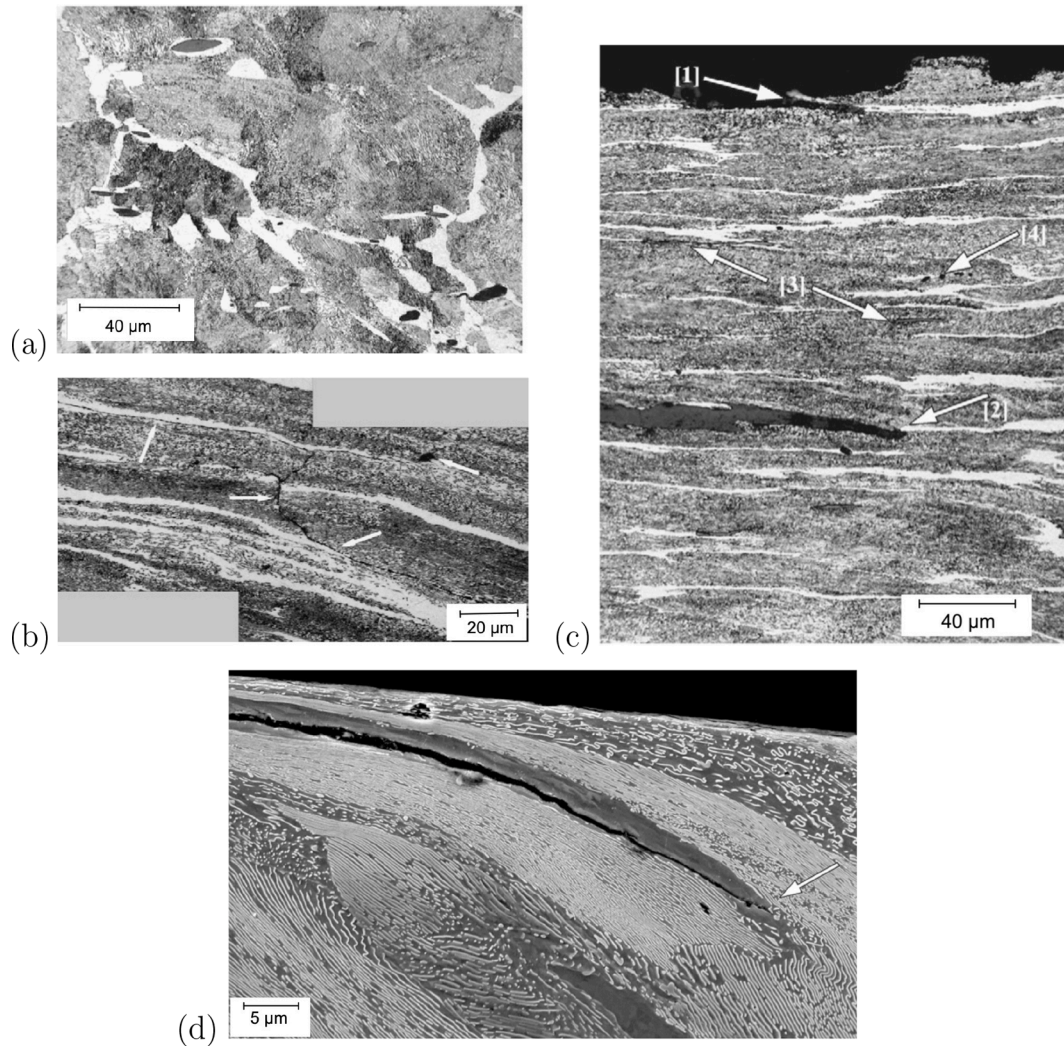


Fig. 50. Micrographs of pro-eutectoid ferrite in: a) untested rail sample, b) sample tested with a twin disc machine at 1500 MPa and 1% slippage after 14013 cycles showing crack propagation along flattened pro-eutectoid ferrite regions, c) rail sample after 33 years of service exhibiting (1) surface crack initiation at a pro-eutectoid ferrite band, (2) oxide filled RCF crack propagating along a ferrite band, (3) cracks propagating along flattened MnS inclusions, and (4) cracks at fine angular brittle inclusions; and d) detail of surface crack initiation at pro-eutectoid containing prior austenite grain boundaries and stifling when it reaches the pearlite front. Reproduced with the permission of Elsevier [361,423].

microstructure needed.

These studies suggest that it is not \bar{L}_y itself but embrittlement due to pro-eutectoid cementite formation that adversely affects rolling contact fatigue life in rails. As an illustration, the negative influence of carbide networks at prior austenite grain boundaries that can reduce the rolling contact fatigue life to half compared to spheroidised samples has been known for many years in the bearing steel industry [422].

In the absence of pro-eutectoid cementite or severely flattened ductile MnS inclusions just below the surface, RCF cracks have been observed to originate along strained prior austenite grain boundaries and not propagate beyond the length of a single grain (50 μm in R220), at least until 55% of the ‘average RCF life’, based on numerous twin disc tests in which failure in the form of flake cracks was monitored through an eddy current twin probe. The crack is stifled when it reaches a less favourably aligned grain boundary [423]. It was concluded therefore, that the first half of the average RCF life is influenced by the microstructure, whereas the second half which is driven by strain fields that propagate the crack to a length several times \bar{L}_y and can make neighbouring stifled cracks join up or ‘jump’ across thinned pearlite zones in order to comply with the strain, sometimes with the help of bridging inclusions, Fig. 50b [423,424]. In fact, the size and shape of surface flakes was related to the dimensions of favourably aligned prior austenite grains of the surface after a series of compression and unidirectional tractive stresses, Fig. 51. A somewhat similar observation was made by authors studying mixed ferrite-pearlite microstructures who concluded that crack growth is dominated by the applied stress system and only influenced to a lesser extent by microstructural features since cracks not always propagated along the softer ferrite on the boundaries [75].

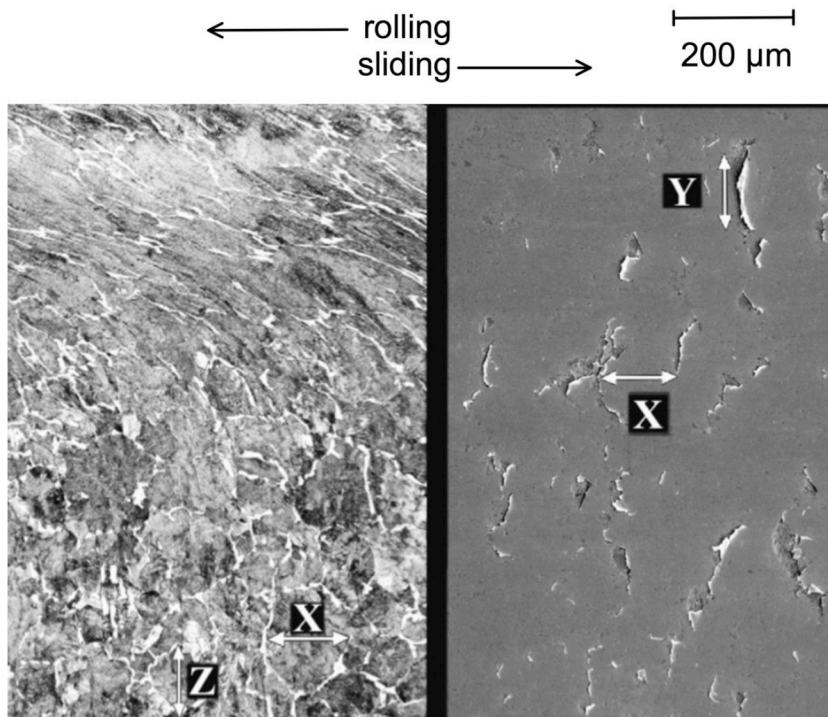


Fig. 51. Optical image of the cross section and SEM image of the surface of R220 at 45% of its RCF life, displaying a relationship between the early crack flake size and the prior austenite grain size. The X, Y and Z correspond to the circumferential/horizontal direction, the horizontal/track width direction and the vertical direction normal to the surface, respectively. Reproduced from [423] with permission of Elsevier.

Crack propagation in pearlite can occur in a cleavage fracture mode defined in terms of the fracture stress σ_f , which is that required to initiate unstable fracture at a finite location, which was shown to be independent of \bar{L}_y , but increase with smaller interlamellar spacings [153,425]. With regards to the tensile strength of pearlite, it sometimes is claimed to be independent of \bar{L}_y [153] and at other times proportional to \bar{L}_y for a given interlamellar spacing [293]. However, \bar{L}_y is a coarse microstructural feature when compared with interlamellar spacing, so it may not have a determining influence on strength. Instead, the tensile ductility δ , which is the strain necessary to develop a critical-sized microcrack and to propagate it in an unstable cleavage mode, seems to decrease significantly with increasing austenite grain size [153,293]. Nevertheless, such property is not precisely relevant in rolling contact fatigue but more in the case of bending forming processes, for example, where the material initially is crack-free. In the case of the plane strain fracture toughness³⁰ K_{Ic} is independent of \bar{L}_y since the fracture plastic zone is much smaller [153]. However, the Charpy impact toughness is inversely related to \bar{L}_y since fracture occurs at regions of common crystallographic orientation called cleavage facets or nodules so having more of them in a fine grained austenite would provide more resistance to crack propagation [426,300,427]. Another property that seems to have an inverse relationship with \bar{L}_y is the fatigue crack growth rate [428]. During RCF it is likely that cracks propagate along embrittled grain boundaries as shown in Fig. 49 than in a cleavage (pure tension) mode since longitudinal wheel-rail contact is after all a sequence of tension, shear and compression.

Proeutectoid ferrite at the austenite grain boundaries can accelerate RCF failure, either by aiding crack initiation or providing an easy path for propagation, Fig. 50 [361,221,423]. The ferrite is soft so plastic strain within it is exaggerated [429,430,423]. This allows the nucleation of short surface cracks that propagate along the direction of plastic flow and the pro-eutectoid ferrite bands Fig. 39a. These cracks grow until they hit a pearlitic front or if the pro-eutectoid ferrite extends along a path that is not the most favourable for crack growth [423]. The amount of strain hardening of the ferrite depends on its size, shape, and orientation with respect to the straining direction [221]. When the volume percentage of pro-eutectoid ferrite was reduced from 5.8 to 2 wt% by cooling rapidly from the austenitisation temperature, surface cracks instead originated at inclusions [431]. In no cases, either with high³¹ or low amounts of pro-eutectoid ferrite³², were cracks seen to nucleate at the subsurface, most likely due to the plastic deformation and compressive

³⁰ Macroscopic criterion for the unstable propagation of a pre-existing crack in an elastically loaded sample [153]. According to Pointner, K_{Ic} cannot be used to estimate RCF crack growth rates, since it describes only high cyclic stress intensity factors valid for long cracks (>few mm) [272].

³¹ 11 wt%; this content was maximised by cooling down slowly (4 h) from the austenitisation temperature to 610 °C. The amount of this phase was quantified through image analysis.

³² Rapidly cooled from the austenitising temperature to room temperature in 0.5 h

residual stresses introduced during cyclic loading [361]. The modelling of weakening due to the ferrite indicates that the observation of enhanced RCF when the ferrite thickness is reduced could be explained if the pearlite then constrains it from excess strain [221].

6.8. Inclusions

We have seen that pro-eutectoid ferrite can be responsible for the initiation of cracks at the surface, whilst pro-eutectoid cementite networks can provide a path for the propagation of cracks deep into the rail. In the absence of proeutectoid phases, strain flattened MnS and other inclusions sometimes become prominent initiators of RCF cracks [361]. Earlier work indicated that the role of MnS was especially important at high contact stresses and creepages, and that hard oxide inclusions also contributed to crack initiation [50]. These experiments were stopped as soon as an eddy current probe detected a crack, so the possibility of MnS inclusions or primary ferrite initiating cracks later in the process cannot be categorically excluded [432].

The manganese sulphides in particular can occur in clusters often described as strings of defects, which under loading during track service can lead to the formation of highly affected regions between individual defects with large strain gradients. The effect is magnified if there happen to be instances of overloads [433,434]. The overloads can arise, for example, from structural vibrations on bridges [435], high train-speed leading to dynamic overloads [436], or compromised vertical stiffness due to ballasting [437].

Non-metallic inclusions can be detected and quantified through different methods depending on the scale and resolution such as local X-ray spectrometry, metallography and automated image analysis, or fractional gas analysis that measures the evolution of oxygen during linear heating of the samples. Regarding the nature of inclusions, observations show that alumina inclusions are more detrimental to RCF than silica or calcium oxide [194]; the Mohs' hardness of alumina, silica and calcium oxide are 9, 6–7 and 3 respectively.

The general perception is that inclusions will be most damaging in fatigue rather than wear. However, parameters such as volume fraction, size, elongation, orientation, elastic modulus relative to the matrix, bonding strength etc. must be taken into account. It has been shown that the fatigue limit³³ is only affected by the inclusion content when stringer inclusions (sulphides) are oriented parallel to the stress axis, but not when they are aligned perpendicularly [438,439,406]. During bend tests on four different pearlitic steels, the fatigue limit was particularly reduced by elongated or brittle inclusions rather than by their average size or the interlamellar spacing of the pearlite [406]. In other words, the steel with longest, more brittle inclusions (spheroidal alumina silicates) had a lower fatigue limit despite having a similar inclusion distribution and the finest interlamellar spacing of the samples studied (120 nm) [433]. This is in spite of the fact that interlamellar spacing is inversely proportional to yield strength and yield strength is linearly related to the fatigue limit [298,440]. The three types of crack initiation mechanisms observed in that study, i.e., microcrack initiation, interfacial debonding, or inclusion fracture, highlight the complexity of the problem [406,441].

6.9. Carbon concentration

The explanation for why the contact fatigue limit in general increases with the carbon concentration of the steel is simple, that the steel becomes stronger, Fig. 47c. Interstitial solid solution strengthening of ferrite by carbon is more potent than precipitate hardening through cementite. Low-carbon martensite performs worse than pearlite of similar hardnesses during rolling contact fatigue [442], as illustrated in Fig. 47d. With a martensitic microstructure, it may be difficult to retain the carbon in solution over the service life [433], an effect well established in bearing steel [37]. The pearlite structure is in this sense much more stable than that of untempered martensite.

The loss of carbon from the surface regions during heat treatment (decarburisation) creates a layer of ferrite on the rails, which causes an increase of the rate of shear strain accumulation below the surface (~225 µm deep), an increase of hardening rate, and almost doubles the RCF crack growth rates due to the low hardness of ferrite [75]. The RCF cracks were initiated at the ferrite/pearlite interface due to ductility exhaustion from the high contact stresses arising from asperity contact. However, since the depth of the decarburised layer in real rails (0.5 mm) does not coincide with that from the maximum subsurface shear stresses (2 mm) [280,221] and the ferrite strain hardens during rolling contact bringing down the crack growth rate to normal levels (55 nm cycle⁻¹) after the initial cycles, it is likely that the contribution of decarburisation to RCF, at least on the wheel tread and railhead, is minimal and unlikely to have a long-term effect [75].

6.10. White-etching layers

The description “white-etching layer” (WEL) comes from the fact that the structure within is so fine that it is attacked relatively mildly by etchants when compared with the coarser, ordinary structure of rail, Fig. 52a. The very first high-resolution study of the structure of WEL [443] revealed a highly deformed ferrite structure containing carbon in solution (e.g., Fig. 52b), with evidence that the material in the layer was not a consequence of re-austenitisation followed by quenching by the bulk substrate to generate martensite. Other results confirm this general conclusion. For example, the WEL is obtained after multiple traverses of the train to accumulate the deformation, whereas the heating would be apparent after a single traverse [444].

However, not everyone agrees with this, largely because martensite-like structures have been observed in the WEL [445] or because

³³ Fatigue limit defined in this case as the maximum possible stress so samples reach 10⁷ cycles without crack initiation, as detected through acoustic emission.

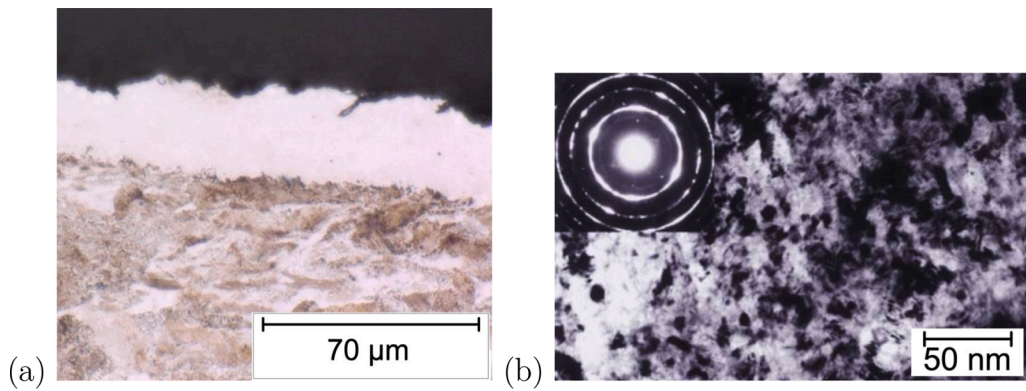


Fig. 52. (a) White-etching layer on R260Mn rail that had been in service between 1989–2007 on straight track. Reproduced and adapted from [448] under CC BY 4.0 license. (b) Nanostructured carbon-supersaturated ferrite in white-etching region of a eutectoid steel rail that served for two years on a 5° curve with an accumulated tonnage of 271 MGt. The inset shows an electron diffraction ring-pattern showing a large range of grain orientations typical of such structures. Reproduced from [444] with the permission of Elsevier.

simulations relying on dynamic friction coefficients indicate that a temperature might be reached to induce austenite formation [313,446]. White-etching layers also form during rail-grinding operations where there is likely to be substantial localised heating [447], where the thickness, distribution and length of the WEL's has been shown to depend on the grade of the rail that is ground. The thickness is found to decrease substantially in the order R260, R350HT and R400HT, from 15 μm, 11 μm and 7 μm respectively although the hardness of the layer is similar in all cases, in excess of 1000 HV. The surface temperatures reached have been estimated to be well into the austenite phase field for all three rails.

It is possible that both types of explanations of white-etching layers are reasonable, depending on the details of the loading on the rails.

The relatively soft (650 HV) white-etching layer formed at the top of low carbon steels (0.45 wt%) seems not to affect the rolling contact fatigue properties but harder (1000 HV) layers that are associated with higher carbon steels can reduce the RCF life by 30% [194]. This is because of the larger gradient of material properties that cause the layer to crack at its interface with the matrix; in some cases the flaking is so ubiquitous that the WEL was completely eliminated.

The strengthening due to a higher carbon concentration will on the one hand increase the rolling contact fatigue resistance, Fig. 47d, but on the other hand, increase the sensitivity of the steel to develop hard -and damaging- white-etching layers [194]. This result matches what has been observed in bearing steels, where a quenched and tempered 1C-1.5Cr wt% steel (52100) readily developed hard white-etching matter around cracks due to the rubbing action of their surfaces during cyclic loading that refines the structure and enriches it with carbon via the dissolution of carbides [449]. No such structure was observed in a lower carbon (0.8 wt%) carbide-free nanostructured bainitic steel tested under the same conditions of Hertzian pressure and cycles, mainly due to the lack of carbides to go into solution [450]. If the white-etching matter forms in such a steel, then its hardness would be attributed to just the refined size of the ferrite but not to carbon enrichment, suggesting that as in the case of the rail study presented above, this low hardness of the white matter would have a lesser effect on the rolling contact fatigue life [451].

6.11. Environmental factors

One of the main interpretations of the effect of water on the RCF behaviour of rails is that it enters relatively benign cracks and under the influence of rolling contact, act as an high-pressure wedge that dramatically raises the stress at the crack tip, causing it to advance deeper than the deformation affected steel at the surface. The pressure pulses create tensile stresses at the crack front, or the reduction of crack-face friction allows a shear mode crack growth [398]. A similar phenomenon can be observed in bearings where surface breaking cracks fill up with lubricant, which transmits the contact load to the crack tip [278]. Full-scale rails that had been subjected to traffic, were removed into a test facility where they were exposed to further traffic while covered with water-based marker fluid [216]. The experiments provided excellent evidence of fluid penetration into the cracks.

There is a review focusing on the role of moisture, on the development of cracks that are initiated on rails by rolling-contact fatigue [452]; useful comparisons were made against rolling contact fatigue phenomena in bearings.

It is interesting that no signs of RCF were observed in rails tested dry or unlubricated, but occurred readily in the presence of lubricants, such as water or grease, were later applied [453,198]. This is consistent with the appearance of pitting cracks appeared after lubricant was added to a dry test on bearing steel [356]. There appear to be three further mechanisms by which water can affect the development of fatigue damage on rails [452]:

1. if the water acts as a lubricant, there will be a reduction in the wear rate of the rail. This may in turn cause the persistence of surface-initiated fatigue cracks which otherwise would be worn away. These cracks could then grow to sizes that are intolerable.
2. If water causes a decrease in adhesion, resulting in increased creepage, then the damage rate would increase.

3. The water participates in electrochemical reactions that lead to crack branching akin to stress-corrosion cracks. The reactions would also introduce nascent hydrogen in the steel, which is well known to cause embrittlement. In bearings, the formation of white-etching matter is greatly accelerated if the steel is charged with hydrogen [37]. Minute traces of water in the lubricant used in bearings [454,455], just 100ppmw of water dissolved in organic lubricant is detrimental. The water condenses from solution within the oil, in surface microcracks and in this way becomes a potent supplier of corrosion-induced hydrogen at the crack tips [456]. Water created through chemical reactions [457], or exposure to hydrogen sources through other corrosion reactions, can lead to a reduction in bearing life. It has long been known that operating bearings in a hydrogen atmosphere leads to hydrogen embrittlement and extensive surface pitting and flaking [458]. Indeed, hydrogen present in the atmosphere around a ball bearing can be mechanically squeezed into the steel [459]. Hydrogen sulphide (H_2S) has a similar effect to hydrogen because it inhibits the recombination of hydrogen atoms at the metal surface [460].

It is emphasised that the hydrogen embrittlement of rails is not in general a feature that controls the life or fabrication of rail steels. Academic studies in which the rail steels are electrolytically charged with hydrogen, not surprisingly, exhibit embrittlement as would most steels [30]. But reports of hydrogen-induced failures of modern rails are difficult to find.

Experiments have been reported on the use of dry, solid lubricants applied by rubbing against the railway wheel [461]. The "solid friction-modifier" is made by compacting polytetrafluoroethylene, molybdenum disulphide, talcum powder, all three are well-known lubricants, together with carbon fibre, presumably acting as a binder. However, this does not seem to be a practical solution if a train has to move over differently inclined terrains, and because the retention of the lubricant on the wheel lasts for a limited time especially when slippage occurs.

The effect of temperature on rolling-contact fatigue damage is defined with respect to a neutral temperature T_N , at which the rail is neither in tension or compression. Deviations from this makes the stress within the rail go into compression when $T < T_N$ and vice versa. Therefore, damage intensifies at low temperatures but has no significant effect for $T > T_N$ because any crack faces created are then compressed together due to rail thermal-expansion [7].

7. Machine learning of rail steels

Machine learning is a powerful empirical method for the quantitative interpretation of complex data, with arbitrary non-linearity [e.g., 462,392]. But in the context of rails steel metallurgy, which is the topic of this review, there are two important caveats:

- The method relies entirely on the availability of data that include all of the important variables.
- It requires a sufficient quantity of data, the sufficiency determined by the magnitude of the modelling uncertainty which will not be constant in the data domain. The modelling uncertainty arises because many different models can be fitted adequately to sparse data, each of which behaves differently when extrapolated or interpolated.
- A model needs to be assessed to see if it reveals new phenomena. It is not good to assess its utility by comparing against data used to train it, because the networks are sufficiently flexible to model any dataset. It is the behaviour in extrapolation that matters.

A case in hand is a model based on limited inputs (hardness of rail and wheel, C, Mn, Si, Cr, V, pearlite interlamellar spacing) which led to such great uncertainties when testing the effect of silicon concentration that it is impossible to extract useful information, Fig. 53 [463]. In another study, it is claimed that the machine learning on rail steel wear is validated against laboratory data but only on the data used to create the model [464].

The conclusion has to be that a long-term data collection exercise that includes an array of assessed input variables and a variety of outputs would reap benefits to machine learning models capable of creating new technologies.

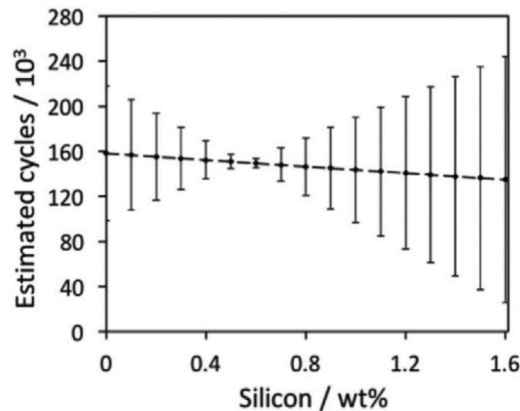


Fig. 53. Estimates of the rolling contact fatigue life as a function of the silicon concentration of a rail steel. The uncertainties come from a Bayesian interpretation of modelling uncertainty, so a large uncertainty indicates a lack of adequate interpretable information [463].

8. Summary

Steels in general offer a very wide range of mechanical properties and at the same time can be manufactured on a large scale at a reasonable cost. Steels for rails are no exception – it has routinely been possible to manufacture rails with hardness in the range 260–400 HV to provide an optimum combination of wear and fatigue resistance that is appropriate for particular track configurations. Rolling-contact fatigue and wear are the predominant factors in determining the maintenance-schedules and the useful life of rails.

The majority of rail steels have a fully-pearlitic microstructure, the interlamellar spacing of which can be manipulated to control the final properties. This ‘manipulation’ relies on the cooling conditions from the austenitic state, with a secondary role played by the substitutional solute content of the steel. The metallurgy of pearlite is well-understood and has been applied thoroughly to rail steels, with some exceptions. For example, there have been no attempts to introduce pearlite that is strengthened by fine, interphase precipitation of both the cementite and ferritic phases [465,466]. Copper also can precipitate in pearlite [467], although the role of copper in the context of possible problems during hot-processing would need to be looked at in detail. The use of thermomechanical control processing has not been explored much as a tool to achieve fine microstructures with only one study focusing on getting the austenite grain structure in a rail steel into a pancaked shape prior to its transformation into pearlite as a means to obtaining a finer ultimate microstructure [321] and another using it to achieve very fine pearlite for high wear resistance, but neither the role of microalloying additions nor the state of the austenite prior to the pearlite transformation are explained [294].

In contrast, bainitic steels, particularly the carbide-free bainitic steels, have had limited applications, presumably because those based on pearlite serve the industry rather well. However, there is no doubt that they exhibit superior rolling contact fatigue resistance. One problem, for which there is a dearth of published data, is that flash butt welding results in a region within the heat-affected zone where the retained austenite may decompose, the consequences of which are not documented.

In terms of welding, both using the thermit process and friction butt welding, it is the production of a soft zone within the microstructure in the heat-affected zone (whether that microstructure is pearlitic or bainitic) that seems to cause concern, especially if the zone is wide. There are preliminary academic studies on the laser welding of rails, with the aim of reducing the total heat input and hence inducing a narrow heat-affected zone; however, the cooling rates associated with the process can result in transformation into martensite, so some form of preheating may be necessary [162].

Declaration of Competing Interest

The authors declare that they have no known competing financial interests or personal relationships that could have appeared to influence the work reported in this paper.

Data availability

Data will be made available on request.

Acknowledgements

Several productive discussions with Jai Jaiswal of ARR Rail Solutions Limited, and Peter Mutton of the Monash University, Institute of Railway Technology are gratefully acknowledged. Their direct experience of the rail industry matters a lot in deciding what is important and in need of attention.

References

- [1] Ishizaka K, Lewis SR, Lewis R. The low adhesion problem due to leaf contamination in the wheel/rail contact: Bonding and low adhesion mechanisms. *Wear* 2017;378:183–97.
- [2] Garnham J, Davis C. Rail materials. In: *Wheel-rail interface handbook*. Elsevier; 2009. p. 125–71.
- [3] Bhadeshia HKDH. Steels for rails. In: *Encyclopedia of Materials Science*, Pergamon Press, Oxford, Elsevier Science; 2007. p. 1–7.
- [4] Porfir'ev MA, Ivanov YF, Popova NA, Gromov VE, Shlyarova YA. Strain hardening of rail steel. *Russ Metall (Metally)* 2023;2023:485–91.
- [5] Athukorala AC, De Pellegrin DV, Kourousis KI. Characterisation of head-hardened rail steel in terms of cyclic plasticity response and microstructure for improved material modelling. *Wear* 2016;366:416–24.
- [6] Clayton P. Predicting the wear of rails on curves from laboratory data. *Wear* 1995;181:11–9.
- [7] Ghodrati M, Ahmadian M, Mirzaeifar R. Modeling of rolling contact fatigue in rails at the microstructural level. *Wear* 2018;406:205–17.
- [8] Xu W, Zhang B, Deng Y, Wang Z, Jiang Q, Yang L, Zhang J. Corrosion of rail tracks and their protection. *Corros Rev* 2021;39:1–13.
- [9] Schafer DH, Barkan CP. A prediction model for broken rails and an analysis of their economic impact; 2008. <https://api.semanticscholar.org/CorpusID:2909025>.
- [10] Devanathan R, Clayton P. Rolling-sliding wear of three bainitic steels. *Wear* 1991;151:255–67.
- [11] Bauri LF, Alves LH, Pereira HB, Tschiptschin AP, Goldenstein H. The role of welding parameters on the control of the microstructure and mechanical properties of rails welded using fbw. *J Mater Res Technol* 2020;9:8058–73.
- [12] Babachenko OI, Kononenko HA, Podolskiy RV, Safronova OA. Steel for railroad rails with improved operating properties. *Mater Sci* 2021;56:814–9.
- [13] Wood N. A Practical Treatise on Rail-roads, and Interior Communication in General. London U.K.: Longman, Orme, Brown, Green, & Longmans; 1838. 3rd Edition.
- [14] Smith RA. Hatfield memorial lecture 2007 railways and materials: synergetic progress. *Ironmaking Steelmaking* 2008;35:505–13.
- [15] Brooke D. The advent of the steel rail, 1857–1914. *J Transp History* 1986;7:18–31.
- [16] Walsh WJ. The history of steel railway rails, Bachelor of Science thesis. University of Illinois; 1909.
- [17] Osborn FM. The story of the Mushets. Thomas Nelson and Sons Ltd; 1952.

- [18] Jaiswal J. Designing rail composition based on the understanding of rail degradation mechanisms, Tech. rep., Corus Rail, Track Engineering and Technologies; 2015.
- [19] Solano-Alvarez W, Peet MJ, Pickering EJ, Jaiswal J, Bevan A, Bhadeshia HKDH. Synchrotron and neural network analysis of the influence of composition and heat treatment on the rolling contact fatigue of hypereutectoid pearlitic steels. *Mater Sci Eng A* 2017;707:259–69.
- [20] Solano-Alvarez W, Gonzalez LF, Bhadeshia HKDH. The effect of vanadium alloying on the wear resistance of pearlitic rails. *Wear* 2019;436–437:203004.
- [21] Yates JK. Innovation in rail steel. *Sci Parliament* 1996;53:2–3.
- [22] Chard AE. Deformation of inclusions in rail steel due to rolling contact. Ph.D. thesis. Birmingham, U.K.: University of Birmingham; 2012.
- [23] Garnham J, Ding R-G, Davis C. Ductile inclusions in rail, subject to compressive rolling–sliding contact. *Wear* 2010;269:733–46.
- [24] Song P, Li Y, Ren Q, Ren Y, Zhang L. Effect of Al_2O_3 content in inclusions on the precipitation of MnS during cooling of a heavy rail steel. *Metall Mater Trans B* 2023;54:1–15.
- [25] Dudley CB. The chemical composition and physical properties of steel rails. *J Franklin Inst* 1878;106:361–90.
- [26] Chang LC. Bainite transformation and novel bainitic rail steels (https://www.phase-trans.msm.cam.ac.uk/2012/chang_thesis.pdf). Cambridge, U.K: University of Cambridge; 1995. Ph.D. thesis.
- [27] Johnson WH. On some remarkable changes produced in iron and steel by the action of hydrogen and acids. *Proc Roy Soc London* 1875;23:168–79.
- [28] Bhadeshia HKDH. Prevention of hydrogen embrittlement in steels. *ISIJ Int* 2016;56:24–36.
- [29] Knupp GG, Chidley WH, Glove JL, Hartman HH, Morris GF, Taylor CW. A review of the manufacture, processing, and use of rail steels in north america—a report of aisi technical subcommittee on rails and accessories, in. In: *Rail Steels—developments, Processing, and Use: A Symposium*, Vol. 644. ASTM International; 1976. p. 7.
- [30] Moon AP, Balasubramaniam R, Panda B. Hydrogen embrittlement of microalloyed rail steels. *Mater Sci Eng A* 2010;527:3259–63.
- [31] Stock R, Pippin R. RCF and wear in theory and practice – the influence of rail grade on wear and RCF. *Wear* 2011;271:125–33.
- [32] Pumpyanskiy DA, Tyutuunik SV, Kolokolov KA, Mescheryachenko AA, Murzin IS, Emel'yanov VV, Belonozhko SS, Arsenkin AM. Production of high-quality wheel steel. Part 2. Nonmetallic inclusion composition and morphology. *Metallurgist* 2021;65:153–9.
- [33] Wang Y, Zhang Y, Zhang L, Liu N, Ren Y. Effect of total calcium in heavy rail steels on the transformation of inclusions during heat treatment at 1473 K. *Steel Res Int* 2021;92:200605.
- [34] Liu N, Zhang L, Chu Y, Ren Y. Effect of slag basicity on non-metallic inclusions in a heavy rail steel. In: *Symposium on high-temperature metallurgical processing*. Berlin, Germany: Springer/TMS; 2022. p. 513–20.
- [35] Jerebtsov D, Mikhailov G. Phase diagram of $CaO-Al_2O_3$ system. *Ceram Int* 2001;27:25–8.
- [36] Koh SU, Jung HG, Kang KB. Effect of non-metallic inclusions and hot rolling process parameters on hydrogen induced cracking of linepipe steels. *Korean J Metals Mater* 2008;46(4):257–66.
- [37] Bhadeshia HKDH. Steels for bearings. *Prog Mater Sci* 2012;57:268–435.
- [38] Cramb AW. *Impurities in Engineering Materials: impact, reliability and control*, Marcel Dekker AG, Basel, Switzerland (ed. C.L. Briant); 1999.
- [39] Liu Y, Wu W, Liu L, Liu M, Li Y. Thermodynamics behavior of titanium for BOF smelting bearing steel. *J Iron Steel Res, Int* 2006;13:74–8.
- [40] Bauri LF, Alves L, Pereira HB, Tschiptschin AP, Goldenstein H. The role of welding parameters on the control of the microstructure and mechanical properties of rails welded using fbw. *J Mater Res Technol* 2020;9:8058–73.
- [41] Grigor'ev AM, Kuznetsov MS, Shepelev DS, Alekseev EM, Grigorovich KV. Optimization of the continuous rail steel casting technology aiming to improve non-metallic inclusion cleanliness. *Steels Transl* 2021;51:302–7.
- [42] Micheletto A, Cookson J, Pang Y, Chen B, Mutton P. The structural integrity of flash-butt welded premium rail steel – evaluation of strength, microstructure and defects. *Proc Inst Mech Eng, Part F: J Rail Rapid Transit* 2021;235:1006–12.
- [43] Kabo E, Ekberg A, Maglio M. Rolling contact fatigue assessment of repair rail welds. *Wear* 2019;436–437:203030.
- [44] Korpanec I, Rebeyrotte E, Guigon M, Tordai L. Increasing axle load in Europe: state of the art and perspectives. In: *Proceedings of 8th International Heavy Haul Conference, International Heavy Haul Association, Companhia Vale do Rio Doce, Rio de Janeiro, Brazil; 2005*. p. 227–235.
- [45] Girsch G, Keichel J, Gehrmann R, Zlatnik A, Frank N. Advanced rail steels for heavy haul application – track performance and weldability. In: *Proceedings of the Ninth International Heavy Haul Conference, 2009, Shanghai, International Heavy Haul Association, China Railway Publishing House, Beijing, China; 2009*. p. 171–179.
- [46] Board II. Train derailment at hatfield: A final report, Tech. rep., Office of Rail and Road, London, UK; 2006.
- [47] Jack I. *The crash that stopped Britain*. London, U.K.: Granta Books; 2001.
- [48] Zhang X, Zhang L, Yang W, Dong Y. Characterization of mns particles in heavy railsteels using different methods. *Steel Res Int* 2016;88:1600080.
- [49] Smallwood R, Sinclair JC, Sawley KJ. An optimization technique to minimize rail contact stresses. *Wear* 1991;144:373–84.
- [50] Beynon JH, Garnham JE, Sawley KJ. Rolling contact fatigue of three pearlitic rail steels. *Wear* 1996;192:94–111.
- [51] Dudley CB. Does the wearing power of steel rails increase with the hardness of the steel? *J Franklin Inst* 1879;107:10–3.
- [52] Perez-Unzueta AJ, Beynon JH. Microstructure and wear resistance of pearlitic rail steels. *Wear* 1993;162–163:173–82.
- [53] Ueda M, Matsuda K. Effects of carbon content and hardness on rolling contact fatigue resistance in heavily loaded pearlitic rail steels. *Wear* 2020;444:203120.
- [54] Heyder R, Girsch G. Testing of HSH® rails in high-speed tracks to minimise rail damage. *Wear* 2005;258:1014–21.
- [55] Dhua S, Ray A, Sen S, Prasad M, Mishra K, Jha S. Influence of nonmetallic inclusion characteristics on the mechanical properties of rail steel. *J Mater Eng Perform* 2000;9:700–9.
- [56] Khourshid A, Gan Y, Aglan H. Microstructure origin of strength and toughness of a premium rail steel. *J Mater Eng Perform* 2001;10:331–6.
- [57] Yu F, Jar PYB, Hendry MT, Jar C, Nishanth K. Fracture toughness estimation for high-strength rail steels using indentation test. *Eng Fract Mech* 2018;204:469–81.
- [58] Ochi Y, McEvily A. An evaluation of the fatigue crack growth and fracture toughness characteristics of rail steels. *Eng Fract Mech* 1988;29:159–72.
- [59] L.P. Moreira, T.G. Viana, L.B. Godefroid, G.L. de Faria, L.C. Cândido, Effect of microstructure on fracture toughness and fatigue crack growth resistance of pearlitic steels for railroad application. In: *Proceedings of 23rd ABCM International Congress of Mechanical Engineering, ABCM, Rio de Janeiro, Brazil; 2015*. p. 1–8.
- [60] Sajuri Z, Alang NA, Razak NAA, Aziman M. Fracture toughness and fatigue crack growth behavior of rail track material. *Key Eng Mater* 2011;462:1109–14.
- [61] Seo JW, Kwon SJ, Jun HK, Lee DH. Evaluation of fatigue and fracture characteristics of high-speed rail material, *Journal of the Korean Society for. Precis Eng* 2017;34:861–6.
- [62] Aglan HA, Fateh M. Fatigue crack growth and fracture behavior of bainitic rail steels. *J Mech Mater Struct* 2007;2:335–46.
- [63] Bhadeshia HKDH. *Pearlite in steels*. Florida, USA: Taylor & Francis (CRC Press, Routledge); 2024. ISBN 978-1-032-61392-9.
- [64] Jaiswal J. Private communication to H.K.D.H. Bhadeshia, elongation in rails; February 2024.
- [65] Bandula-Heva T, Dhanasekar M. Failure of discontinuous railhead edges due to plastic strain accumulation. *Eng Fail Anal* 2014;44:110–24.
- [66] Boonsukachote P, Kingklang S, Uthaisangsuk V. Modelling of mechanical properties of pearlitic rail steel. *Key Eng Mater* 2019;798:3–8.
- [67] Liu P, Quan Y, Ding G. Dynamic mechanical characteristics and constitutive modeling of rail steel over a wide range of temperatures and strain rates. *Adv Mater Sci Eng* 2019;2019:6862391.
- [68] Iwafuchi K, Satoh Y, Toi Y, Hirose S. Fatigue property analysis of rail steel based on damage mechanics. *Quart Rep RTRI* 2004;45:203–9.
- [69] Kapoor A, Beynon JH, Fletcher D, Loo-Morrey M. Computer simulation of strain accumulation and hardening for pearlitic rail steel undergoing repeated contact, *The. J Strain Anal Eng Des* 2004;39:383–96.
- [70] Panda B, Balasubramaniam R, Moon A. Microstructure and mechanical properties of novel rail steels. *Mater Sci Technol* 2009;25:1375–82.
- [71] Lan Y, Zhao G, Xu Y, Ye C, Zhang S. Effects of quenching temperature and cooling rate on the microstructure and mechanical properties of U75V rail steel. *Metallogr Microstruct, Anal* 2019;8:249–55.
- [72] Scutti J, Pelloux R, Fuquen-Moleno R. Fatigue behavior of a rail steel. *Fatigue & Fract Eng Mater Struct* 1984;7:121–35.

- [73] Yu F, Jar P-YB, Hendry M. Effect of temperature on deformation and fracture behaviour of high strength rail steel. *Eng Fract Mech* 2015;146:41–55.
- [74] Aglan H, Gan Y. Fatigue crack growth analysis of a premium rail steel. *J Mater Sci* 2001;36:389–97.
- [75] Carroll RI, Beynon JH. Decarburisation and rolling contact fatigue of a rail steel. *Wear* 2006;260:523–37.
- [76] Cui L, Lei X, Zhang L, Yang W, Gao Y, Liu Y, Liu N. Three-dimensional characterization of defects in continuous casting blooms of heavy rail steel using X-ray computed tomography. *Metall Mater Trans A* 2021;52:2327–40.
- [77] Srimani SL, Basu J. An investigation for control of residual stress in roller-straightened rails. *J Strain Anal* 2003;38:261–8.
- [78] Chen L, Yang M, Xu Y, Zhang Z, Li Z, Zhang F. Effects of cooling on bending process of heavy rail steel after hot rolling. *Metallorg, Microstruct, Anal* 2016;5: 196–206.
- [79] Ringsberg JW, Lindbäck T. Rolling contact fatigue analysis of rails including numerical simulations of the rail manufacturing process and repeated wheel-rail contact loads. *Int J Fatigue* 2003;25:547–58.
- [80] Kang C, Wenner M, Marx S. Experimental investigation on the rail residual stress distribution and its influence on the bending fatigue resistance of rails. *Constr Build Mater* 2021;284:122856.
- [81] Wineman SJ, McClintock FA. Rail web fracture in the presence of residual stresses. *Theoret Appl Fract Mech* 1987;8:87–99.
- [82] Wineman SJ, McClintock FA. In: Orringer O, Orkisz J, Swiderski Z, editors. Residual stress in rails, Engineering applications of fracture mechanics, Vol. 12–13. Dordrecht, Germany: Springer; 1992. p. 1–22. Ch. Residual stresses and web fracture in roller-straightened rail.
- [83] Moser A, Pointner P. Head-hardened rails produced from rolling heat. *Transp Res Rec* 1992;1341:70–4.
- [84] Webster PJ, Wang X, Mills G, Webster GA. Residual stress changes in railway rails. *Phys B* 1992;180–181:1029–31.
- [85] Kuchuk-Yatsenko S, Didkovsky A, Shvets V, Rudenko P, Antipin E. Flash-butt welding of high-strength rails of nowadays production. *Paton Weld J No. 5–6* 2016:4–12.
- [86] Prokofiev O, Gubatyuk R, Rymar S, Sydorets V, Kostin V. Inductor for uniform bulk heat treatment of welded butt joints of railway rails. *Solid State Phenom* 2021;313:72–81.
- [87] Weingrill L, Krutzler J, Enzinger N. Temperature field evolution during flash butt welding of railway rails. *Mater Sci Forum* 2017;879:2088–93.
- [88] Enzinger N, Weingrill L. Private communication to H.K.D.H. Bhadeshia, flash butt welding; January 2024.
- [89] NPL, MTDATA, Software, National Physical Laboratory, Teddington, U.K; 2006.
- [90] Farhangi H, Mousavizadeh SM. Horizontal split-web fractures of flash butt welded rails. In: Proceedings of the 8th International Fracture Conference, Vol. 7, Yildiz Technical University Istanbul, Yildiz Technical University Istanbul, Istanbul, Turkey; 2007. p. 509–517.
- [91] Procaro RR, Faria GL, Godefroid LB, Apolonio GR, Gândido LC, Pinto ES. Microstructure and mechanical properties of a flash butt welded pearlitic rail. *J Mater Process Technol* 2019;270:20–7.
- [92] Pereira HB, Echeverri EAA, Alves LHD, Goldstein H. Evaluation of the effect of heat input and cooling rate of rail flash-butt welding using finite element method simulation. *Soldagen & Inspeção* 2022;27:e2701.
- [93] Voronin NN, Seydakhmetov NB, Rezanov VA. Development of the combined flashing method in welding of rails. *Weld Int* 2017;31:984–7.
- [94] Goldschmidt H. Process for the manufacture of metals or alloys of the same, Imperial Patent No. 96317, Germany; 1895.
- [95] Messel R. Progress in industrial chemistry. *Industr Eng Chem* 1912;4:767–71.
- [96] Shepard ER. Modern practice in the construction and maintenance of rail joints and bonds in electric railways, no. 62 in Technologic papers of the Bureau of Standards, US Government Printing Office; 1920.
- [97] de Souza KM, de Lemos MJS, Kawachi EY. Thermodynamics of thermite reactions for a new thermal plug and abandonment process. *Continuum Mech Thermodyn* 2022;34:259–71.
- [98] Mutton PJ, Alvarez EF. Failure modes in aluminothermic rail welds under high axle load conditions. *Eng Fail Anal* 2004;11:151–66.
- [99] Mutton P. Private communication to H.K.D.H. Bhadeshia, soft zone in welded rails; August 2022.
- [100] Shira S. Linear friction welding for constructing and repairing rail for high speed and intercity passenger service rail, Tech. Rep. DOT/FRA/ORD-16/32, United States. Federal Railroad Administration, Office of Research, Development, and Technology, Washington, D.C., USA; 2016.
- [101] Bhamji I, Preuss M, Threadgill PL, Addison A. Solid state joining of metals by linear friction welding: a literature review. *Mater Sci Technol* 2011;27:2–12.
- [102] Brouzoulis J, Josefson BL, Faes K, Andersson T, Maglio M, Jackman S, Janssens A. Orbital friction welding of steel bars – heat generation and process modelling. *Proc Inst Mech Eng, Part L: J Mater: Des Appl* 2023;1715–24.
- [103] Shtrikman M. Linear friction welding. *Weld Int* 2010;24:563–9.
- [104] Tan J, Gao Z, Ren S, Xu Q, Wang K, Zeng Q. Improving the microstructures and mechanical properties of u71mn rail steel liner friction welded joint by normalizing treatment. *Mater Today Commun* 2024;38:107736.
- [105] Andersson J, Ek J, Elfving F, Hæg J. Linear friction welding of rail materials. Sweden: Chalmers University; 2019. Tech. Rep. TME131.
- [106] Mutton P, Cookson J, Qiu C, Welsby D. Microstructural characterisation of rolling contact fatigue damage in flashbutt welds. *Wear* 2016;366:368–77.
- [107] Wahlstedt I. Fe modeling of orbital friction welding. Sweden: Chalmers University of Technology; 2016. Master's thesis.
- [108] Thomas WM, Nicholas ED, Needham JC, Murch MG, Temple-Smith P, Dawes CJ. Friction stir butt welding. International Patent Application December 1991; no. PCT/GB92/02203.
- [109] Dawes CJ, Thomas WM. Friction stir process welds aluminium alloys. *Weld J* 1996;73:41–5.
- [110] Thomas WM, Dolby RE. Friction stir welding developments. In: David SA, DebRoy T, Lippold JC, Smartt HB, Vitek JM, editors. 6th Int. Trends in Welding Research. Materials Park, Ohio, USA: ASM International; 2003. p. 203–11.
- [111] Nandan R, DebRoy T, Bhadeshia HKDH. Recent advances in friction-stir welding – Process, weldment structure and properties. *Prog Mater Sci* 2008;53: 980–1023.
- [112] DebRoy T, Bhadeshia HKDH. Innovations in Everyday Engineering Materials. Switzerland: Springer Nature; 2021.
- [113] Masithulela F. Conceptual design of a friction stir welding machine for joining rails. South Africa: University of the Witwatersrand; 2009. Master's thesis.
- [114] Threadgill PL, Leonard AJ, Shercliff HR, Withers PJ. Friction stir welding of aluminium alloys. *Int Mater Rev* 2009;54:49–93.
- [115] Bhadeshia HKDH, DebRoy T. Critical assessment: Friction stir welding of steels. *Sci Technol Weld Join* 2009;14:193–6.
- [116] De A, Bhadeshia HKDH, DebRoy T. Friction stir welding of mild steel: tool durability and steel microstructure. *Mater Sci Technol* 2014;30:1050–6.
- [117] Forsman O. Undersökning av rymdstrukturen hos ett kolstal av hypereutektoid sammansättning. *Jernkontorets Annaler* 1918;102:1–30.
- [118] Darken LS, Fisher RM. Some observations on the growth of pearlite. In: Zackay VF, Aaronson HI, editors. Decomposition of austenite by diffusional processes. Interscience publishers; 1962. p. 249–94.
- [119] Hillert M. The formation of pearlite. In: Zackay VF, Aaronson HI, editors. Decomposition of Austenite by Diffusional Processes. New York, USA: Interscience; 1962. p. 197–237.
- [120] Adachi Y, Morooka S, Nakajima K, Sugimoto Y. Computer-aided three-dimensional visualization of twisted cementite lamellae in eutectoid steel. *Acta Mater* 2008;56:5995–6002.
- [121] Mintz B. Role of silicon in influencing strength and impact behaviour of ferrite and its likely influence at ultrafine grain size. *Mater Sci Technol* 2000;16: 1282–6.
- [122] Zeng D, Lu L, Gong Y, Zhang Y, Zhang J. Influence of solid solution strengthening on spalling behavior of railway wheel steel. *Wear* 2017;372–373:158–68.
- [123] Masoumi M, Echeverri EAA, Tschiptschin AP, Goldstein H. Improvement of wear resistance in a pearlitic rail steel via quenching and partitioning processing. *Scient Rep* 2019;9:7454.
- [124] Bhadeshia HKDH, Chinthra AR. Critical assessment: the strength of undeformed pearlite. *Mater Sci Technol* 2022;38:1291–9.
- [125] Ferreira VM, Mecozzi MG, Petrov RH, Sietsma J. Microstructure development of pearlitic railway steels subjected to fast heating. *Mater Des* 2022;221:110989.
- [126] Leslie WC. Iron and its dilute substitutional solid solutions. *Metall. Trans. A* 1972;3:5–23.
- [127] Bhadeshia HKDH. Cementite. *Int Mater Rev* 2020;65:1–27.
- [128] Tewari SK, Sharma RC. The effect of alloying elements on pearlite growth. *Metall Trans. A* 1985;16:597–603.

- [129] Sahay S, Mohapatra G, Totten G. Overview of pearlitic rail steel: accelerated cooling, quenching, microstructure, and mechanical properties. *J ASTM Int* 2009; 6:1–26.
- [130] Wang J, Zhang F, Yang Z. Effects of alloying elements and cooling rates on the high-strength pearlite steels. *Mater Sci Technol* 2017;33:1673–80.
- [131] Bhadeshia HKDH. *Theory of Transformations in Steels*. Taylor and Francis Group, London, U.K.: CRC Press; 2021.
- [132] Shilov VA SE, Shvarts DL. Aspects of the rolling of long rails on a universal rail-beam mill. *Metallurgist* 2016;60: 260–66.
- [133] Nesterov D, Razin'kova N, Chernyakova L, Kisil B. Structure and mechanical properties of rails type r65 bulk-hardened in oil. *Met Sci Heat Treat* 1991;33: 331–6.
- [134] Jabłońska M, Lewandowski F, Chmiela B, Gronostajski Z. Advanced heat treatment of pearlitic rail steel. *Materials* 2023;16:6430.
- [135] Sinel'nikov V, Filippov G. Technological aspects of improving the quality and service properties of railroad rails. *Metallurgist* 2001;45:403–7.
- [136] Bramfitt BL. Accelerated cooling of rail. *Iron & Steelmaker* 1991;18:33–41.
- [137] Rodrigues KF, ao GMMM, Faria GL. Kinetics of isothermal phase transformations in premium and standard rail steels. *Steel Res Int* 2021;92:2000306.
- [138] Yuryev A, Kozyrev N, Shevchenko R, Mikhno A, Gutak O. Phase transformations occurring during the formation of a welded joint from rail steel. In: *E3S Web of Conferences*, Vol. 330. France: EDP Sciences; 2021. p. 02007.
- [139] Kawulok R, Schindler I, Mizera J, Kawulok P, Ruzs S, Opéla P, Podolinský P, Čmiel KM, Mališ M. Transformation diagrams of selected steel grades with consideration of deformation effect. *Arch Metall Mater* 2018;63:55–60.
- [140] Chen P, Chen L, Xu J, Huang S, Xia Z. Formation mechanism of pearlite during thermal cycling in U75V steel rail repaired by laser directed energy deposition. *J Laser Appl* 2021;33:101–6.
- [141] Strife JR, Carr MJ, Ansell GS. Effect of austenite prestrain above the M_d temperature on the M_s temperature in Fe-Ni-Cr-C alloys. *Metall Trans A* 1977;8A: 1471–84.
- [142] Maki T, Tamura I. Microstructure and mechanical properties of martensite formed from work-hardened austenite. In: *International Conference on Physical Metallurgy of Thermomechanical Processing of Steels and Other Metals. THERMEC-88*, Vol. 2. Tokyo, Japan: The Iron and Steel Institute of Japan; 1988. p. 458–66.
- [143] Christian JW, Mahajan S. Deformation twinning. *Prog Mater Sci* 1995;39:1–157.
- [144] Chatterjee S, Wang HS, Yang JR, Bhadeshia HKDH. Mechanical stabilisation of austenite. *Mater Sci Technol* 2006;22:641–4.
- [145] Belaiew NT. The inner structure of the pearlite grain. *J Iron Steel Inst* 1922;105:201–27.
- [146] Hultgren A. Isothermal transformation of austenite. *Trans Am Soc Met* 1947;39:915–1005.
- [147] Olivares RO, Garcia CI, DeArdo A, Kalay S, Hernández FCR. Advanced metallurgical alloy design and thermomechanical processing for rails steels for North American heavy haul use. *Wear* 2011;271:364–73.
- [148] Han K, Edmonds DV, Smith GDW. Optimization of mechanical properties of high-carbon pearlitic steels with Si and V additions. *Metall Mater Trans A* 2001;32: 1313–23.
- [149] Ordonez R, Garcia CI, DeArdo AJ. Effect of thermomechanical processing and cooling rate conditions on the austenite decomposition behavior in hypereutectoid steels. In: *Austenite Formation and Decomposition IV*, Vol. 10, Materials Science and Technology Conference and Exhibition, Texas, USA; 2010. p. 1327–1335.
- [150] Andrews KW. Empirical formulae for the calculation of some transformation temperatures. *J Iron Steel Inst* 1965;203:721–7.
- [151] Schneider H. Investment casting of high hot-strength 12% chrome steel. *Found Trade J* 1960;108:562–3.
- [152] Takahashi M. Reaustenitisation from bainite in steels. University of Cambridge; 1992. Ph.D. thesis, <http://www.phase-trans.msm.cam.ac.uk/2000/phd.html#Takahashi>.
- [153] Kavishe FPL, Baker TJ. Effect of prior austenite grain size and pearlite interlamellar spacing on strength and fracture toughness of a eutectoid rail steel. *Mater Sci Technol* 1986;2:816–22.
- [154] Clayton P, Danks D. Effect of interlamellar spacing on the wear resistatnce of eutectoid steels under rolling-sliding conditions. *Wear* 1990;135:369–89.
- [155] Reed-Hill RE. *Physical Metallurgy Principles*. 2nd Edition. Boston, USA: PWS Publishers; 1973.
- [156] Dollar M, Bernstein IM, Thompson AW. Influence of deformation substructure on flow and fracture of fully pearlitic steel. *Acta Metall* 1988;36:311–20.
- [157] Li Y, Bushby AJ, Dunstan DJ. The Hall-Petch effect as a manifestation of the general size effect. *Proc Roy Soc A* 2016;472:20150890.
- [158] Sugden AAB, Bhadeshia HKDH. A model for the strength of the as-deposited regions of steel weld metals. *Metall Trans A* 1988;19A:1597–602.
- [159] E. 13674-1, Railway applications-track-rail-part 1: Vignole railway rails 46 kg/m and above, Tech. rep., National Standards Authority of Ireland, Dublin, Eire (2011).
- [160] Li H, Sun J, Zhao G. Research on rail wear of small radius curve in EMU depot. *Railway Sci* 2022;1:16–39.
- [161] Lu P, Lewis SR, Fretwell-Smith S, Engleberg DL, Fletcher DI, Lewis R. Laser cladding of rail; the effects of depositing material on lower rail grades. *Wear* 2019; 438–439:203045.
- [162] van Velsen S. Laser welding on rails. Delft, The Netherlands: Delft University of Technology; 2017. Master's thesis.
- [163] Basu J, Srimani SL, Gupta DS. Rail behaviour during cooling after hot rolling. *J Strain Anal* 2004;39:15–24.
- [164] K. Mädlar, A. Zoll, R. Heyder, M. Brehmer, Rail materials - alternatives and limits. In: *Proceedings of the 8th World Congress on Railway Research, UNION INTERNATIONALE DES CHEMINS DE FER, France; 2008*. p. 18–22.
- [165] Pointner P, Hierg A, Jaiswal J. Definitive guidelines on the use of different rail grades. Sweden: D4.1.5GL, Chalmers University; 2006. Tech. Rep. TIP5-CT-2006-031415.
- [166] Jaiswal PSJ. Crossrail rcf and wear study: literature review and data gathering. University of Huddersfield; 2016. Tech. Rep. IRR 184/14.
- [167] Pang Y, Grilli N, Su H, Liu W, Ma J, Yu SF. Experimental investigation on microstructures and mechanical properties of PG4 flash-butt rail welds. *Eng Fail Anal* 2022;141:106650.
- [168] Su H, Pun CL, Mutton P, Kan Q, Kang G, Yan W. Numerical study on the ratcheting performance of rail flash butt welds in heavy haul operations. *Int J Mech Sci* 2021;199:106434.
- [169] Pawan A, Salleh Z, Zulkefli AH, Talib YM, Alsibramulsi A, Masdek NR. Tensile properties of the reclaimed steel rail flash butt joint. *IOP Conf Ser: Mater Sci Eng* 2019;628:012008.
- [170] Hao K, Di W, Zhao X-M. Surface temperature change of U75V 60 kg/m heavy rail during heat treatment. *J Iron Steel Res, Int* 2013;20:33–67.
- [171] Wu H, Huang S, Li Z, Chen P, Tan H, Xia Z. Optimization of microstructure and properties in U75V steel rail cladding layers manufactured by laser melting deposition and laser shock peening. *Opt Laser Technol* 2023;163:109436.
- [172] Bkowski H, Piwnik J. Quantitative and qualitative comparison of tribological properties of railway rails with and without heat treatment. *Arch Metall Mater* 2016;16:469–474.
- [173] Nesterov D, Sapozhkov V, Levchenko N, Dubrov V. Heat treatment of rail steel using induction heating. *Met Sci Heat Treat* 1990;32:589–94.
- [174] Saeki K, Iwano K. Progress and prospects of rail for railroads, Tech. Rep. 105, Nippon Steel & Sumitomo Metal Technical Report, Japan; 2013.
- [175] Clare AT, Oyelola O, Abioye TE, Farayibi PK. Laser cladding of rail steel with Co-Cr. *Surf Eng* 2013;29:731–6.
- [176] Rasmussen CJ, Faester SF, Dhar S, Quaade JV, Bini M, Danielsen HK. Surface crack formation on rails at grinding induced martensite white etching layers. *Wear* 2017;384–385:8–14.
- [177] Ekberg A, Paulsson B. INNOTRACK: Concluding technical report, Tech. rep., International Union of Railways (UIC); 2010.
- [178] Pointner P, Joerg A, Jaiswal J. Deliverable D4.1.5, definitive guidelines on the use of different rail grades. Innotrack Project; 2009. Tech. rep.
- [179] Li J, Han Z, Zhao H. Optimization of heat treatment process for high strength steel rail R400HT. *Heat Treat Met* 2023;48(6):101–6.
- [180] R. Carroll, H.M. Smith, S. Jaiswal, U.S. Patent No. 8,430,976: Rail steel with an excellent combination of wear properties and rolling contact fatigue resistance, Tech. rep., U.S. Patent and Trademark Office, Washington, DC; 2013.
- [181] A. Bevan, J. Jaiswal, A. Smith, M. Ojeda Cabral, Judicious selection of available rail steels to reduce life-cycle costs, *Proceedings of the Institution of Mechanical Engineers, Part F: Journal of rail and rapid transit* 234 (2020) 257–275.

- [182] H. Pereira, E. Ariza, D. Centeno, S. Souza, H. Goldenstein, L. Alves, A. Wilson, S. Lewis, Superior wear resistance of novel HP335 rail steel, in: Proceedings of International Heavy Haul Conference, Brazil; 2023. p. 1–5.
- [183] Wilby A, Corteen J, Lewis S, Lewis R, Fletcher D. Nano and micro-indentation driven characterisation of asperity and bulk plasticity at the surface of modern premium rail steels. *Wear* 2023;530–531:205004.
- [184] Woodhead DH. Investigating the performance of rail steels. *J Huddersfield Student Res* 2021;7:1–15.
- [185] Secrodel P, Jaiswal J. Private communication to H.K.D.H. Bhadeshia, performance of carbide-free bainitic rail; 2020.
- [186] Anonymous, Bainitic low fatigue, <https://britishsteel.co.uk/what-we-do/rail/flat-bottomed-vignole-rail/bainitic-low-fatigue-blf/>; 2022.
- [187] Cristofari F. Moving points on high speed rail system, moving points on high speed rail system; 2022.
- [188] Jaiswal J. Private communication to H.K.D.H. Bhadeshia, moveable point crossings; August 2022.
- [189] Sysyn M, Kluge F, Gruen D, Kovalchuk V, Nabochenko O. Experimental analysis of rail contact fatigue damage on frog rail of fixed common crossing 1:12. *J Fail Anal Prev* 2019;19:1077–92.
- [190] Sun X, Wang P, Chen J, Hao C, Xu J. Analytical representations of inherent structural irregularities in turnout crossing with moveable point. *Vehicle Syst Dynam ahead-of-print* 2022. <https://doi.org/10.1080/00423114.2022.2062010>.
- [191] Girsch G, Heyder R. Advanced pearlitic and bainitic high strength rails promise to improve rolling contact fatigue resistance. In: in: 7th World Congress on Railway Research (WCR2006). Montréal, Canada: World Congress for Railway Research; 2006. p. 2–10.
- [192] A. Bevan, J. Jaiswal, A. Smith, M.O. Cabral, Judicious selection of available rail steels to reduce life-cycle costs, Proceedings of IMechE Part F: Journal of Rail and Rapid Transit 234 (2018) 257–275.
- [193] Turan ME, Ozcelik S, Sun Y, Ahlatci H, Cetin M. Residual stress measurement in R260 and R260MN quality rails. In: International Symposium on Railway Systems Engineering, Karabük Üniversitesi, Karabük, Turkey; 2016. p. 372–8.
- [194] Shur EA, Bychkova NY, Trushevsky SM. Physical metallurgy aspects of rolling contact fatigue of rail steels. *Wear* 2005;258:1165–71.
- [195] Bolton PJ, Clayton P. Rolling-sliding wear damage in rail and tyre steels. *Wear* 1984;93:145–65.
- [196] Su X, Clayton P. Surface-initiated rolling contact fatigue of pearlitic and low carbon bainitic steels. *Wear* 1996;197:137–44.
- [197] Markov D. Laboratory tests for wear of rail and wheel steels. *Wear* 1995;181:678–86.
- [198] Sato M, Anderson PM, Rigney DA. Rolling-sliding behaviour of rail steels. *Wear* 1993;162–164:159–72.
- [199] Bayer RJ. Mechanical Wear Fundamentals and Testing, revised and expanded. New York, USA: CRC Press; 2004.
- [200] Wong JY. Theory of ground vehicles. USA: John Wiley & Sons; 2022.
- [201] Six K, Meierhofer A, Trummer G, Bernsteiner C, Marte C, Müller G, Lubner B, Dietmaier P, Rosenberger M. Plasticity in wheel – rail contact and its implications on vehicle – track interaction. *Proc Inst Mech Eng, Part F: J Rail Rapid Transit* 2017;231:558–69.
- [202] Vollebregt E, Six K, Polach O. Challenges and progress in the understanding and modelling of the wheel–rail creep forces. *Vehicle Syst Dynam* 2021;59:1026–68.
- [203] Chen H, Zhang C, Liu W, Li Q, Chen H, Yang Z, Weng Y. Microstructure evolution of a hypereutectoid pearlite steel under rolling-sliding contact loading. *Mater Sci Eng: A* 2016;655:50–9.
- [204] Trummer G, Marte C, Scheriau S, Dietmaier P, Sommitsch C, Six K. Modeling wear and rolling contact fatigue: Parametric study and experimental results. *Wear* 2016;366:71–7.
- [205] Bower AF, Johnson KL. Plastic flow and shakedown of the rail surface in repeated wheel-rail contact. *Wear* 1991;144:1–18.
- [206] Tyfour WR, Beynon JH, Kapoor A. Deterioration of rolling contact fatigue life of pearlitic rail steel due to dry-wet rolling-sliding line contact. *Wear* 1996;197:255–65.
- [207] Johnson KL. Contact Mechanics. Cambridge, U.K.: Cambridge University Press; 1985.
- [208] Su X, Clayton P. Ratchetting strain experiments with a pearlitic steel under rolling/sliding contact. *Wear* 1997;205:137–43.
- [209] Suh NP. The delamination theory of wear. *Wear* 1973;25:111–24.
- [210] Makino T, Kato T, Hirakawa K. The effect of slip ratio on the rolling contact fatigue property of railway wheel steel. *Int J Fatigue* 2012;36:68–79.
- [211] Ohyama T. Fundamental adhesion phenomena between wheel and rail at high speeds, some experiments with a high speed rolling test machine under water. *Quart Rep Railway Tech Res Inst Japan* 1985;26:135–40.
- [212] Trummer G, Lee ZS, Lewis R, Six K. Modelling of frictional conditions in the wheel-rail interface due to application of top-of-rail products. *Lubricants* 2021;9:100.
- [213] Suhr B, Butcher T, Lewis R, Six K. Friction and wear in railway ballast stone interfaces. *Tribol Int* 2020;151:106498.
- [214] Carter FW. On the action of a locomotive driving wheel. *Proc Roy Soc London A: Mathematical, Physical and Engineering Sciences* 1926;112: 151–7.
- [215] Maya-Johnson S, Felipe Santa J, Toro A. Dry and lubricated wear of rail steel under rolling contact fatigue - wear mechanisms and crack growth. *Wear* 2017;380–381:240–50.
- [216] Fletcher DI, Hyde P, Kapoor A. Investigating fluid penetration of rolling contact fatigue cracks in rails using a newly developed full-scale test facility. *J Rail Rapid Transit* 2007;221:35–44.
- [217] Donzella G, Faccoli M, Ghidini A, Mazzu A, Roberti R. The competitive role of wear and RCF in a rail steel. *Eng Fract Mech* 2005;72:287–308.
- [218] Zakhharov S, Goryacheva IG. Rolling contact fatigue defects in freight car wheel. *Wear* 2005;258:1142–7.
- [219] Fletcher DI. The influence of lubrication on the fatigue of pearlitic rail steel, Ph.D. thesis, Department of Mechanical Engineering, University of Sheffield; 1999.
- [220] Fletcher DI, Beynon JH. Equilibrium of crack growth and wear rates during unlubricated rolling-sliding contact of pearlitic rail steel. *Proc Inst Mech Eng, Part F: J Rail Rapid Transit* 2000;214:93–105.
- [221] Franklin FJ, Garnham JE, Fletcher DI, Davis CL, Kapoor A. Modelling rail steel microstructure and its effect on crack initiation. *Wear* 2008;265:1332–41.
- [222] Deters L, Proksch M. Friction and wear testing of rail and wheel material. *Wear* 2005;258:981–91.
- [223] Zhang W, Chen J, Wu X, Jin X. Wheel/rail adhesion and analysis by using full scale roller rig. *Wear* 2002;253:82–8.
- [224] Gallardo-Hernandez EA, Lewis R. Twin disc assessment of wheel/rail adhesion. *Wear* 2008;265:1309–16.
- [225] Olofsson U, Sundvall K. Influence of leaf, humidity and applied lubrication on friction in the wheel-rail contact: pin-on-disc experiments. *Proc Inst Mech Eng, Part F: J Rail Rapid Transit* 2004;218:235–42.
- [226] Lewis R, Trummer G, Six K, Stow J, Alturbeh H, Bryce B, Shackleton P, Johnstone LB. Leaves on the line: Characterising leaf based low adhesion on railway rails. *Tribol Int* 2023;185:108529.
- [227] Chen H, Kimura S, Ikoma K, Ishizaka K, Suzumura J, Hibino S. Evaluation test of tangential force coefficient under different types of fallen leaves. *Wear* 2023;532–533:205072.
- [228] Chen H, Ban T, Ishida M, Nakahara T. Experimental investigation of influential factors on adhesion between wheel and rail under wet conditions. *Wear* 2008;265:1504–11.
- [229] Chen H, Ishida M, Nakahara T. Analysis of adhesion under wet conditions for three-dimensional contact considering surface roughness. *Wear* 2005;258:1209–16.
- [230] Kapoor A, Franklin FJ, Wong SK, Ishida M. Surface roughness and plastic flow in rail wheel contact. *Wear* 2002;253:257–64.
- [231] Johnson KL. The strength of surfaces in rolling contact. In: Proceedings of the Institution of Mechanical Engineers, Part C: Journal of Mechanical Engineering Science 1989;Vol. 203. p. 151–63.
- [232] Nowell D, Hills DA. Hertzian contact of ground surfaces. *J Tribol* 1989;111:175–9.
- [233] Ishida M, Abe N. Experimental study on rolling contact fatigue from the aspect of residual stress. *Wear* 1996;191:65–71.
- [234] Ponter ARS, Hearle AD, Johnson KL. Application of the kinematical shakedown theorem to rolling and sliding point contacts. *J Mech Phys Solid* 1985;33:339–62.
- [235] Ringsberg JW. Life prediction of rolling contact fatigue crack initiation. *Int J Fatigue* 2001;23:575–86.
- [236] Manolov N. Acoustical method of investigation of contact of solids. Bulgaria: Report of Sofia Technical University; 1970. Tech. rep.

- [237] Manolov N. Acoustical method of investigation of contact of solids. Ph.D. thesis. USSR: Moscow State University; 1970.
- [238] Krolkowski J, Szczepk J. Phase shift of the reflection coefficient of ultrasonic waves in the study of the contact interface. *Wear* 1992;157:51–64.
- [239] Pau M, Aymerich F, Ginesu F. Distribution of contact pressure in wheel–rail contact area. *Wear* 2002;253:265–74.
- [240] K. Kendall, D. Tabor, An ultrasonic study of the area of contact between stationary and sliding surfaces, *Proc Roy Soc London A: Mathematical, Physical and Engineering Sciences* 323 (1971) 321–340.
- [241] Haines DJ, Ollerton E. Contact stress distributions on elliptical contact surfaces subjected to radial and tangential forces. *Proc Inst Mech Eng* 1963;177:95–114.
- [242] Woo KL, Thomas TR. Contact of rough surfaces: a review of experimental work. *Wear* 1980;58:331–40.
- [243] van Dokkum J, Khajeh Salehani M, Irani N, Nicola L. On the proportionality between area and load in line contacts. *Tribol Lett* 2018;66:115.
- [244] Müser MH. On the linearity of contact area and reduced pressure. *Tribol Lett* 2017;65:129.
- [245] Paggi M, Ciavarella M. The coefficient of proportionality κ between real contact area and load, with new asperity models. *Wear* 2010;268:1020–9.
- [246] Archard JF. Friction between metal surfaces. *Wear* 1986;113:3–16.
- [247] Archard J. Contact and rubbing of flat surfaces. *J Appl Phys* 1953;24:981–8.
- [248] Rigney DA. Viewpoint set on materials aspects of wear-introduction. *Scripta Mater* 1990;24:799–803.
- [249] Jin Y, Ishida M, Namura A. Experimental simulation and prediction of wear of wheel flange and rail gauge corner. *Wear* 2011;271:259–67.
- [250] Wang Y, Lei T, Liu J. Tribology-metallographic behavior of high carbon steels in dry sliding: I. Wear mechanisms and their transition. *Wear* 1999;231:1–11.
- [251] Zakharov S, Komarovskiy I, Zharov I. Wheel flange/rail head wear simulation. *Wear* 1998;215:18–24.
- [252] Lewis R, Olofsson U. Mapping rail wear regimes and transitions. *Wear* 2004;257:721–9.
- [253] Ashby MF, Lim SC. Wear-mechanism maps. *Scr Metall Mater* 1990;24:805–10.
- [254] Lim SC, Ashby MF. Overview no. 55 wear-mechanism maps. *Acta Metall* 1987;35:1–24.
- [255] Lim SC, Ashby MF, Brunton JH. Wear-rate transitions and their relationship to wear mechanisms. *Acta Metall* 1987;35:1343–8.
- [256] Akagaki T, Kato K. Wear mode diagram in lubricated sliding friction of carbon steel. *Wear* 1989;129:303–17.
- [257] Wang Y, Lei T, Yan M, Gao C. Frictional temperature field and its relationship to the transition of wear mechanisms of steel 51200. *J Phys D: Appl Phys* 1992; 25:A165.
- [258] Fischer FD, Daves W, Werner EA. On the temperature in the wheel–rail rolling contact. *Fatigue & Fract Eng Mater Struct* 2003;26:999–1006.
- [259] Lewis R, Dwyer-Joyce RS. Wear mechanisms and transitions in railway wheel steels. *Proc Inst Mech Eng, Part J: J Eng Tribol* 2004;218:467–78.
- [260] McEwen IJ, Harvey RF. Full-scale wheel-on-rail wear testing: comparisons with service wear and a developing theoretical predictive method. *Lubr Eng* 1985; 41:80–8.
- [261] Rosenfield AR. Wear and fracture mechanics: Are they related. *Scr Metall Mater* 1990;24:811–4.
- [262] Danks D, Clayton P. Comparison of the wear process for eutectoid rail steels: Field and laboratory tests. *Wear* 1987;120:233–50.
- [263] Welsh NC. The dry wear of steels I. The general pattern of behaviour. *Philos Trans Roy Soc London A* 1965;257:31–50.
- [264] Welsh NC. The dry wear of steels II. Interpretation and special features. *Philos Trans Roy Soc London A* 1965;257:51–70.
- [265] Wang Y, Li XD, Feng Z. The relationship between the product of load and sliding speed with friction temperature and sliding wear of a 52100 steel. *Scr Metall Mater* 1995;33:1163–8.
- [266] Wang Y, Gao CQ, Lei TC, Lu HX. Amorphous structure of worn surface in 52100 steel. *Scr Metall* 1988;22:1251–4.
- [267] Vingsbo O, Hogmark S. Single-pass pendulum grooving – a technique for abrasive testing. *Wear* 1984;100:489–502.
- [268] Kapoor A, Franklin FJ. Tribological layers and the wear of ductile materials. *Wear* 2000;245:204–15.
- [269] Sasada T. Wear research in Japan: Trends and future directions. *Wear* 1984;100:561–77.
- [270] Wang Y, Lei T, Liu J. Tribology-metallographic behavior of high carbon steels in dry sliding: II. microstructure and wear. *Wear* 1999;231:12–9.
- [271] Steele RK, Reiff RP. Rail: Its behaviour and relationship to total system wear. In: *Proceedings of the Second International Heavy Haul Railway Conference, Colorado, USA; 1982*. p. 115–64.
- [272] Pointner P. High strength rail steels – the importance of material properties in contact mechanics problems. *Wear* 2008;265:1373–9.
- [273] Sawley K, Kristan J. Development of bainitic rail steels with potential resistance to rolling contact fatigue. *Fatigue & Fract Eng Mater Struct* 2003;26:1019–29.
- [274] Chang LC. The rolling/sliding wear performance of high silicon carbide-free bainitic steels. *Wear* 2005;258:730–43.
- [275] Bhadeshia HKDH. *Bainite in Steels: Theory and Practice*. 3rd Edition. Leeds, U.K.: Maney Publishing; 2015.
- [276] Rothäuser N, Muders L, Grohmann HD. Influence of surface-decarburisation area of the rail on rolling contact fatigue. *Eisenbahningenieur* 2001;52:62–5.
- [277] Boulanger D. Rail metallurgical developments to address the changing needs of the railway, in: *Proceedings of the World Congress of Rail Research; 2003*. p. 932–9.
- [278] Voskamp AP. Microstructural changes during rolling contact fatigue. Ph.D. thesis. Technical University of Delft; 1996.
- [279] Clayton P. The relations between wear behaviour and basic material properties for pearlitic steels. *Wear* 1980;60:75–93.
- [280] B.E. 13674-1:2011, *Railway applications. track. rail. vignole railway rails 46 kg/m and above*, Tech. rep., British Standards Institute, London, U.K; 2011.
- [281] Purbrick MC. The use of rail on british railways. In: *Second International Heavy Haul Conference, International Heavy Haul Association, Virginia, USA; 1982*. p. 380–7.
- [282] Gahr KHZ. *Microstructure and wear of materials*, Vol. 10. North-Holland: Elsevier; 1987.
- [283] Bakshi SD, Shipway PH, Bhadeshia HKDH. Three-body abrasive wear of fine pearlite, nano-structured bainite and martensite. *Wear* 2013;308:46–53.
- [284] Larsen-Basse J. Role of microstructure and mechanical properties in abrasion. *Scr Metall Mater* 1990;24:821–6.
- [285] Moore MA. The relationship between the abrasive wear resistance, hardness and microstructure of ferritic materials. *Wear* 1974;28:59–68.
- [286] Bhadeshia HKDH, Honeycombe RWK. *Steels – structure, properties and design*. 5th Edition. London, U.K.: Elsevier Butterworth-Heinemann; 2024.
- [287] Kalousek J, Fegredo DM, Laufer EE. Wear resistance and worn metallography of pearlite, bainite and tempered martensite rail steel microstructures. *Wear* 1985;105:199–222.
- [288] Takahashi T, Nagumo M. Flow stress and work-hardening of pearlitic steel. *Trans JIM* 1970;11:113–9.
- [289] Wang Y, Tomota Y, Ohmura T, Gong W, Harjo S, Tanaka M. Continuous and discontinuous yielding behaviors in ferrite-cementite steels. *Acta Mater* 2020;196: 565–75.
- [290] Bhattacharyya S. Wear and friction in steel, aluminum and magnesium alloys I. Pearlitic and spheroidized steels. *Wear* 1980;61:133–41.
- [291] Fegredo DM, Kalousek J, Shehata MT. The effect of progressive minor spheroidization on the dry-wear rates of a standard carbon and a Cr-Mo alloy rail steel. *Wear* 1993;161:29–40.
- [292] Underwood EE. *Quantitative Stereology*. Addison-Wesley Publication Company; 1970.
- [293] da Fonseca Gomes GM, de Almeida LH, Gomes LCF, May IL. Effects of microstructural parameters on the mechanical properties of eutectoid rail steels. *Mater Charact* 1997;39:1–14.
- [294] Kimura T, Takemasa M, Honjo M. Development of SP3 rail with high wear resistance and rolling contact fatigue resistance for heavy haul railways. *JFE Techn Rep* 2011;16:32–7.
- [295] K. Tokunaga, T. Arimura, M. Yamaguchi, H. Fukuda, M. Honjo, R. Matsuoka, M. Takemasa, Development of SP4 rail with high wear resistance for heavy haul railways, Tech. rep., JFE steel.
- [296] Hall EO. The deformation and ageing of mild steel: III discussion of results. *Proc Phys Soc B* 1951;64:747–53.
- [297] Petch NJ. The cleavage strength of polycrystals. *J Iron Steel Inst* 1953;174:25–8.
- [298] Alexander DJ, Bernstein IM. Microstructural control of flow and fracture in pearlitic steels. In: Marder AR, Goldstein JI, editors. *Phase Transformations in Ferrous Alloys*. Pennsylvania, USA: The Metallurgical Society of AIME; 1984. p. 243–58.
- [299] Ray KK, Mondal D. Effect of interlamellar spacing on strength of pearlite in annealed eutectoid and hypoeutectoid plain carbon steels. *Acta Metall Mater* 1991; 39:2201–8.
- [300] Hyzak JM, Bernstein IM. The role of microstructure on the strength and toughness of fully pearlitic steels. *Metall Trans A* 1976;7:1217–21.

- [301] Honeycombe RWK, Bhadeshia HKDH. Steels: microstructure and properties. 2nd Edition. London, U.K.: Edward Arnold; 1995.
- [302] Sourmail T, Caballero FG, Garcia-Mateo C, Smanio V, Ziegler C, Kuntz M, Elvira R, Leiro A, Vuorinen E, Teeri T. Evaluation of potential of high Si high C steel nanostructured bainite for wear and fatigue applications. *Mater Sci Technol* 2013;29:1166–73.
- [303] Bakshi SD, Leiro A, Prakash B, Bhadeshia HKDH. Dry rolling/sliding wear of nanostructured pearlite. *Mater Sci Technol* 2015;31:1735–44.
- [304] Takahashi J, Kobayashi Y, Ueda M, Miyazaki T, Kawakami K. Nanoscale characterisation of rolling contact wear surface of pearlitic steel. *Mater Sci Technol* 2013;29:1212–8.
- [305] Langford G. Deformation of pearlite. *Metall Trans A* 1977;8:861–75.
- [306] Gil-Sevillano J. Room temperature plastic deformation of pearlitic cementite. *Mater Sci Eng* 1975;21:221–5.
- [307] Fegredo D, Shehata M, Palmer A, Kalousek J. The effect of sulphide and oxide inclusions on the wear rates of a standard c-mn and a cr-mo alloy rail steel. *Wear* 1988;126:285–306.
- [308] Hernández FCR, Demas NG, Gonzales K, Polycarpou AA. Correlation between laboratory ball-on-disk and full-scale rail performance tests. *Wear* 2011;270:479–91.
- [309] Larsen-Badse J, Mathew KG. Influence of structure on the abrasion resistance of a 1040 steel. *Wear* 1969;14:199–205.
- [310] Sarychev V, Molotkov S, Kormyshev V, Nevskii S, Polevoi E. Simulation of differentiated thermal processing of railway rails by compressed air. *Steel Transl* 2020;50:848–54.
- [311] Baumann G. Formation of white-etching layers on rail treads. *Wear* 1996;191:133–40.
- [312] Lojkowski W, Djahanbakhsh M, Bürkle G, Gierlotka S, Zielinski W, Fecht HJ. Nanostructure formation on the surface of railway tracks. *Mater Sci Eng A* 2001;303:197–208.
- [313] Takahashi J, Kawakami K, Ueda M. Atom probe tomography analysis of the white etching layer in a rail track surface. *Acta Mater* 2010;58:3602–12.
- [314] Jahannir S, Suh NP. Mechanics of subsurface void nucleation in delamination wear. *Wear* 1977;44:17–38.
- [315] Cornell HH. Improvement in carbon rail steels by the addition of niobium. *Can Metall Q* 1983;22:347–51.
- [316] Nolasco CA, Bordignon PJP, Oliveira EQ. Trilho niobras 200 elevada resistência mecânica e ao desgaste para ferrovias de frageo infensoepesado (Niobras 200 trail of high resistance mechanical and degassing strength for light and heavy freight railways). In: *Alguns resultados da pesquisa tecnológica na CSN, CSN, Brazil*; 1976. p. 7–13.
- [317] Nolasco CA, Oliveira EQ, Leonardos G, Bordignon PJB. Niobium Si-Mn rail steel. In: *Niobium '81, TMS-AIME, Warrendale, Pennsylvania, USA*; 1984. p. 1041–1060.
- [318] Feifei J. Performance and research of rail steel by added micro-alloy element niobium and vanadium. *J Shandong Univ Build Mater* 2001;15:364–6.
- [319] Singh U, Singh R, Jha S. Influence of microalloying on fracture toughness and wear resistance of rail steel. *Scand J Metall* 1995;24:180–6.
- [320] Liu C, Huang Y, Liu H, Jiang M. Effects and mechanisms of niobium on the fracture toughness of heavy rail steel. *Adv Mater Res* 2011;163:110–6.
- [321] Ray A. Niobium microalloying in rail steels. *Mater Sci Technol* 2017;33:1584–600.
- [322] Rigney DA, Glaeser WA. The significance of near surface microstructure in the wear process. *Wear* 1978;46:241–50.
- [323] Li YJ, Choi P, Borchers C, Westerkamp S, Goto S, Raabe D, Kirchheim R. Atomic-scale mechanisms of deformation-induced cementite decomposition in pearlite. *Acta Mater* 2011;59:3965–77.
- [324] Heller W, Schweitzer R. Hardness, microstructure and wear behaviour of rail steels. In: *2nd Int. Conf. Heavy Haul Railways, Colorado Springs, USA*; 1982. p. 282–6.
- [325] H. Ichinose, J. Takehara, M. Ueda, High strength rails produced by two-stage flame heating and slack-quenching, in: *2nd Int. Conf. on Heavy Haul Railways, Colorado Springs, USA, 1982*, pp. 178–182.
- [326] Fegredo DM, Kalousek J. The effects of mixed microstructures on wear. In: *Proc. 2nd Int. Symp. on Contact Mechanics and Wear of Rail/Wheel Systems. Waterloo, Canada: University of Waterloo Press*; 1987. p. 289–313.
- [327] Ghonem H, Kalousek J, Stone D. Fracture and wear characteristics of Cr-Mo bainitic steel, speciality steels and hard materials. In: *Speciality Steels and Hard Materials, Pergamon Press, Oxford, Pretoria, South Africa*; 1982. p. 259–65.
- [328] Clayton P, Devanathan R. Rolling/sliding wear behavior of a chromium-molybdenum rail steel in pearlitic and bainitic conditions. *Wear* 1992;156:121–31.
- [329] Callender WR. Bainitic transformation and novel bainitic rails steels. Ph.D. thesis. University of Sheffield; 1983.
- [330] Clayton P, Devanathan R, Dikshit V, Christensen DE, Danks D, Steele RK. Recent research on wear, deformation and fatigue of steels in rolling contact. In: *Proceedings of the international symposium on: rail steels-developments, manufacturing and performance. USA: Association for Iron & Steel Technology*; 1992. p. 161–74.
- [331] Mannes W, Hornung K, Rettig H. Testing of gears made of bainitic cast iron with spheroidal graphite. experiences with unalloyed spherical graphite cast qualities. *Antriebstechnik* 1984;23:49–55.
- [332] Garnham JE, Beynon JH. Dry rolling-sliding wear of bainitic and pearlitic steels. *Wear* 1992;157:81–109.
- [333] Leiro A, Vuorinen E, Sundin KG, Prakash B, Sourmail T, Smanio V, Caballero FG, Gracia-Mateo C, Elvira R. Wear of nano-structured carbide-free bainitic steels under dry rolling-sliding conditions. *Wear* 2013;298–299:42–7.
- [334] Hodgson WH, Preston RR. Rails for the 1990s. *Bull Canad Inst Min Metall* 1988;81:95–101.
- [335] Gahr KHZ. Influence of thermal treatments on abrasive wear resistance of tool steels. *Zeitschrift für Metallkunde* 1977;68:783–92.
- [336] Hogmark S, Vingsbo O, Fridström S. Mechanisms of dry wear of some martensitic steels. *Wear* 1975;31:39–61.
- [337] Vingsbo O, Hogmark S. *Wear of Steels*. Materials Park, Ohio, USA: ASM International; 1981.
- [338] Schilke M. Degradation of railway rails from a materials point of view. Ph.D. thesis. Gothenburg, Sweden: Chalmers University of Technology; 2013.
- [339] Ghosh G, Olson GB. Precipitation of paraequilibrium cementite: experiments, thermodynamic and kinetic modelling. *Acta Mater* 2002;50:2099–119.
- [340] Kozeschnik E, Bhadeshia HKDH. Influence of silicon on cementite precipitation in steels. *Mater Sci Technol* 2008;24:343–7.
- [341] Bhadeshia HKDH. *Bainite in Steels*. 2nd Edition. London, U.K.: Institute of Materials; 2001.
- [342] Ordóñez-Olivares R, García CI, DeArdo A, Kalay S, Robles-Hernández FC. Advanced metallurgical alloy design and thermomechanical processing for rails steels for North American heavy haul use. *Wear* 2011;271:364–73.
- [343] Wu KM, Bhadeshia HKDH. Extremely fine pearlite by continuous cooling transformation. *Scripta Mater* 2012;67:53–6.
- [344] McMahon Jr CJ, Cianelli AK, Feng HC. The influence of Mo on P-Induced temper embrittlement in Ni-Cr steel. *Metall Trans A* 1977;8:1055–7.
- [345] Bhadeshia HKDH, Honeycombe RWK. *Steels: Microstructure and Properties*. 4th Edition. Elsevier; 2017.
- [346] Krauss G. *Steels: processing, structure and performance*. Metals Park, Ohio, USA: ASM International; 2005.
- [347] L. Lianxiu, Z. Dongmin, X. Xiaolan, *Review of Progress in Quantitative Nondestructive Evaluation*, Vol. 18A, Springer, US, 1999, Ch. A Study on Ultrasonic Detection of Flaws in Welds of Rails, pp. 2115–2120.
- [348] Independent Investigation Board, Train derailment at Hatfield: A final report by the independent investigation board, Tech. rep., Office of Rail Regulation; July 2006.
- [349] Kemp R. Revisiting the causes of the hatfield rail crash, Tech. rep., Royal Academy of Engineering, London, U.K. (≈; 2022).
- [350] Nierlich W, Gegner J, Bruckner M. X-ray diffraction in failure analysis of rolling bearings. *Mater Sci Forum* 2006;524–525:147–52.
- [351] Coelho L, Dias A, Lieurade HP, Maitournam H. Experimental and numerical rolling contact fatigue study on the 32CrMoV13 steel. *Fatigue Fract Eng Mater Struct* 2004;27:811–23.
- [352] Lankford J, Kusenberger FN. Initiation of fatigue cracks in 4340 steel. *Metall Trans* 1973;4:553–9.
- [353] WenTao L, Zhang Y, ZhiJing F, JingShan Z. Effects of stick-slip on stress intensity factors for subsurface short cracks in rolling contact. *Sci China Technol Sci* 2013;56:2413–21.
- [354] Bakshi SD, Leiro A, Prakash B, Bhadeshia HKDH. Dry rolling/sliding wear of nanostructured bainite. *Wear* 2014;316:70–8.
- [355] Seabra J, Berthe D. Influence of surface waviness and roughness on the normal pressure distribution in the hertzian contact. *J Tribol* 1987;3:462–9.
- [356] Way S. Pitting due to rolling contact. *ASME J Appl Mech* 1935;2:A49–58.

- [357] Dawson PH. Rolling contact fatigue crack initiation in a 0.3 per cent carbon steel. *Proc Inst Mech Eng* 1968;183:75–86.
- [358] Clayton JQ, Knott JF. Phosphorus segregation in austenite in Ni-Cr and Ni-Cr-Mn steels. *Metal. Science* 1982;16:145–52.
- [359] Railtrack-plc, Rolling contact fatigue in rails: a guide to current understanding and practice, Birmingham, UK; 2001.
- [360] Dirks B, Enblom R, Ekberg A, Berg M. The development of a crack propagation model for railway wheels and rails. *Fatigue & Fract Eng Mater Struct* 2015;38:1478–91.
- [361] Garnham JE, Davis CL. The role of deformed rail microstructure on rolling contact fatigue initiation. *Wear* 2008;265:1363–72.
- [362] K.J. Miller, The three thresholds for fatigue crack propagation, Vol. 27, ASTM special technical publication, eds R.S. Piascik and J.C. Newman and N.E. Dowling, 1997, Ch. Fatigue and Fracture Mechanics, pp. 267–286.
- [363] Vásquez-Chacón IA, Gallardo-Hernández EA, Moreno-Ríos M, Vite-Torres M. Influence of surface roughness and contact temperature on the performance of a railway lubricant grease. *Mater Lett* 2021;285:129040.
- [364] Bachchhav B, Bagchi H. Effect of surface roughness on friction and lubrication regimes, *Materials Today: Proceedings* 2021;38: 169–173.
- [365] Tallian TE, Chiu YP, Amerongen EV. Prediction of traction and microgeometry effects on rolling contact fatigue life. *ASME J Lubricat Technol* 1978;100:156–65.
- [366] G.R. Miller, L.M. Keer, H.S. Cheng, On the mechanics of fatigue crack growth due to contact loading, *Proc Roy Soc London A: Mathematical, Physical and Engineering Sciences* 1985;397: 197–209.
- [367] Mackay TL, Alperin BJ, Bhatt DD. Near-threshold fatigue crack propagation of several high strength steels. *Eng Fract Mech* 1983;18:403–16.
- [368] Ritchie RO. Influence of microstructure on near-threshold fatigue crack propagation in ultra high strength steel. *Metal. Science* 1977;11:368–81.
- [369] Kaneta M, Yatsuzuka H, Murakami Y. Mechanism of crack growth in lubricated rolling/sliding contact. *Trans Am Soc Lubricat Eng* 1985;28:407–14.
- [370] Fletcher DI, Franklin FJ, Kapoor A. Image analysis to reveal crack development using a computer simulation of wear and rolling contact fatigue. *Fatigue & Fract Eng Mater Struct* 2003;26:957–67.
- [371] Frederick CO, Armstrong PJ. A mathematical representation of the multiaxial bauschinger effect. *Mater High Temp* 2007;24:1–26.
- [372] Chaboche JL. Constitutive equations for cyclic plasticity and cyclic viscoplasticity. *Int J Plast* 1989;5:247–302.
- [373] Jiang Y, Kurath P. Characteristics of the armstrong-frederick type plasticity models. *Int J Plast* 1996;12:387–415.
- [374] Jiang Y, Sehitoglu H. Modeling of cyclic ratchetting plasticity, part i: development of constitutive relations. *J Appl Mech* 1996;63:720–5.
- [375] Ekh M, Johansson A, Thorberntsson H, Josefson BL. Models for cyclic ratchetting plasticity – integration and calibration. *J Eng Mater Technologyengineering Mater Technol* 2000;122:49–55.
- [376] Franklin FJ, Widiyarta I, Kapoor A. Computer simulation of wear and rolling contact fatigue. *Wear* 2001;251:949–55.
- [377] Sosnovskiy LA. *Tribo-fatigue: wear-fatigue damage and its prediction*. Springer Science and Business Media; 2010.
- [378] Kalousek J, Magel E. Achieving a balance: the magic wear rate. *Railway Track & Struct* 1997;93:50–2.
- [379] G. Donzella, F. M, A. Mazzù, C. Petrogalli, R. Roberti, Progressive damage assessment in the near-surface layer of railway wheel–rail couple under cyclic contact, *Wear* 271 (2011) 408–416.
- [380] Tyfow WR, Beynon JH, Kapoor A. The steady state wear behaviour of pearlitic rail steel under dry rolling-sliding contact conditions. *Wear* 1995;180:79–89.
- [381] Olofsson U, Nilsson R. Surface cracks and wear of rail: A full-scale test on a commuter train track. *Proc Inst Mech Eng, Part F: J Rail Rapid Transit* 2002;216:249–64.
- [382] RSSB, Management and understanding of rolling contact fatigue: Mechanisms of crack growth (t355 report), Tech. rep., Rail Safety and Standards Board, London, U.K; 2007.
- [383] Garwood MF, Zurburg HH, Erickson MA. Correlation of Laboratory Tests and Service Performance: Interpretation of tests and correlation with service, *ASM. Ch.* 1951;1:1–77.
- [384] Nishiyama S. Statistical analysis of fatigue test data. *J Soc Mater Sci, Japan* 1980;29:24–9.
- [385] Peet MJ, Hill P, Rawson M, Wood S, Bhadeshia HKDH. Fatigue of extremely fine bainite. *Mater Sci Technol* 2011;27:119–23.
- [386] G. Chalant, B.M. Suyitno, Effects of microstructure on low and high cycle fatigue behaviour of a micro-alloyed steel, in: M. Jono, T. Inoue (Eds.), *Proceedings of the 6th International Conference on Mechanical Behaviour of Materials*, Vol. VI, Pergamon Press, Oxford, Elsevier Science, Kyoto, Japan, 1991, pp. 511–516.
- [387] G. Girsch, N. Frank, P. Pointner, New rail grades - a technical performance overview. In: *8th International Heavy Haul Conference*, Vol. Safety, Environment and Productivity, International Heavy Haul Association, Rio de Janeiro, Brazil; 2005. p. 731–8.
- [388] Clayton P, Brave G. Fatigue origination and growth experiment, FRA/ORD 91/18, US Department of Transportation; 1991.
- [389] Ranjha SA. Effect of head wear on rail underhead radius stresses and fracture under high axle load conditions. Ph.D. thesis. Melbourne, Australia: Swinburne University of Technology; 2013.
- [390] Garber AK, Arsenkin AM, Grigorovich KV, Shibaev SS, Kushnarev AV, Petrenko YP. Analysis of various versions of the deoxidation of rail steel at OAO NTMK. *Elektrometallurgiya* 2008;10:2–9.
- [391] Grigorovich KV, Trushnikova AS, Arsenkin AM, Shibaev SS, Garber AK. Structure and metallurgical quality of rail steels produced by various manufacturers. *Metally* 2006;5:72–87.
- [392] Bhadeshia HKDH. Neural networks in materials science. *ISIJ Int* 1999;39:966–79.
- [393] Smith KN, Watson P, Topper TH. Stress-strain function for the fatigue of metals. *J Mater* 1970;5:767–78.
- [394] Pun CL, Kan Q, Mutton PJ, Kang G, Yan W. A single parameter to evaluate stress state in rail head for rolling contact fatigue analysis. *Fatigue & Fract Eng Mater Struct* 2014;37:909–19.
- [395] Qiu X. Rolling contact fatigue behavior of three eutectoid rail steels. Ph.D. thesis. Oregon, USA: Oregon Health and Science University; 1987.
- [396] Dikshit V. Rolling contact fatigue behavior of pearlitic rail steels. Ph.D. thesis. Oregon, USA: Oregon Health and Science University; 1992.
- [397] Fletcher DI, Hyde P, Kapoor A. Modelling and full-scale trials to investigate fluid pressurisation of rolling contact fatigue cracks. *Wear* 2008;265:1317–24.
- [398] Bower AF. The influence of crack face friction and trapped fluid on surface initiated rolling contact fatigue cracks. *J Tribol* 1988;110:704–11.
- [399] Bogdański S, Lewicki P. 3D model of liquid entrapment mechanism for rolling contact fatigue cracks in rails. *Wear* 2008;265:1356–62.
- [400] Bogdański S. Liquid–solid interaction at opening in rolling contact fatigue cracks. *Wear* 2005;258:1273–9.
- [401] Hanson MT, Keer LM. An analytical life prediction model for the crack propagation occurring in contact fatigue failure. *Tribol Trans* 1992;35:451–61.
- [402] Bogdański S. A rolling contact fatigue crack driven by squeeze fluid film. *Fatigue & Fract Eng Mater Struct* 2002;25:1061–71.
- [403] Karlsson B, Linden G. Plastic deformation of ferrite–pearlite structures in steel. *Mater Sci Eng* 1975;17:209–19.
- [404] Ivanisenko Y, Lojkowski W, Valiev RZ, Fecht HJ. The mechanism of formation of nanostructure and dissolution of cementite in a pearlitic steel during high pressure torsion. *Acta Mater* 2003;51:5555–70.
- [405] Sauvage X, Copreaux J, Danoix F, Blavette D. Atomic-scale observation and modelling of cementite dissolution in heavily deformed pearlitic steels. *Philos Mag A* 2000;80:781–96.
- [406] Liu CD, Bassim MN, Lawrence SS. Management and understanding of rolling contact fatigue. *Eng Fract Mech* 1995;50:301–7.
- [407] Li X, Ma X, Subramanian SV. EBSD characterization of secondary microcracks in the heat affected zone of a X100 pipeline steel weld joint. *Int J Fract?* 2015. <https://doi.org/10.1007/s10704-015-0024-3>.
- [408] Green MR, Rainforth WM, Frolish MF, Beynon JH. The effect of microstructure and composition on the rolling contact fatigue behaviour of cast bainitic steels. *Wear* 2007;263:756–65.
- [409] Caballero FG, Bhadeshia HKDH. Very strong bainite. *Curr Opin Solid State Mater Sci* 2004;8:251–7.
- [410] Zaretsky EV. Rolling bearing steels – a technical and historical perspective. *Mater Sci Technol* 2012;28:58–69.
- [411] Liu H, Sun J, Jiang T, Guo S, Liu Y. Improved rolling contact fatigue life for an ultrahigh carbon steel with nanobainitic microstructure. *Scripta Mater* 2014;90:17–20.
- [412] Bevan A, Molyneux-Berry P, Eickhoff B, Burstow M. Development and validation of a wheel wear and rolling contact fatigue damage model. *Wear* 2013;307:100–11.

- [413] Guzowski S, Michnej M, Zajac G. Tribological wear of wheel rims in rail vehicles in operating conditions. *Tribologia* 2016;268:91–9.
- [414] Ekberg A. Rolling contact fatigue of railway wheels—a parametric study. *Wear* 1997;211:280–8.
- [415] Cordiano HV. Effect of residual stress on the low cycle fatigue life of large scale weldments in high strength steel. *J Eng Industry, A.S.M.E.* 1970;92:86–92.
- [416] Guo YB, Warren AW, Hashimoto F. The basic relationships between residual stress, white layer, and fatigue life of hard turned and ground surfaces in rolling contact. *CIRP J Manuf Sci Technol* 2010;2:129–34.
- [417] Segade V. Reliability growth of cementite steel, *Mashinostroenie* 216.
- [418] Pan A, Dobuzhskaya A, Shur E, Galitsin G. Structure and properties of rail steel, microalloyed vanadium and titanium. *Steel (Stal’)* 2001;10:55–7.
- [419] Vorozhishchev V, Devyatkin Y, Shur E, Kozirev N, Gulyaeva T. Quality of rails of dispersion-hardened steel. *Steel (Stal’)* 2003;8:64–70.
- [420] P. Gembalova, J. Boruta, E. Grycz, K.M. Cmiel, Hot forming parameters research of bearing steel, *Archives of Civil and Mechanical Engineering* 721–28.
- [421] Chattopadhyay S, Sellars CM. Kinetics of pearlite spheroidisation during static annealing and during hot deformation. *Acta Metall* 1982;30:157–70.
- [422] Anonymous, The effect of carbide network on the life of AISI 52100 in rolling contact fatigue, Tech. Rep. May 6, Federal-Mogul Corporation, Derbyshire, U.K; 1982.
- [423] Garnham JE, Davis CL. Very early stage rolling contact fatigue crack growth in pearlitic rail steels. *Wear* 2011;271:100–12.
- [424] J.E. Garnham, D.I. Fletcher, C.L. Davis, F.J. Franklin, Visualization and modelling to understand rail rolling contact fatigue cracks in three dimensions, in: *Proceedings of the Institution of Mechanical Engineers, Part F: Journal of Rail and Rapid Transit*, Vol. 225, 2011, pp. 165–178.
- [425] Lewandowski JJ, Thompson AW. Microstructural effects on the cleavage fracture stress of fully pearlitic eutectoid steel. *Metall Mater Trans A* 1986;17:1769–86.
- [426] Park YJ, Bernstein IM. The process of crack initiation and effective grain size for cleavage fracture in pearlitic eutectoid steel. *Metall Trans A* 1979;10:1653–64.
- [427] Marder AR, Bramfitt BL. The effect of morphology on the strength of pearlite. *Metall Trans A* 1976;7:365–72.
- [428] Gray GT, Thompson AW, Williams JC, Stone DH. The effect of microstructure on fatigue crack propagation in pearlitic eutectoid steels. *Can Metall Q* 1982;21: 73–8.
- [429] Suh DW, Bae JH, Cho JY, Oh KH, Lee HC. Fem modeling of flow curves for ferrite/pearlite two-phase steels. *ISIJ Int* 2001;41:782–7.
- [430] Eden HC, Garnham JE, Davis CL. Influential microstructural changes on rolling contact fatigue crack initiation in pearlitic rail steels. *Mater. Sci. Technol.* 2005; 21:623–9.
- [431] Gray III GT, Thompson AW, Williams JC. Influence of microstructure on fatigue crack initiation in fully pearlitic steels. *Metall. Trans. A* 1985;16:753–60.
- [432] Garnham JE, Beynon JH. The early detection of rolling-sliding contact fatigue cracks. *Wear* 1991;144:103–16.
- [433] Kabo E. Material defects in rolling contact fatigue – influence of overloads and defect clusters. *Int. J. Fatigue* 2002;24:887–94.
- [434] Li YD, Liu CB, Xu N, Wu XF, Guo WM, Shi JB. A failure study of the railway rail serviced for heavy cargo trains. *Case Stud Eng Fail Anal* 2013;1:243–8.
- [435] Hai DT. Current status of existing railway bridges in vietnam: An overview of steel deficiencies. *J Constr Steel Res* 2006;62:987–94.
- [436] Sol-Sánchez M, Moreno-Navarro F, Rubio-Gámez MC. The use of elastic elements in railway tracks: A state of the art review. *Constr Build Mater* 2015;75: 293–305.
- [437] I. Gallego, J.M. noz, A. Rivas, S. Sánchez-Cambronero, Vertical track stiffness as a new parameter involved in designing high-speed railway infrastructure, *Journal of transportation engineering* 137 (2011) 971–979.
- [438] G.J. Fowler, A.S. Tetelman, Stress concentration effect on nonmetallic inclusions and its effect on fatigue crack initiation in rail steel, in: *Proceedings of the 77th Annual Technical Conference*, Vol. 79, AREA, 1978, pp. 1–447.
- [439] Ransom JT. The effect of inclusions on the fatigue strength of sae-4340 steels. *Trans ASM* 1954;46:1254–69.
- [440] Nishijima S, Tanaka K, Sumiyoshi H. The defect size determining the fatigue limits of steels. In: *Proc 6th Int Conf Fracture (ICF6)*, Vol. 3; 1984, p. 1719–26.
- [441] Liu CD, Bassim MN, Lawrence SS. Evaluation of fatigue-crack initiation at inclusions in fully pearlitic steels. *Mater Sci Eng, A* 1993;167:107–13.
- [442] Safonova KE, Velikanov AV, Vinokurov IY, Rabinovich DM, Ravzin YR. The composition of steel for high strength rails. *Vestnik VNIITZ* 1974;1:45–9.
- [443] Zheng SB, Stobbs WM. A transmission electron microscope study of the white etching layer on a rail head. *Mater Sci Eng A* 1984;66:195–204.
- [444] Hwang HW, Ohsaki S, Mitao S, Ohnuma M, Hono K. Microstructural investigation of white etching layer on pearlite steel rail. *Mater Sci Eng A* 2006;421:191–9.
- [445] Wu J, Petrov RH, Kölling S, Koenraad P, Malet L, Godet S, Sietsma J. Micro and nanoscale characterization of complex multilayer – structured white etching layer in rails. *Metals* 2018;8:100749.
- [446] Bernsteiner C, Müller G, Meierhofer A, Six K, Künstner D, Dietmaier P. Development of white etching layers on rails: simulations and experiments. *Wear* 2016; 366–367:116–22.
- [447] Bedoya-Zapata AD, León-Henao H, Mesaritis M, Molina LF, Palacio M, Santa JF, Ruda JS, Toro A, Lewis R. White etching layer (WEL) formation in different rail grades after grinding operations in the field. *Wear* 2022;502:204371.
- [448] Xu W, Zhang W. An investigation of the crystallography of pearlites nucleated on the proeutectoid cementite. *Acta Metall Sin* 2018;55:496–510.
- [449] Solano-Alvarez W, Bhadeshia HKDH. White-etching matter in bearing steel: Part II: distinguishing cause and effect in bearing steel failure. *Metall Mater Trans A* 2014;45:4916–31.
- [450] Solano-Alvarez W, Pickering EJ, Bhadeshia HKDH. Degradation of nanostructured bainitic steel under rolling contact fatigue. *Mater Sci Eng A* 2014;617: 156–64.
- [451] Bhadeshia HKDH. Anomalies in carbon concentration determinations from nanostructured bainite. *Mater Sci Technol* 2015;31:758–63.
- [452] Cookson JM, Mutton PJ. The role of the environment in the rolling contact fatigue cracking of rails. *Wear* 2011;271:113–9.
- [453] Sugino K, Kageyama H, Sato M. Effect of wheel and rail profiles on wear and fatigue behavior of rail. In: *Contact Mechanics and Wear of Rail/Wheel Systems*. University of Waterloo Press; 1986. p. 435–50.
- [454] Grunberg L, Jamieson DT, Scott D. Hydrogen penetration in water-accelerated fatigue of rolling surfaces. *Phil Mag* 1963;8:1553–68.
- [455] Tamada K, Tanaka H. Occurrence of brittle flaking on bearings used for automotive electrical instruments and auxiliary devices. *Wear* 1996;199:245–52.
- [456] Schatzberg P, Felsen IM. Effect of water and oxygen during rolling contact lubrication. *Wear* 1968;12:331–42.
- [457] Imran T, Jacobson B, Shariff A. Quantifying diffused hydrogen in AISI-52100 bearing steel and in silver steel under tribo-mechanical action: Pure rotating bending, sliding-rotating bending, rolling-rotating bending and uni-axial tensile loading. *Wear* 2006;261:86–95.
- [458] Irving R, Scarlett NA. Wear problems associated with lubrication in inert atmospheres. *Wear* 1964;7:244–54.
- [459] Deulin EA, Nevshupa RA. Deuterium penetration into the bulk of a steel ball of a ball bearing due to its rotation in vacuum. *Appl Surf Sci* 1999;144–145:283–6.
- [460] Ciruna JA, Szieleit HJ. The effect of hydrogen on the rolling contact fatigue life of AISI 52100 and 440C steel balls. *Wear* 1973;24:107–18.
- [461] Song J, Shi L, Ding H, Galas R, Omasta M, Wang W, Guo J, Liu Q, Hartl M. Effects of solid friction modifier on friction and rolling contact fatigue damage of wheel-rail surfaces. *Friction* 2022;10:597–607.
- [462] MacKay DJC. *Information theory, inference, and learning algorithms*. Cambridge University Press; 2003.
- [463] Solano-Alvarez W, Peet M, Pickering E, Jaiswal J, Bevan A, Bhadeshia H. Synchrotron and neural network analysis of the influence of composition and heat treatment on the rolling contact fatigue of hypereutectoid pearlitic steels. *Mater Sci Eng: A* 2017;707:259–69.
- [464] Shebani A, Iwnicki S. Prediction of wheel and rail wear under different contact conditions using artificial neural networks. *Wear* 2018;406:173–84.
- [465] Khalid FA, Edmonds DV. Interphase precipitation in microalloyed engineering steels and model alloy. *Mater Sci Technol* 1993;9:384–96.
- [466] Khalid FA, Edmonds DV. Effect of vanadium on the grain boundary carbide nucleation of pearlite in high-carbon steels. *Scr Metall Mater* 1994;30:1251–5.
- [467] Chairuangrsri T, Edmonds DV. The precipitation of copper in abnormal ferrite and pearlite in hyper-eutectoid steels. *Acta Mater* 2000;48:3931–49.